## Czech Technical University and Université Clermont Auvergne

Physical Engineering

Specialty “Materials”

Ph. D. Thesis

# Infrared calorimetry applied to thermomechanical characterization of NiTi alloys

Presented by

## Mr. Antoine JURY

Thesis submitted in partial fulfillment of requirements for Degree of “Doctor of Philosophy in Material Engineering”

Defended in public on June 24th, 2021 before the jury composed of:

| | | |
|---|---|---|
| Mr. Yongjun He | Associate Professor HDR, ENSTA Paris | Rapporteur |
| Mr. Hanuš Seiner | Doc. Ing., Institute of Thermomechanics of the CAS | Rapporteur |
| Mrs. Karine Lavernhe-Taillard | Associate Professor HDR, ENS Paris-Saclay | Examiner |
| Mr. Šittner Petr | Doc. Ing., Institute of the Physics of the CAS | Examiner |
| Mr. Moumni Ziad | Professor, ENSTA Paris | Examiner |
| Mr. Heller Luděk | Doc. Ing., Institute of the Physics of the CAS | Co-supervisor |
| Mr. Karlík Miroslav | Professor, Czech Technical University in Prague | Supervisor |
| Mr. Xavier Balandraud | Professor, Sigma Clermont engineering school | Supervisor |

**Institute of Physics of the CAS and Institut Pascal – M3G department**

## Abstract:

Shape memory alloys (SMAs) exhibit spectacular functional properties, such as superelasticity, single- and two-way shape memory effects, and passive damping properties. In the first part of this thesis, we present a state of the art on nickel-titanium (NiTi) SMAs and on deformation calorimetry. We focus on the use of infrared thermography (IR) and the heat source reconstruction technique. In a second part of the thesis, we present different experimental studies on NiTi SMA wires. First, we performed a calorimetric analysis of a superelastic cycle of a mechanically stabilized wire. Particular attention was paid to the calorific quantities of the nucleation and annihilation events of the austenite and martensite phases. We were able to follow the space-time kinetics of the forward (A→M) and reverse (M-→A) transformations during the cycle, as a result of the strong thermo-mechanical coupling that NiTi presents. We concluded that the mechanical dissipations during austenite merging are higher than during nucleation. Next, we analyzed twenty superelastic cycles of a virgin NiTi wire. Moreover, we observed in particular that the number of nucleation and merging sites increases progressively during the cycles until reaching a maximum number. Finally, we observed a strong decrease of the calorific response of the tested material of about 22% which could be attributed to the stabilization of the material and a retention of the martensite fraction.

**Keywords**: shape memory alloys, NiTi, heat source reconstruction, thermal diffusivity, thermomechanical behavior, tensile test, NiTi training analysis.

# Résumé :

Les alliages à mémoire de forme (AMF) présentent des propriétés fonctionnelles spectaculaires, telles que la superélasticité, des effets de mémoire de forme simple-sens et double-sens, ainsi que des propriétés d'amortissement passif. Dans la première partie de cette thèse, nous présentons un état de l'art sur les AMF nickel-titane (NiTi) et sur la calorimétrie de déformation. Nous nous focalisons en particulier sur l’utilisation de la thermographie infrarouge (IR) et la technique de reconstruction de sources de chaleur. Dans une seconde partie de la thèse, nous présentons différentes études expérimentales sur des fils AMF en NiTi. Tout d’abord, nous avons procédé à l'analyse calorimétrique d'un cycle superélastique d'un fil préalablement entraîné mécaniquement. Une attention particulière a été portée aux quantités calorifiques des événements de nucléation et d'annihilation des phases austénite et martensite. Nous avons pu suivre la cinétique spatio-temporelle des transformations directe (A→M) et inverse (M→A) au cours du cycle, résultat du fort couplage thermo-mécaniques que présente le NiTi. Nous avons conclu que les dissipations mécaniques pendant la fusion de l'austénite sont plus élevées que lors de la nucléation. Ensuite, nous avons analysé vingt cycles superélastiques d'un fil NiTi vierge. De plus, nous avons observé en particulier que le nombre de sites de nucléation et de fusion augmente progressivement au cours des cycles jusqu'à atteindre un nombre maximal. Enfin, nous avons observé une forte diminution de la réponse calorifique du matériau testé d'environ 22% qui pourrait être attribuée à la stabilisation du matériau et à une rétention de la fraction de martensite.

**Mots clés :** alliages à mémoire de forme, NiTi, reconstruction des sources de chaleur, diffusivité thermique, comportement thermomécanique, essai de traction, analyse de la formation du NiTi.

## Acknowledgments :

This thesis document represents the completion of 3 years of thesis in the laboratories of functional materials in Prague, innovative materials and experimental mechanics in Clermont-Ferrand. I would like to thank all the members of these different laboratories that I had the opportunity to meet or exchange with, who have greatly helped in this important part of my professional life.

I would like to thank Ziad Moumni for accepting to chair my thesis jury.

I would like to thank my two manuscript referees Prof. Yongjun He and Prof. Hanuš Seiner who accepted the difficult task of proofreading my report, and I thank them for the constructive feedback during my defense and in their respective reports.

I would like to thank Karine Lavernhe-Taillard for agreeing to be a member of the jury, as well as for her remarks during my thesis defense.

I would like to thank Petr Šittner for accepting me in the condensed matter department at the Institute of Physics in Prague. I also thank him for accepting to be a member of my thesis jury and for the very interesting discussions during our meetings and during the writing of my paper.

I would like to thank Miroslav Karlík for accepting the co-direction of my thesis. I would also like to thank him for managing all the administrative details related to the Technical University of Prague, as well as for our discussions during our interviews.

I would like to thank Xavier Balandraud for accepting the co-direction of my thesis. I would also like to thank him for his welcome in Clermont-Ferrand and for his introduction to the heat sources reconstruction technique and the great discussions that it generated, especially in the last line.

I would like to thank Luděk Heller for having accepted the supervision and the proposal of this thesis subject. I would also like to thank him for his welcome in Prague and for his introduction to the world of shape memory alloys as well as for the long discussion concerning the understanding of the mechanisms involved in the martensitic transformation.

For a thesis is nothing without other thesis students. I would like to thank all the PhD students of the M3G laboratory that I could meet in Clermont-Ferrand, especially Corentin, Rym and Dimitri. I would like to thank all the members of the functional materials laboratory in Prague, Ondra, Silvia, Ivo, Mira, Yuchen, Pejman, Sneha, Lukáš, David and Eduardo.

I also want to thank my family. Among them I think particularly of my parents who supported me throughout these three years. Katka for her presence and confidence of every moment.

# Table of contents

# Table of figures

# Acronyms

| | |
|---|---|
| AME | austenitic merging event |
| ANE | austenitic nucleation event |
| COP | coefficient of performance |
| DIC | digital image correlation |
| DSC | differential scanning calorimetry |
| ECE | elastocaloric effect |
| FMBF | forward martensite band front |
| FMT | forward martensitic transformation |
| FMTQ | forward martensitic transformation heat |
| FMTW | forward martensitic transformation work |
| HDC | high damping capacity |
| HSR | heat source reconstruction |
| IRT | infrared thermography |
| MBF | martensite band front |
| MNE | martensitic nucleation event |
| MME | martensitic merging event |
| MT | martensite transformation |
| RMBF | reverse martensite band front |
| RMT | reverse martensitic transformation |
| RMTQ | reverse martensitic transformation heat |
| RMTW | reverse martensitic transformation work |
| SE | superelasticity |
| SIMT | stress-induced phase transformation |
| SMA | shape memory alloy |
| SME | shape memory effect |
| TWSME | two-way shape memory effect |
| TIMT | thermally-induced phase transformation |
| WHS | weak heat source |

# General introduction

Shape memory alloys (SMAs) are smart materials that exhibit several attractive thermomechanical properties such as shape memory effects, superelasticity and high damping capacity. In the past few decades, SMAs have attracted a lot of interest for scientific research and engineering applications. In particular, nickel-titanium-based (NiTi-based) SMAs are used as biomechanical components thanks to their biocompatibility. They have also found numerous developments in mechatronics and mechanical engineering, for instance, to develop a new generation of actuators. Applications concern several important industrial fields such as automotive, aerospace, robotics, etc.

Macroscopic properties of SMAs are inherited from the first-order displacive solid-solid phase transformations triggered by stress and temperature. Generally, the so-called austenite (A) and martensite (M) phases are present at “high” and “low” temperatures, respectively. Large reversible strains can be created during the phase change. Phase transitions can be simply obtained using the Joule effect thanks to the metallic nature of the SMAs, which is an advantage for the integration in smart structures. A↔M transformation can be also induced at “high” temperature by mechanical loading. The martensitic transformation is intrinsically accompanied by release/absorption of latent heat that significantly changes the material’s temperature, making the thermomechanical responses rate dependent. Among other difficulties in applying SMAs in engineering applications, let us note also their non-linear and hysteretic responses, as well as the potential presence of an intermediate phase between austenite and martensite (namely the R-phase). Also, the behavior of an SMA is highly dependent on its chemical composition, its manufacturing process, heat treatment and preparation (thermomechanical history).

The use of these materials in engineering applications remains generally limited by low structural fatigue performance and cyclic instability of responses termed functional fatigue. In materials science, the study of fatigue refers to the change of properties induced by applying cyclic loading (thermal and/or mechanical). The *functional fatigue* in NiTi refers to the large change of properties specific to SMAs (shape memory effects, superelasticity, high damping capacity) along with the first cycles. S*tructural fatigue* refers to the accumulation of microstructural changes leading to the rupture of the material, as in the fatigue of conventional materials.

Any deformation process (by elasticity, plasticity, viscosity, fatigue, rupture, cracking, phase transformation…) is accompanied by production or absorption of heat by the material itself. Throughout this document, we will use the term “**heat source**” or “**internal heat source**” to designate the corresponding heat power density (in W.m$^{-3}$). These terms will be used both for heat release (positive heat source) and heat absorption (negative heat “source”). Throughout the document, the reader should pay attention to the difference between “heat source” and “**heat**”, the latter being the time integral of the former. In practice, “specific heat” values (in J.g$^{-1}$) will be provided, similarly to what is done in the field of thermodynamics.

Two types of heat sources exist in materials: heat sources due to thermomechanical couplings (associated with mechanically reversible phenomena) and the mechanical dissipation (associated with mechanically irreversible phenomena). Both quantities are involved in the heat diffusion equation. Two types of thermomechanical couplings exist in SMAs: thermo-elastic coupling heat sources (associated with thermo-elasticity) and latent heat sources (associated with phase change). Fatigue is by definition accompanied by a release of mechanical dissipation. In this context, measuring temperature during a mechanical test appears to be relevant to study martensitic transformations as well as fatigue processes.

The technique to carry out heat measurement is calorimetry. Heat is calculated from temperature data and specimen's mass. A well-known system is the differential scanning calorimetry (DSC) using a thermocouple. However, commercial DSC systems do not enable to apply mechanical loading to the material specimen tested. Efforts have been made by several academic research teams around the world to implement systems of *deformation calorimetry*. At first, thermocouples were placed onto the specimen surface to directly measure the temperature variations during loading. Later chambers were developed embedding thermocouples within their walls enabling to place the chamber around the mechanical testing machine (the so-called "micro-calorimeters"). However, one of the problems with using punctual temperature measurements (i.e. thermocouples) in classical calorimetry and deformation calorimetry is the assumption that the heat sources are homogeneous within the specimen to calculate the corresponding heat. While this assumption seems to be fairly valid for the characterization of small volume specimens (as done for DSC with the order of a few $mm^3$), application to large specimens is more complex. In mechanical testing, the dimensions of the specimens are generally larger (up to several tens of centimeters). Besides, deformation processes often occur heterogeneously. The development of infrared thermography (IRT) systems makes it possible to obtain temperature fields at the surface of large material specimens. IRT is now widely used in the laboratory to provide additional information to the mechanical data (force, displacement, stress, strain).

In NiTi SMAs, the transformation stresses increase linearly with the temperature of the material. During the application of a mechanical loading at constant ambient temperature, the temperature heterogeneity within the specimen (in part due to heat exchanges with its environment) appears due to martensitic transformation triggered at a critical stress. The martensitic transformation is usually triggered at one or several nucleation sites from which the martensite transformation bands propagate via moving interfaces at which the latent heat is being released. Similarly, upon unloading, austenite bands appear and propagate via interfaces where the latent heat is being absorbed. IRT is particularly suitable to observe and thermodynamically quantify these deformation phenomena.

IRT provides a wealth of information to the mechanical experimenter. However, the evolution of the temperature depends on heat exchanges: by conduction within the specimen, by contact with the jaws of the testing machine, by convection with the air, and by radiation. Based on certain assumptions, a technique called "heat source reconstruction" (HSR) can be used to trace the distribution of heat sources from the knowledge of temperature fields measured on the surface of the specimen by IRT. The technique relies on the heat diffusion equation. HSR was developed in the 80s, but it has not had the same success as strain full-field measurement methods such as digital image correlation (DIC) or the grid method.

Several approaches have been developed for HSR. In this context, **the objective of the present study is to use IRT and HSR for calorific analysis of martensitic transformation in NiTi SMA wires using a one-dimensional (1D) version of the heat diffusion equation**. Surprisingly, such a 1D approach has never been used to investigate the response of NiTi, to my knowledge. So the application of this 1D approach was promising at the beginning of my Ph.D work! Obviously, application of HSR is not easy as many metrological aspects must be considered before presenting quantitative data. The thesis is organized into three chapters, which may not seem like much, but each one has been a great (and long and difficult) adventure:

- Chapter 1 is a review of the literature on different points related to the topic of the present research work: fundamental points on NiTi SMAs, a state of the art on deformation calorimetry methods, mathematical framework of the thermomechanics of materials, and details about HSR techniques;
- Chapter 2 is a calorimetric study of the localized and homogeneous deformation processes in mechanically stabilized NiTi wire during a superelastic cycle;

- Chapter 3 is a calorimetric study of the functional fatigue of NiTi wire, i.e. the first mechanical cycles starting from a virgin specimen.

This research work was performed in the framework of a co-tutorship agreement between the Czech technical university in Prague (CTU-Prague) in the Czech Republic and the Université Clermont Auvergne (UCA) in France. I performed my research activity both at the Institute of Physics (FZU) of the Czech Academy of Sciences (CAS) and at the Institute Pascal (IP). Thermomechanical couplings in a cyclically loaded NiTi are complex, but it was also difficult for me to switch cyclically between mechanical engineering (my background) and physics (which has always impressed me!)!

# Chapter 1. Bibliographical review

This chapter is a review of the literature on different points related to the topic of the present research work, namely the **thermomechanical analysis of nickel-titanium (NiTi) shape memory alloy (SMA) wires using infrared (IR) thermographic measurement**.

The chapter includes first a rapid presentation of the functional properties of NiTi SMAs. It recalls also some information about the underlying physical phenomenon at the origin of the macroscopic properties: a martensitic transformation (MT) triggered by temperature and stress. In the context of the present work, a focus is then put on the calorific aspects accompanying MT in SMAs subjected to mechanical loading, and more specifically during loading-unloading mechanical cycles in tension. The basic notions concerning calorimetric measurements are recalled. Beyond classical differential scanning calorimetry (DSC), the procedure using IR thermography is presented. A focus is put on the **deformation calorimetry (DC)** methods, i.e. the measurement of the heat produced or absorbed by the material itself.

In the last part of this review, the principles of the **heat source reconstruction technique (HSR)** applied to the mechanics of materials are presented. This physics-based image processing consists of evaluating the density of heat power produced or absorbed by the material from the knowledge of the temperature fields measured by an IR camera at the surface of the specimen under mechanical loading. Throughout this chapter, some application cases that have been identified in the literature are presented.

The chapter is organized as follows:

- Section 1 recalls some fundamental points on NiTi SMAs: macroscopic functional properties, microstructural aspects, phase diagram, as well as some typical observations obtained using full-field measurement techniques.
- Section 2 presents a state of the art on DC methods, in particular using IR thermography.
- Section 3 presents the mathematical framework of the thermomechanics of materials. The section focuses on the writing of the general form (i.e. in three dimensions) of the heat diffusion equation, showing the two types of heat sources in materials subjected to mechanical loading: *mechanical dissipation* (also named *intrinsic dissipation*, associated with irreversible mechanical phenomena) and *thermomechanical couplings* (thermo-elastic coupling in all materials, and latent heat production/absorption for MT in SMAs).
- Finally, Section 4 gives some details about HSR techniques. The two versions of the heat diffusion equation that will be used in the next chapter are developed. The one-dimensional (1D) version of the equation will be presented. It concerns the case of elongated specimens subjected to uniaxial loading (typically a wire) with the heterogeneous heat source distribution. A so-called 0D version of the heat equation is also presented. Under certain hypotheses, it is applicable in the case of homogeneous heat source distribution (even if the temperature distributions are not homogeneous).

It is important to note that all of these topics are broad and it is not possible to provide all the details. This chapter is an attempt to survey a significant amount of reading done during the course of this Ph.D work. Finally, note that acronyms are recalled in each chapter to make each part of the manuscript independent.

## 1.1. Fundamentals of NiTi SMAs

SMAs exhibit several attractive properties such as the one-way memory effect (OWSME, or simply SME) and the two-way shape memory effect (TWSME), the recovery of large strains during cyclic loadings (superelasticity – SE), high damping capacities (HDC), as well as the elastocaloric effect (ECE). These properties stem from a displacive phase transition that can be induced in two ways: it can be either thermally-induced (giving rise to SME), or mechanically-induced (giving rise to SE). The corresponding MTs are often referred to as the thermally-induced martensitic transformation (TIMT) and the stress-induced martensitic transformation (SIMT) respectively. Though MT in SMAs is termed "reversible", the reversibility is not perfect. Irreversible processes accompanying MT give rise to hysteretic responses (from which HDC is derived), leading to complex thermomechanical responses. Many handbooks can be found about all these properties: see for instance Refs [1–6] (including modeling aspects in Refs [1,3,5]). The present section browses some of the important aspects as follows:

- Section 1.1.1 recalls the physical origin of functional properties;
- Section 1.1.2 presents the phase diagram of NiTi SMAs in the stress-temperature plane for uniaxial tensile loadings;
- Sections 1.1.3 to 1.1.7 provide details about SE, SME, HDC, as well as the "heat effects" on the SE response;
- Section 1.1.8 provides information about microstructural effects;
- Finally, Section 1.1.9 presents experimental results on heterogeneity in the strain and temperature fields measured by full-field techniques.

### 1.1.1 The physical origin of functional properties

The functional properties of NiTi stem from crystallographic features. Indeed, MT is the change between high-symmetry B2 cubic phase (termed *austenite* – A) and low-symmetry B19' monoclinic phase (termed *martensite* – M) [2]. As depicted in Figure 1-1, forward MT often proceeds as a two-step transition from austenite to an intermediate trigonal so-called R-phase, which then transforms into martensite. The reverse transformation, is usually a one-step transition from martensite to austenite [2].

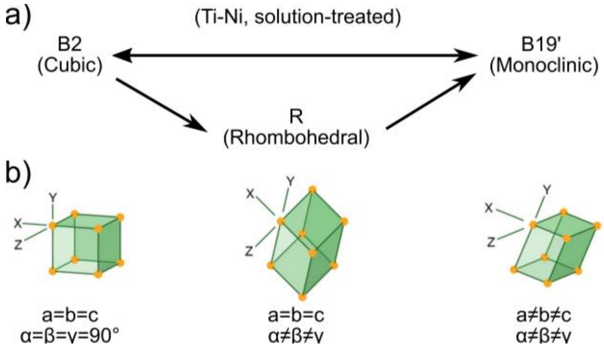

Figure 1-1: **a)** Transformation path in NiTi SMAs (adapted from [2]) and **b)** crystal lattices of different phases (adapted from Encyclopedia Britannica, Inc).

### 1.1.2 Stress-temperature diagram

The functional properties in NiTi SMAs depend on the path in the stress-temperature space. Several technological parameters affecting functional behavior were identified in the seminal work by S. Miyazaki [7]. The main factors are the Ni content, cold working, as well as ageing and annealing treatments [8]. SIMT in NiTi alloys was discovered later than TIMT [9]. The phase diagram was introduced in the early studies for TIMT [10] and then extended to different functional behaviors [11,12]. Figure 1-2-a shows simplified phase diagram (simplified Clausius-Clapeyron diagram) of a NiTi SMA in tension.

**TIMT** occurs during temperature changes: forward MT (A→M) upon cooling; reverse MT (M→A) upon heating. The stress-free thermally-induced martensite is said to be *twinned* or *self-accommodated* [13], i.e., formed by all martensite variants in equal proportions, leading to no macroscopic shape change of the SMA component compared to its shape in the austenitic state. Under the stress-free condition, A→M transformation starts and finishes at temperatures denoted $M_s$ (martensite-start) and $M_f$ (martensite-finish), respectively; whereas M→A transformation starts and finishes at temperatures denoted $A_s$ (austenite-start) and $A_f$ (austenite-finish) respectively. In Figure 1-2-c, the thermal hysteresis is represented by the quantity $\eta_t$.

**SIMT** occurs above $A_f$ and is triggered by mechanical loading. The forward transformation is initiated at the stress denoted $\sigma_M$ in the graph. The reverse transformation occurs upon unloading from a critical stress level $\sigma_A$ lower than $\sigma_M$. In Figure 1-2-b, the stress hysteresis is represented by the quantity $\eta_\sigma$. The stress-induced martensite is said to be *detwinned* or *oriented*, i.e., formed by a selection of martensite variants as a result of the applied loading direction. Relationships between transformation stresses and temperatures are linear: in the graph, $C_{AM}$ and $C_{MA}$ are equal to around 6 MPa.K$^{-1}$ in tension.

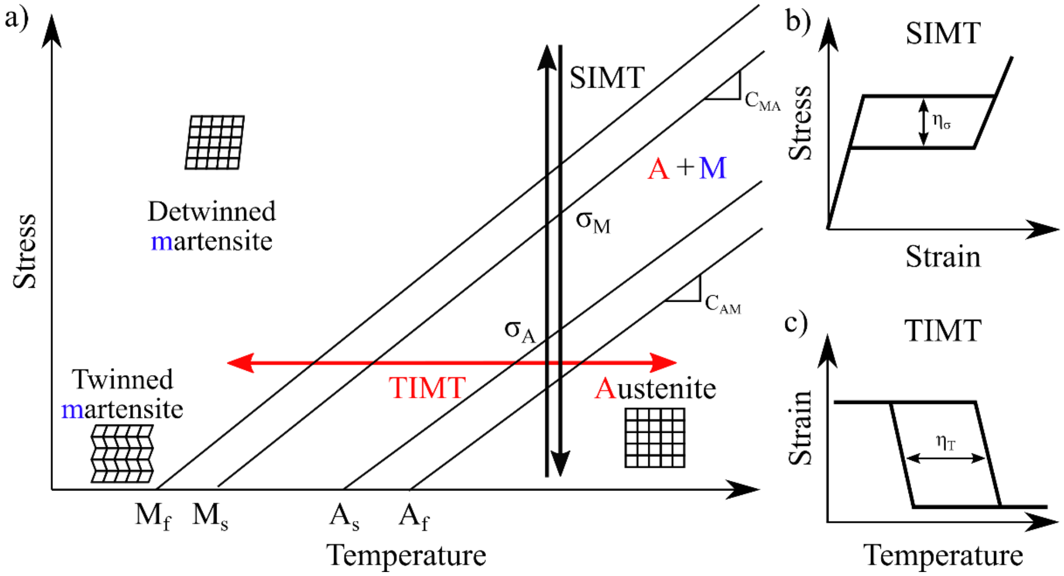

Figure 1-2: **a)** Simplified phase diagram, **b)** schematic stress-strain response during SIMT, **c)** schematic strain-temperature response during TIMT.

### 1.1.3 Superelasticity (SE)

The superelastic effect refers to the ability to exhibit large reversible strains (up to 11% in certain NiTi SMAs) at temperatures above $A_f$ thanks to the *transformation strain* arising from distortion of martensite lattice with respect to the austenite lattice [14]. The typical "isothermal" SE cycle in the stress-strain diagram is presented in Figure 1-3. It can be described in a simplified manner as follows.

- First, the externally applied load induces a linear elastic deformation of austenite.
- Then, the A→M occurs at nearly constant stress, forming thus the upper *stress plateau*.
- When the SMA specimen is fully transformed into (twinned/oriented) martensite, linear elastic deformation of martensite occurs upon further loading.
- Upon unloading, the response of the martensite is first elastic.
- Then, the reverse MT occurs at nearly constant stress, forming thus the lower stress plateau.
- The mechanical cycle ends with the elastic behavior of the austenite.

Note that the plateau stresses increase linearly with temperature. For a room temperature of 20°C, the mechanical response of the tested NiTi wire appears to be almost reversible, with a transformation strain of about 6% (see the "length" of the stress plateau). It can be observed that the reversibility is progressively lost when increasing the test temperature: see the recovered strains at 60°C and 80°C. The unrecovered strain can be firstly associated with a non-fully reversible phase transformation. This was demonstrated by Brinson et al. [15] from microscopic observations: residual martensite is observed at the end of the mechanical cycle. Secondly, irreversibility is also due to plastic deformation processes [16]. The part of the unrecovered strain due to residual martensite can be recovered by overheating the SMA specimen well above $A_f$ [17].

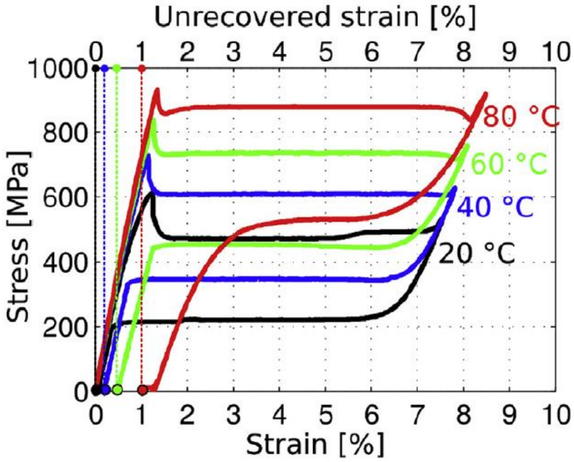

Figure 1-3: Superelastic response of a NiTi wire (image taken from [18]).

**Cyclic effect on SE from a virgin SMA specimen**

It has often been reported in the literature that repeated SE cycles applied to a virgin SMA specimen are showing ratcheting [19–26]. This effect is referred to as *functional fatigue* (the term was introduced by G. Eggeler [27]). As depicted in Figure 1-4 from Ref. [26]), the hysteresis area of the stress-strain curves decreases and the unrecovered strain increases over the cycles, up to stabilization. SE cycles are also displayed in Figure 1-5-a from Ref. [19]). The evolution of the specific dissipated energy per cycle is presented in Figure 1-5-b for 11,000 cycles. A great dissipation of energy is evidenced during the stabilization of the MT. This reveals irreversibility associated with microstructural changes.

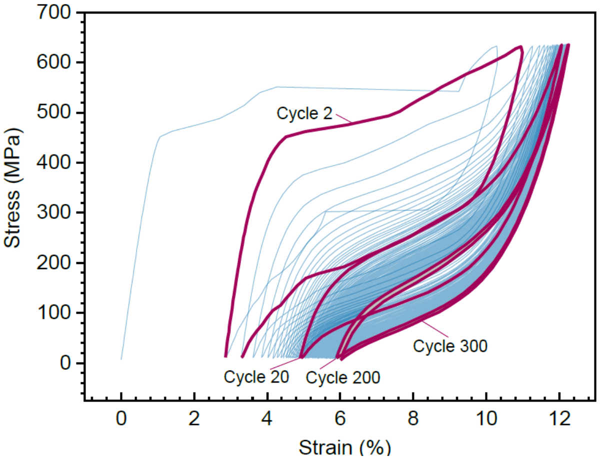

Figure 1-4: Stress-strain curves of NiTi during cyclic tensile loading (image taken from [26]).

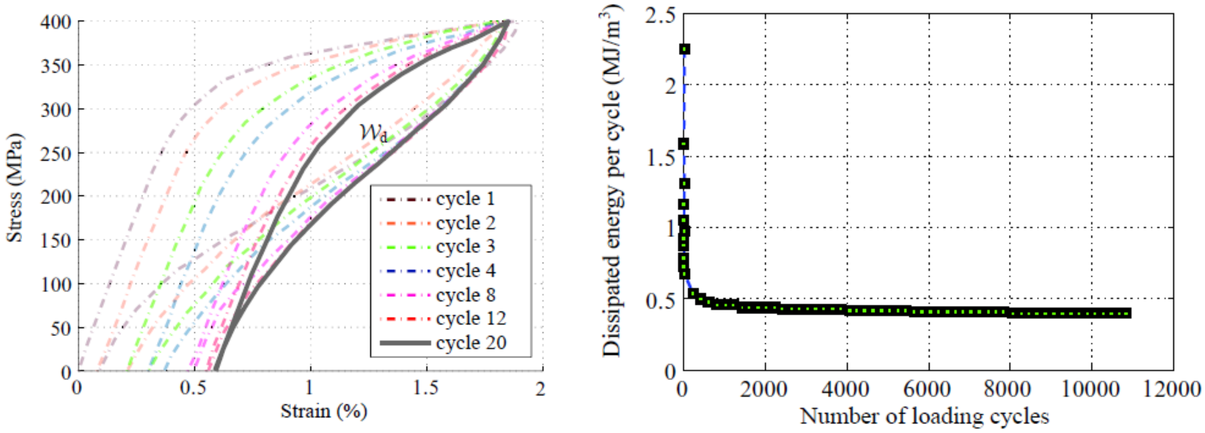

Figure 1-5: **a)** SE cycling for twenty cycles, **b)** dissipated energy per cycle versus the number of loading cycles (image taken from [19]).

### Transformation localization

SIMT in NiTi wires, stripes and ribbons in tension proceeds usually in a localized manner. A Lüders-type deformation is reported for polycrystalline specimens (see for instance Refs [2,28]). Localized stress-induced transformation occurs by nucleation and propagation of macroscopic shear bands, also referred to as *martensite band fronts* (**MBFs**). The MT onset corresponds to the sharp stress peak observed in the macroscopic strain-stress curve. As depicted in Figure 1-6, the specimen geometry determines the shape of the shear band [29–33]. For flat specimens such as plates, strips and ribbons, MBFs are inclined at an angle between 51° to 67° with respect to the longitudinal direction [32,34,35]: see Figure 1-6-a. For wires, a conical MBF was evidenced by 3D-XRD [29]: see Figure 1-6-b.

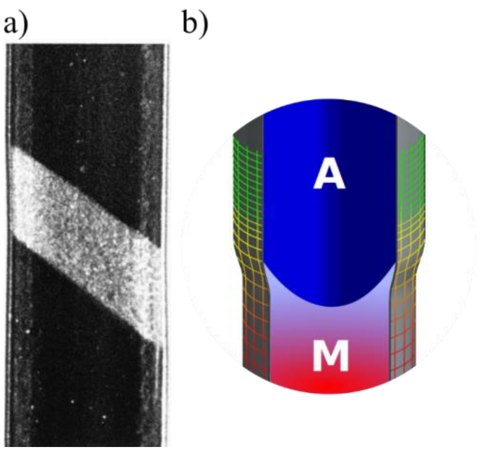

Figure 1-6: Shape of the shear band in NiTi in tension: **a)** in wire [29], **b)** in strip [34].

### 1.1.4 Shape memory effect (SME)

SME refers to the ability to memorize a shape fixed during a thermomechanical treatment [36]. An SMA specimen stretched in a martensite state (i.e., at "low" temperature) is apparently permanently deformed. To return to the original shape under stress-free condition, the specimen must be heated above $A_f$. This one-way shape memory effect (OMSME) can be described by the thermomechanical cycle presented in Figure 1-7:

- stress-free cooling from a temperature higher than $A_f$ (austenite state) to a temperature lower than $M_f$ in order to create twinned/oriented martensite (path 4–1);
- loading (at a temperature lower than $M_f$) above the critical stress needed to "detwin" the martensite (path 1–2);
- unloading (still at a temperature lower than $M_f$), leading to a residual strain (path 2–3);
- stress-free heating above $A_f$ to transform into austenite and recover the residual strain (path 3–4).

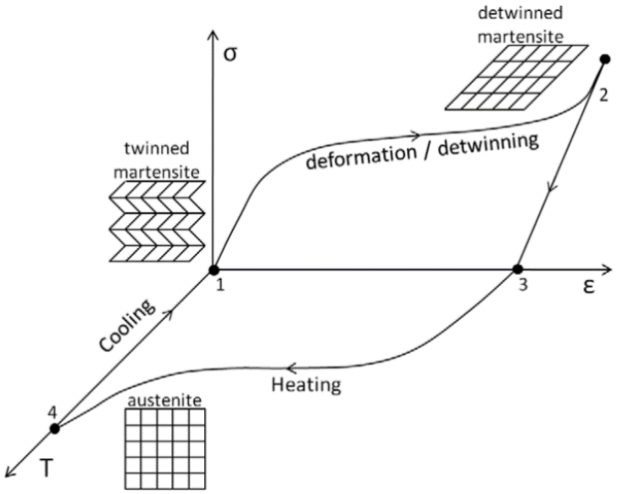

Figure 1-7: Schematics of the shape memory effect in the stress-strain-temperature ($\sigma - \epsilon - T$) diagram (image taken from [37]).

**Stress effect on TIMT**

Functional fatigue is observed also for thermal loading under mechanical load. Figure 1-8 shows the effect of the stress level during a thermal loading from a virgin specimen. It shows firstly the stress effect on the shgift of transformation temperatures. It can be secondly noted the strong increase of the hysteresis area and of the residual strain above a certain level of stress (see the difference between the curves at 287 MPa and 379 MPa).

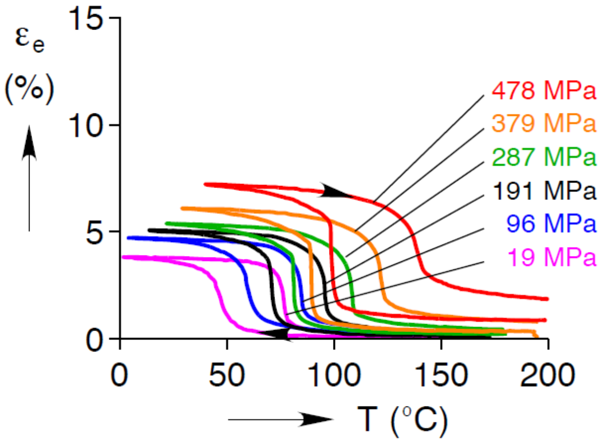

Figure 1-8: Effect of the stress on the thermally-induced martensitic transformation (image taken from [38]).

Figure 1-9 also shows the effect of thermal cycling at constant stress. The latter causes the martensite to orient itself in a preferred direction [39]. A decrease of the hysteresis in the strain-temperature plane without apparent shift of the transformation temperatures can be observed. Thermomechanical training induced by plastic deformation leads to a stabilization of the specimen shape both in austenitic and martensitic states. Therefore, even in macroscopic stress-free condition, large reversible deformations can be triggered by thermal cycling. This is the so-called two-way-shape-memory-effect (TWSME) [39].

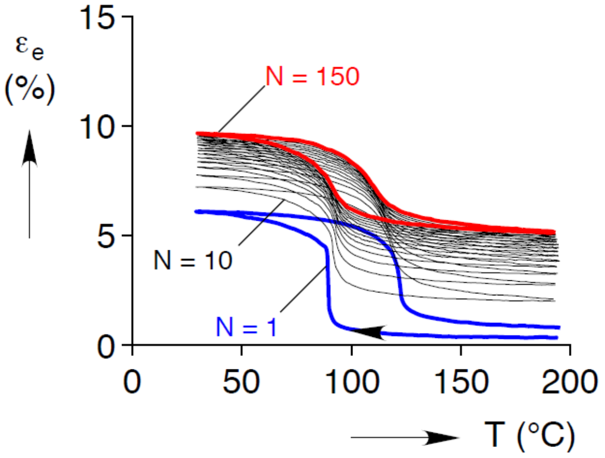

Figure 1-9: Effect of thermal cycling at constant stress (image taken from [38]).

### 1.1.5 Heat effects on the superelastic response

The phase change that occurs in NiTi SMAs is a thermodynamical evolution of a material system from a state A to a state B [40]. In that process, the internal energy change is not equal to the mechanical work spent. The difference between internal energy change and mechanical work is a heat quantity, namely the latent heat. The forward and reverse MT are exothermic and endothermic, respectively. In a stress-free condition, differential scanning calorimetry (DSC) is classically used to measure the involved heat quantities and the phase transition temperatures. In practice, the latent heat is the integration of the DSC curve in the colored zones in Figure 1-10. The latent heat depends on the SMA composition [41] (and obviously on the fraction of the product phase [26,42]).

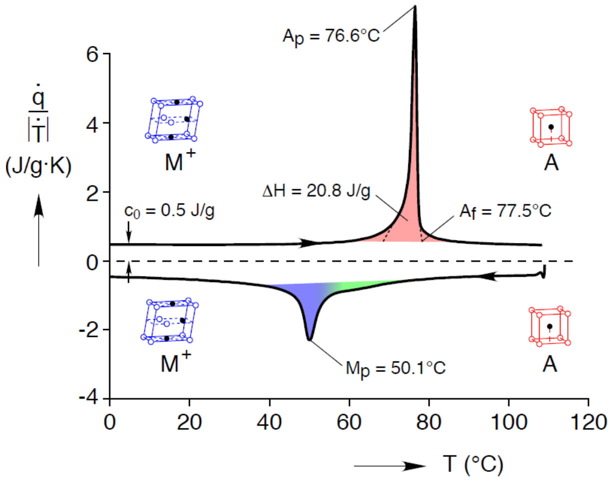

Figure 1-10: DSC curve of a stress-free NiTi specimen (image taken from [38]).

In the case of SIMT, the latent heat implies *self-heating* and *self-cooling* during the loading and unloading, respectively [30,43,44]. Depending on the mechanical loading rate, the temperature changes may directly influence the SE response as MT is a strongly temperature-dependent deformation process [23,45–47].

For quasi-static tensile tests (see Figure 1-11-a), no substantial temperature changes are induced by the phase change. Indeed, heat is exchanged with the specimen's surroundings (see for instance Ref. [48]). High-rate mechanical tests are more complex to analyze due to temperature changes of the material along the test, as analyzed for instance in Refs [31,46,47,49–52]. In particular, localized phase transformation leads to non-homogeneous temperatures within the specimen. Moreover, higher stresses are required upon loading for the forward transformation, and both stress "plateaus" are inclined (see Figure 1-11-b) as a consequence of these thermomechanical couplings.

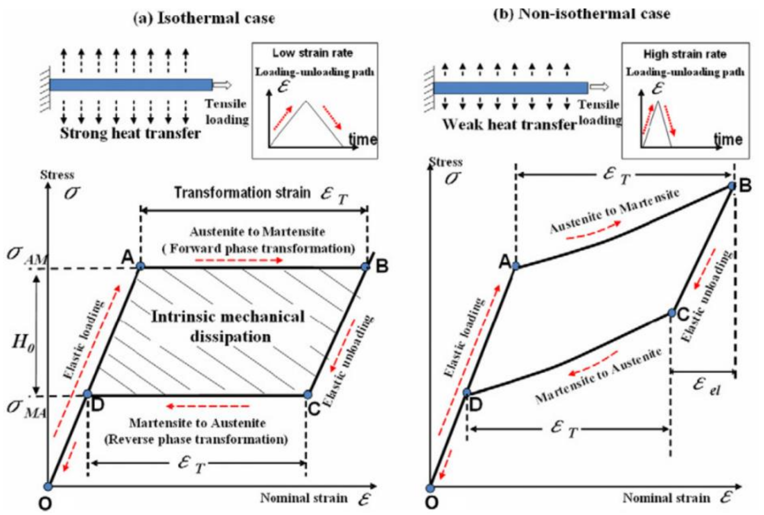

Figure 1-11: Comparison of tensile SE curves schematically depicted for **a)** isothermal loading conditions and **b)** non-isothermal loading conditions (image taken from [46]).

### 1.1.6 High damping capacity

The mechanical hysteresis is associated with the work spent to perform loading-unloading cycles. According to the first principle of thermodynamics, this energy is the sum of the dissipated heat and work stored within the material. This physical principle can be used to dissipate the work of vibrating objects that are to be damped. The analysis of this effect is in a growing field of applications, especially for civil engineering (see for instance Ref. [53]). Due to the self-heating issue discussed earlier, the damping capacity strongly depends on the excitation frequency. From Figure 1-12 showing the amount of dissipated energy at different strain rates, it was possible to determine an optimal rate. In the same study, different environmental conditions have been investigated by imposing different wind speeds around the specimen. It was shown that the increase of the heat exchanged by convection shifts the dissipation peak to higher strain rates. Therefore, SMAs are an excellent candidate to be used as a passive dampener.

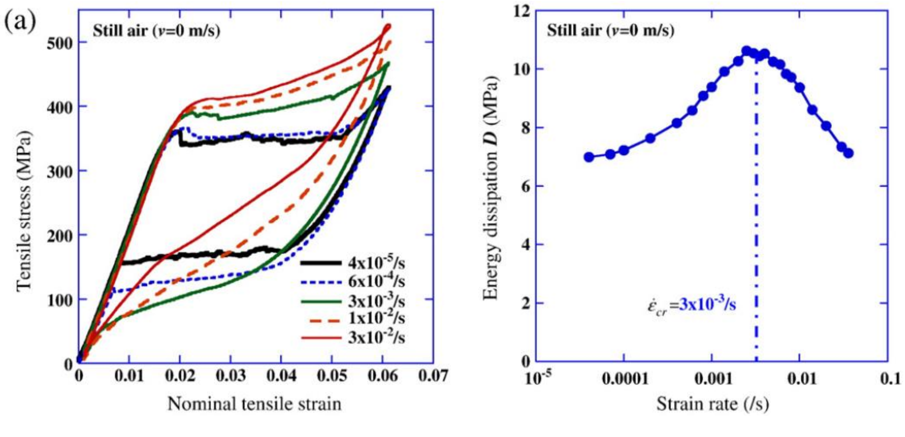

Figure 1-12: Strain rate dependency of the NiTi mechanical behavior (image taken from [45]).

### 1.1.7 The elastocalorific effect

The heat effect induced during SE is also referred to as the elastocaloric effect (ECE) [54,55]. It is in particular considered for use in solid-state refrigeration applications. The large difference in temperature change between the exothermic and endothermic reactions makes NiTi alloy an excellent candidate for such applications (see Figure 1-14).

For example, Figure 1-13 shows four steps refrigeration cycle of the device proposed by Tusek et al. [54]: a) the mechanical loading induces the forward MT and a fluid in contact with SMA components is heated by the exothermic reaction; b) the hot fluid flows out to the heat exchanger while a cool fluid replaces it; c) mechanical unloading triggers reverse MT and the fluid in contact with the SMA components is cooled by the endothermic reaction; d) the cooled fluid is carried to the system to cool, etc.

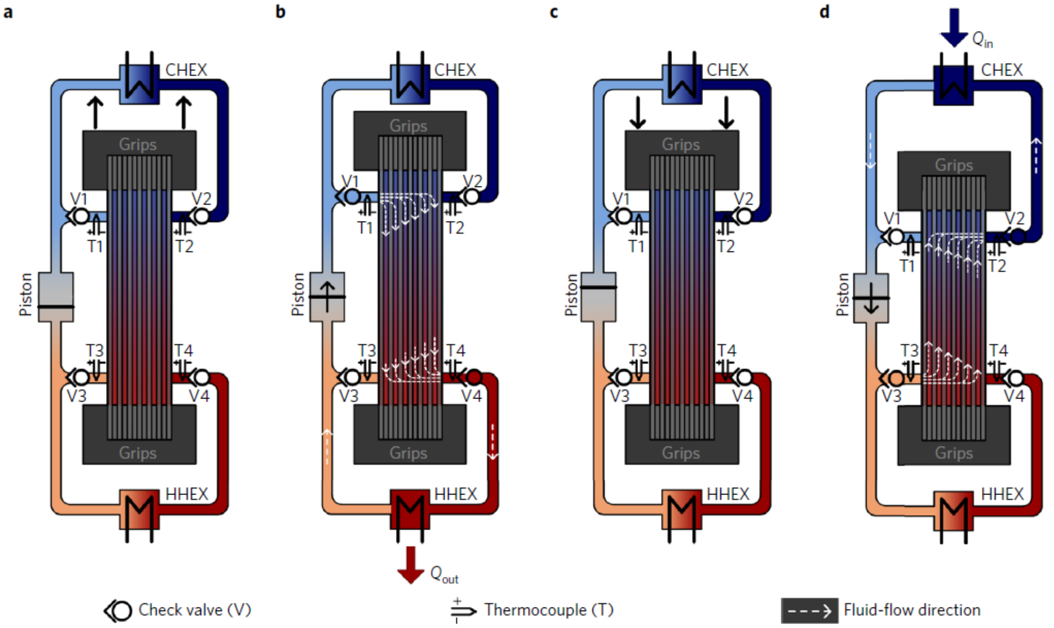

Figure 1-13: Illustration of four operational steps of an SMA-based elastocaloric device (image taken from [54]).

The coefficient of performance (COP) is classically used to evaluate the efficiency of a cooling system. It is expressed as the ratio of the amount of the heat ($Q$) extracted from the reservoir over the work ($W$) over a cycle: COP = $Q/W$ [54]. To enhance the efficiency, $W$ should be as low as possible, i.e., the hysteresis of the stress-strain curve should be minimized. Figure 1-14 presents a comparison of COP values for different promising materials for solid-state refrigeration technology: the magnetocaloric, elastocaloric, electrocaloric and thermoelectric effects are considered. The Carnot limit represents the maximal COP reachable, about 28 [56]. Elastocaloric materials appear to be the second most promising category of caloric materials. Note that the use of refrigerants in refrigerators corresponds to COP values between 3 to 5 [57].

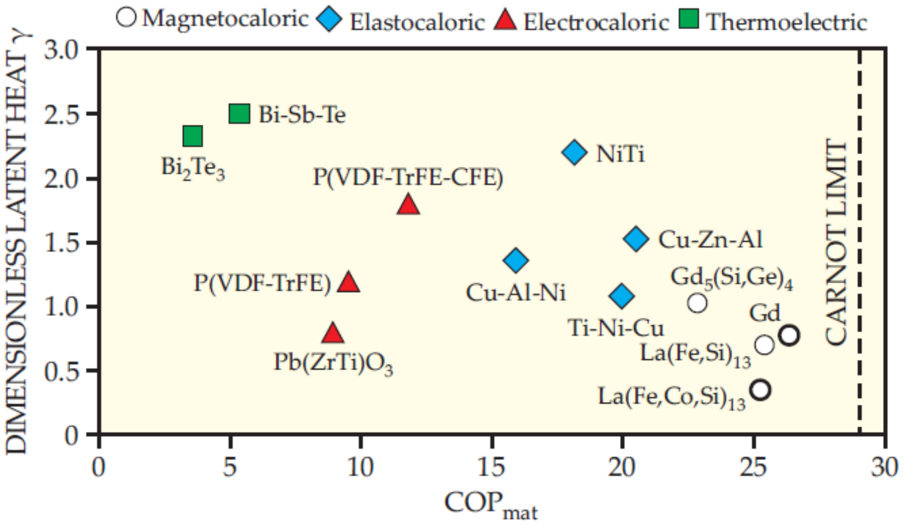

Figure 1-14: Coefficient of performance (COP) versus dimensionless latent heat for various caloric materials (image taken from [56]).

### 1.1.8 Microstructural effects

Different mechanical responses of SMAs can be observed in materials of the same chemical composition [7,58,59] depending on the parameters of the heat treatment that have to be considered in the design of SMA applications.

**Heat treatment effects**

NiTi SMAs are mainly produced and used in the form of wires [8]. Manufacturers deliver them either in straight annealed or cold worked state as semi-finished products extruded through multiple hot working passes, a final cold working. The final heat treatment can or do not have to be applied and the wires are then delivered in so cold as drawn or straight annealed state, respectively. The properties of as drawn wires can be controlled via customized heat treatment. For instance, the effect of the final treatment (annealing) was analyzed in Ref. [60]: see Figure 1-15. Without annealing, the material does not exhibit functional properties (absence of SE in the stress-strain curve in Figure 1-15-a). In this study, non-conventional heat treatment was used: electrical impulse (pulse duration of a few milliseconds). Figure 1-15-b–h shows that the increase in treatment temperature that scales with pulse duration leads to drastically coarser grains. The optimal treatment was determined to obtain a stable superelastic property: see Figure 1-15-e. The general effect of annealing is the combination of three processes: recovery, recrystallization and grain growth [61]. It results in a release of internal stresses and softening of the material. However, if the annealing temperature is too high, dislocation slip occurs after repeated tension cycles with large permanent deformation (see Figure 1-15-h). This study shows the importance of grain size control in NiTi alloys to tune the balance between functional behavior and mechanical performance.

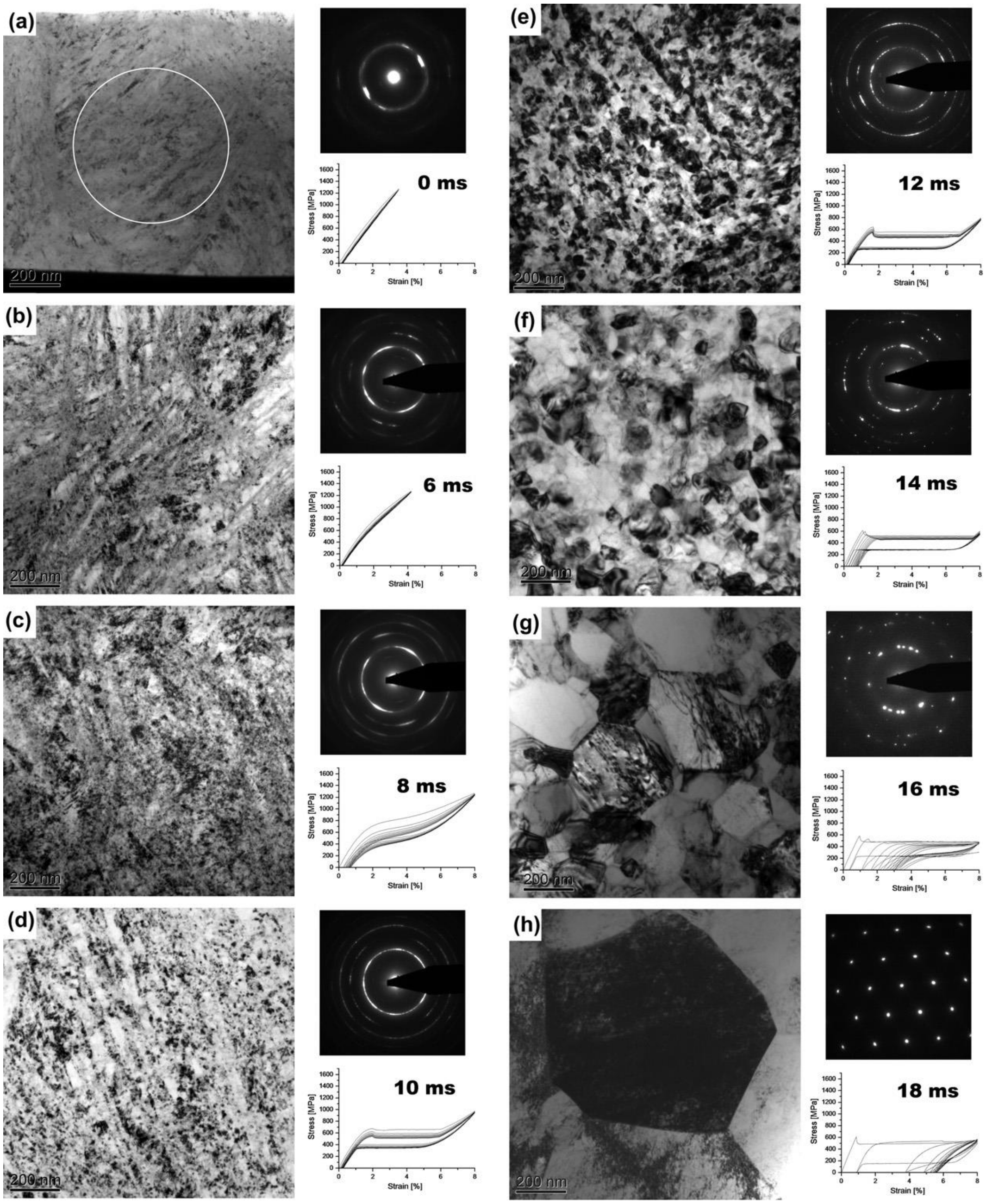

Figure 1-15. Microstructure and corresponding functional properties in NiTi wires heat-treated by an electrical impulse of a few milliseconds (image taken from [60]).

Only a few in-situ studies of the microstructure evolution under mechanical loading were reported in the literature. Usually, initial and final microstructures are compared from different specimens (for instance in Ref. [25]). Reference [15] describes the microstructural changes in a single specimen after specific cycle numbers, enabling to see the evolution of specific transformation sites: see Figure 1-16. At each mechanical cycle, a small amount of strain remains and accumulates. One can observe that, cycle after cycle, grain boundaries are more and more visible, which may indicate the occurrence of dislocation slips. This form of plasticity explains the non-reversible strain. Also, the striae within the grains (known as *twins*, which are the way the martensite appears) are more and more pronounced cycle after cycle, evidencing that the phase transformation cycle is not fully reversible.

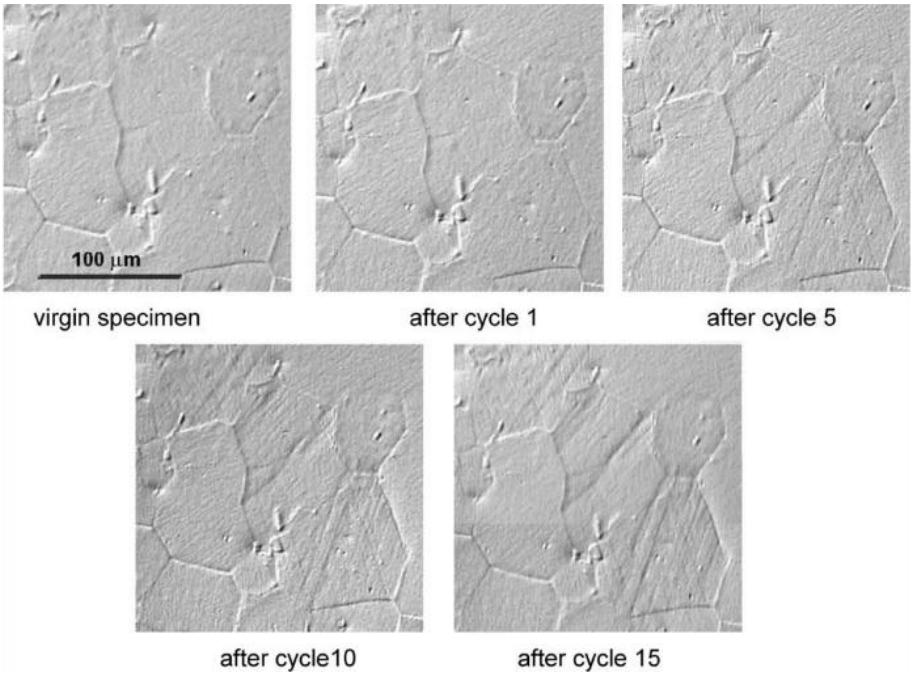

Figure 1-16: Accumulation of localized plastic deformation within the grains and of residual martensite during SE cycles (image taken from [15]).

### 1.1.9 Full-field thermomechanical observations

The localized behavior of NiTi polycrystalline SMAs can be tracked using displacement and temperature full-field measurements by cameras. For instance, the use of visible-range pictures processed by Digital Image Correlation (DIC) enables measurement of strain fields. InfraRed Thermography (**IRT**) enables basically to measure temperature fields. See for instance Refs [43,62,63] about these techniques, which give a better overview of the heterogeneous events occurring in NiTi SMAs as well as their local quantitative thermomechanical measurements.

For instance, Figure 1-17 presents the spatio-temporal strain and temperature fields for five SE cycles applied to a virgin NiTi wire. Due to the elongated shape of the specimen, data are presented in the form of one-dimensional (1D) profiles evolving along the time: let us say a “1D+time” field. Thanks to full-field measurements, mechanical and thermal effects were analyzed along the wire axis during the mechanical test at constant ambient temperature:

- In the averaged stress response (black line) obtained from DIC measurement, one can see various typical macroscopic features of the mechanical response of the NiTi specimen, e.g. various stress drops and peaks.
- From the 1D strain profiles, it can be seen that the specimen did not transform fully during the first cycle (see the bottom part of the specimen remaining at low strain, i.e. in the austenitic state). In the subsequent cycles, the transformation is complete. It can be noted that MT nucleation occurs within the upper jaw during the first and second cycles. Then it occurs within the two jaws during the third and fourth cycles. Three nucleation zones are visible for the fifth cycle.
- In the 1D thermal profiles, the exothermic and endothermic reactions are evidenced in the form of fronts during forward and reverse transformations, respectively.

This study shows that simultaneous mechanical and thermal measurements give a better insight of the local thermomechanical response, in particular the competition between heat effect and mechanical effect (leading to different “MT patterns” along the SMA wire in terms of the number of nucleation sites and MBFs).

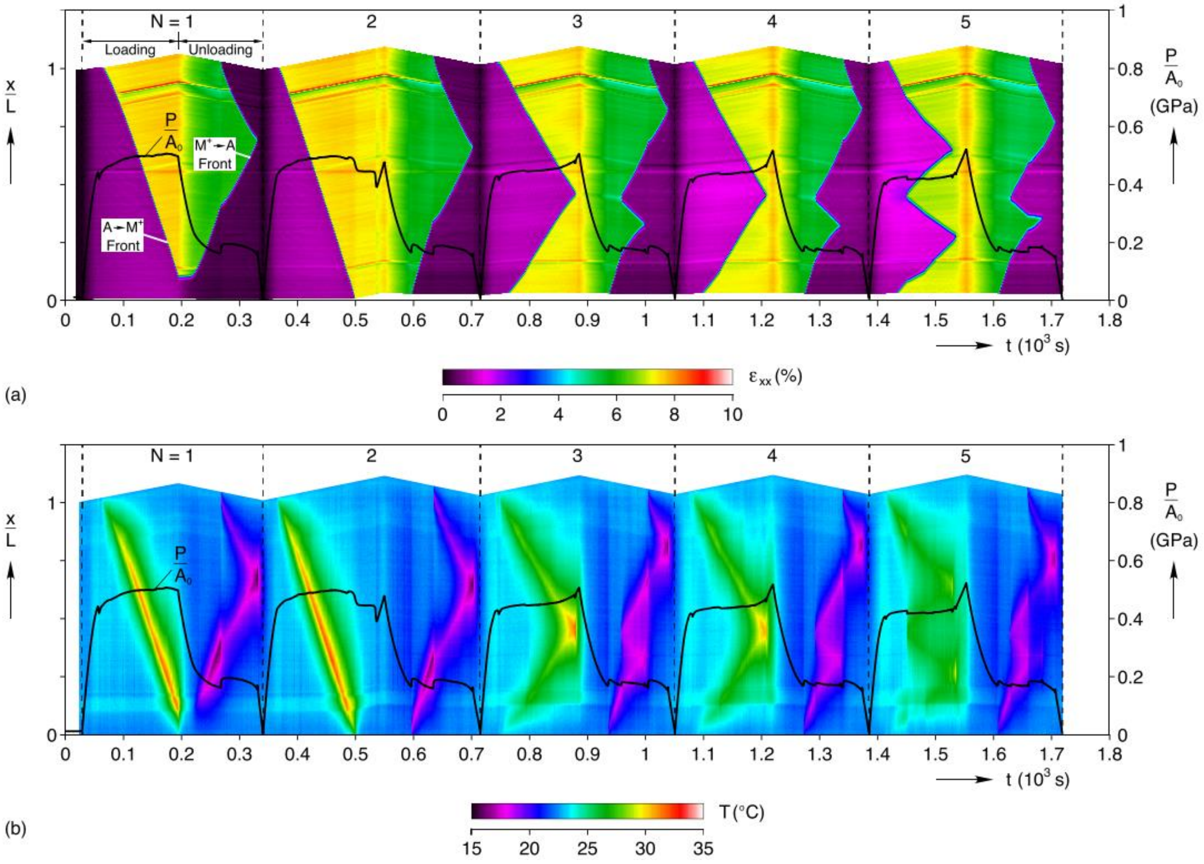

Figure 1-17: The five first loading-unloading cycles of a virgin NiTi wire: a) spatio-temporal strain field b) spatial-temporal temperature field (image taken from [29]).

Finally, while strain field and force measurements provide quantitative data for the calculation of the local mechanical fields, thermal measurement requires an adapted post-processing method in order to extract “calorimetric” information. The next section is dedicated to a state of the art of the different calorimetric methods to extract quantitative heat information from temperature data.

## 1.2 Deformation calorimetry methods

### 1.2.1 Introduction

Since the finding of Lord Kelvin [64], we know that a material that undergoes a process of deformation in an elastic regime sees its temperature change. This phenomenon is described as an isentropic process. In the case of metallic materials, the application of a load causes the temperature to decrease, while unloading causes it to increase [65]. This effect is also known as *thermoelastic coupling* and is a reversible thermodynamical process.

Later, in his seminal article on the *thermodynamics of irreversible processes* (TIP), Lord Kelvin [66] introduced the notion of irreversible processes: "*when heat is created by an irreversible process, mechanical energy is dissipated, and a complete restoration of this energy to its primitive state is impossible*". A key to assessing mechanical dissipation is to propose a system for quantifying heat from temperature data. Calorimetry encompasses the different techniques that allow us to meet this challenge. Calorimetry is a field in constant improvement that offers new technological solutions to researchers and engineers [67]. The best known and most widespread system is the Differential Scanning Calorimeter (DSC). Improved versions have been proposed: Temperature Modulated Differential Scanning Calorimeter (TMDSC), step-DSC and recently IR calorimeter [68]. However, most of the different solutions proposed are based on a measurement on a material specimen not subjected to a mechanical load: the specimen is confined in an enclosure minimizing heat exchanges with the outside. For the measurement under mechanical loading (deformation calorimetry – DC), several devices have been proposed over the last decades.

In Section 1.2, we will present a state of the art of the deformation calorimeters that have been developed and we explain the motivations that have driven the researchers in their endeavors. To estimate heat, temperature values are required. So, the next section presents first the different temperature measurement technologies that are available.

## 1.2.2 Measurements of temperatures in solids

### 1.2.2.1 Contact temperature measurement

Affixing a temperature measuring means such as a thermocouple at the specimen surface inserts a certain number of uncertainties that are difficult to evaluate, such as the positioning, fixation and thermal conduction of the junction [69]. Two configurations are presented in Ref. [70]:

- The first possibility is to weld the thermocouple on the metallic object (see Figure 1-18-a), which has several disadvantages. The welding process can alter the thermocouple properties and alloying with the specimen may occur. Moreover, specimen microstructure can be changed too, thus creating an uncontrolled microstructural heterogeneity.
- A second possibility consists in gluing the thermocouple at the surface of the object (see Figure 1-18-b), which inserts many sources of uncertainties such as a bad thermal contact induced by the glue or a loss of contact during the object deformation.

In the case of significant deformations of the object, adherence of the thermocouple cannot be perfect and undesirable motion of the thermocouple cannot be avoided. In regards of the uncertainties of temperature measurement by contact, contactless techniques are preferable.

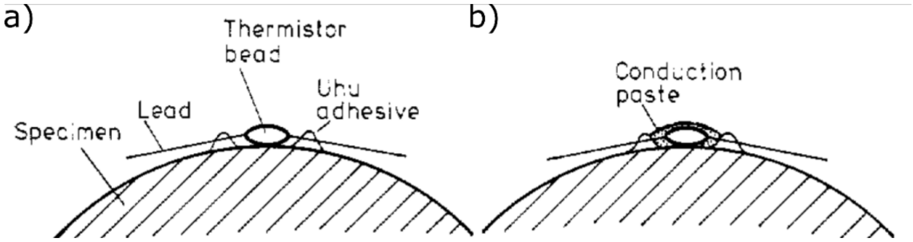

Figure 1-18: Technique to establish a thermal contact between an object and a thermocouple: **a)** by welding, **b)** by gluing (image taken from [70]).

### 1.2.2.2 Infrared temperature measurement

The following information on InfraRed Thermography (IRT) is taken from the handbook of Vollmer and Möllman [71].

**Infrared radiation**

IR thermography is based on the measurement of electromagnetic waves with wavelengths between 1.7 µm and 14 µm: see Figure 1-19. Indeed, it has been observed that any object whose temperature is higher than 0 K emits energy in the IR range. The radiation power $\phi_\lambda$ depends on the wavelength $\lambda$, the temperature $T$ and the material properties. It can be is estimated by the so-called Planck's law:

$$\phi_\lambda = \frac{C}{\lambda^5} \frac{1}{e^{\left(\frac{c}{\lambda}T\right)} - 1} \tag{1-1}$$

where $C$ and $c$ are the first and second radiation constants. It should be noted that this law was established for a *black body*, i.e., a body that emits IR radiation due to its own temperature (no IR radiation reflection from the environment, and no IR radiation transmission through the object from its background). In practice, black bodies have a *thermal emissivity* $\epsilon$ equal to 1 (see below). A body whose emissivity value does not depend on the wavelength $\lambda$ within a certain range is named a *gray body*.

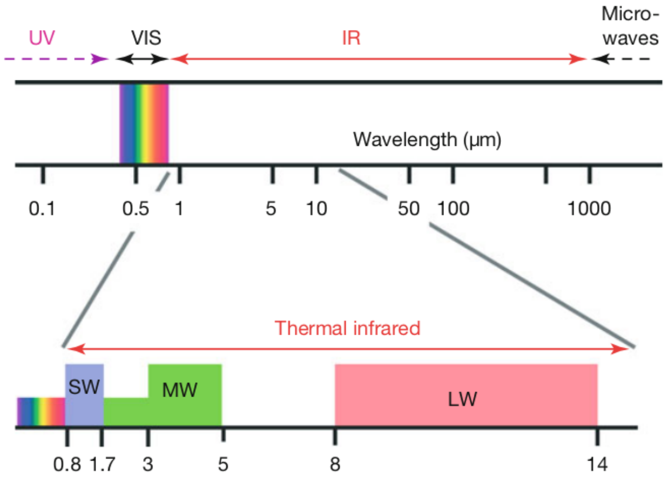

Figure 1-19: Infrared (IR) and adjacent spectral regions. Wavelength domains used in IR imaging systems: short-wave (SW), mid-wave (MW), and long-wave (LW) (image is taken from [71]).

**Kirchhoff's law**

Black bodies are idealized objects. The thermal emissivity $\epsilon$ of an object can be defined as the ratio between the IR radiation it emits, and the theoretical radiation given by Planck's law. $\epsilon$ is comprised between 0 and 1. In practice, one must consider not only the IR radiation of the object observed due to its own temperature, but also the IR radiation of the environment reflecting on it, the IR radiation of background in the case of semitransparent object, and the absorption by the media (generally air) through which the IR radiation passes to the camera. When the absorption in the air is negligible (this is the case in practice), Kirchhoff's law is:

$$\phi = \phi_R + \phi_B + \phi_E \tag{1-2}$$

where the indices $R$, $B$ and $E$ stand for reflection, background, and emission, respectively. For many solid materials, $\phi_B$ is null (opaque body). So, the radiation measurement by the thermographic system is the sum of the reflected and emitted radiations. The radiation can be known from the use of the Stefan-Boltzmann equation:

$$\phi_E = \sigma \, \epsilon \, T^4 \tag{1-3}$$

where $\sigma$ is the Stefan-Boltzmann constant. Kirchhoff-Draper's law allows us to establish a relationship between the emissivity and the absorption of a body, and to assume that they are equal. For $\phi_B = 0$, it comes

$$\phi = \sigma \, \epsilon \, T^4 + (1 - \epsilon) \, \sigma \, T_e^4 \tag{1-4}$$

where $T_e$ is the temperature of the environment. It is thus necessary to know the thermal emissivity $\epsilon$ of the material surface. The calibration of the IR system is usually performed by the manufacturer of the IR camera.

### IR imaging system

IR detectors are transducers that convert IR radiation at wavelengths within their sensitivity range into electrical signals. There are two types of IR detectors: *photon detectors* and *thermal detectors*. In general, photon detectors have better performance with reduced integration time, better sensitivity, and reduced noise compared to thermal detectors. However, systems integrating such detectors are more expensive and require cooling to a temperature close to that of 77 K liquid nitrogen for proper operation. Nowadays, the current cameras integrate a sterling engine and keep it at a constant temperature. For the application in the present research work, being the quantitative characterization of NiTi SMA specimens, an IR camera with integrated photon detectors has been used.

### NETD

An IR thermographic system can be characterized by the so-called *Noise Equivalent Temperature Difference* (NETD) and the spatial resolution of the thermal images. NETD corresponds to temperature resolution (measurement resolution). This quantity gives the minimum detectable temperature variation. Experimentally, NETD is determined by analyzing the temperature fluctuations at a pixel observing a black body set at a given stabilized temperature. The NETD is equal to one standard deviation of the Gaussian probability density function of the deviation from the mean (see Figure 1-20).

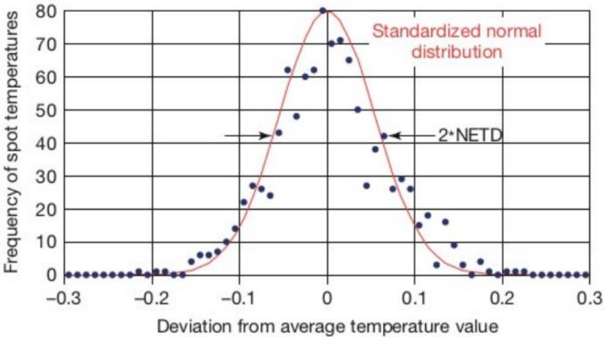

Figure 1-20: Probability density function of the thermal noise. NETD corresponds to one standard deviation of the distribution (image taken from [71]).

### NUC

For quantitative measurements of temperature fields, a Non-Uniformity Correction (NUC) procedure is required. Indeed, an IR thermographic system integrates a focal plane array (FPA) of detectors having each one its own response. The procedure consists of two steps, as depicted in Figure 1-21. An offset correction is applied to each detector by considering an a priori homogeneous temperature field. Then, the slope of the signal to the radiative power is corrected for each detector. An additional step is finally performed: offset correction again.

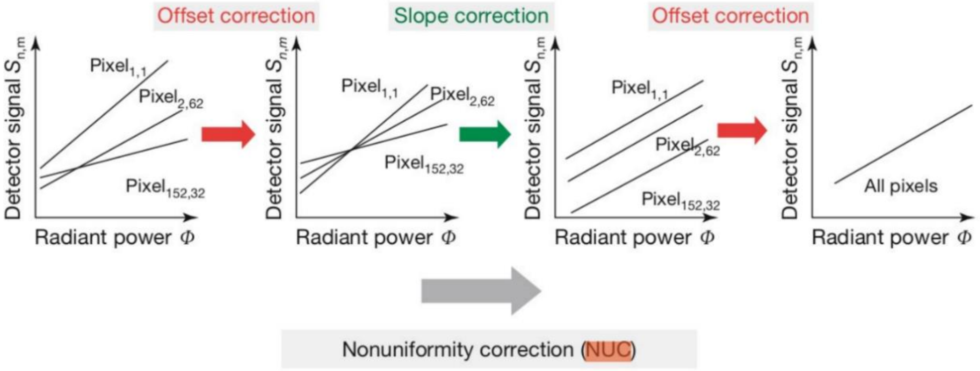

Figure 1-21: Non-Uniformity Correction procedure (image taken from [71]).

### Guideline for IR measurements

Regarding the information presented previously, different points must be taken into account in order to guarantee quantitative thermal image acquisition:

- The emissivity $\epsilon$ of the surface of the object must be known. Within the framework of characterization of metallic materials, it is advisable to use high emissivity paints ($\epsilon > 0.9$) to be applied before the measurement.
- The temperature $T_e$ of the environment must be known.
- A waiting time is necessary after switching on the IR camera. The stabilization of the acquisition can be checked by consulting the internal temperature of the camera or of a dummy specimen being at a constant temperature.
- The NUC procedure must be systematically performed before each measurement to ensure uniformity of detector responses. The NETD must be then estimated.

### 1.2.3 Deformation calorimetry

Historically, the method of deformation calorimetry (DC) has been developed to characterize the work stored in a metallic specimen subjected to cold working [72,73]. Part of the plastic work is indeed dissipated in the form of heat, the remaining part is stored in the material. The process of energy storage occurs during the manufacturing process (e.g. a drawing). The presence of residual stresses induced by the process [74] creates microstructural instabilities [75] that can be released in a subsequent thermal or mechanical process.

In contrast to conventional calorimetry (DSC), there is no commercial apparatus or standard for "deformation" calorimetry. Some devices have been developed in research institutes.

**Energy storage**

During the plastic deformation process, the plastic work $W_p$ is partially dissipated in the form of heat ($Q_p$), the remaining part being stored within the material ($E_s$):

$$W_p = E_s + Q_p \tag{1-5}$$

So:

$$E_s = W_p - Q_p \tag{1-6}$$

The plastic work $W_p$ can be estimated from the measured stress-strain curve. But the measurement of $Q_p$ is not straightforward. Information about the calculation of $Q_p$ from temperature measurement is given below.

**History of Taylor-Quinney coefficient**

One of the first reported applications of deformation calorimetry was carried out by Farren and Taylor [73]. In this study, fast loading was applied followed by temperature measurement ex-situ in order to evaluate the heat resulting from the deformation. The portion of the heat generated during plastic deformation of a twisted rod of metal (steel and copper) was estimated at 90%. In the second known report, by Taylor and Quinney [76], the estimation was carried out up at different levels of strain to estimate if the portion is constant or not. They proved that it is not constant and tends to drop above a certain level of strain. Nowadays, the ratio of dissipated heat over plastic strain energy is referred to as the *Taylor-Quinney coefficient*.

A large collection of calorific data from the first half of the 20th century are presented in the extensive review paper by Bever et al. [75]. The two groups of DC approaches based on thermal measuring devices are the single-step and two-step methods [75]. The single-step method consists of measuring continuously the heat produced along a mechanical test. As an example, Figure 1-22 presents the system proposed in Ref. [77] to evaluate the stored energy during a shear test. The device was integrated into an Instron machine and the specimen (a copper single crystal) was attached at its ends to nylon pull rods. The specimen was electrically insulated and installed in a tube connected to a vacuum pump to thermally insulate the specimen as well. The temperature measurement was carried out by a thermocouple welded at the center of the specimen. The two-step method is based on the measurement of heat *after* the mechanical loading: see Ref. [78] for details.

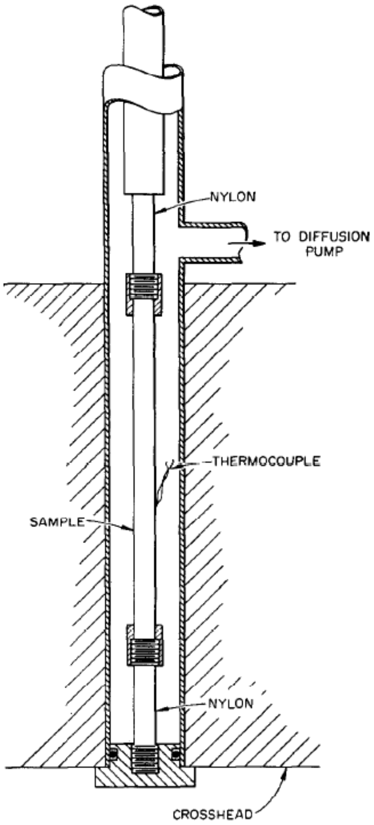

Figure 1-22: Setup for the one-step measurement of the stored energy in single crystals (image taken from [77]).

#### 1.2.3.1 “Micro-calorimeter”

In a so-called “*micro-calorimeter*”, thermocouples are embedded within the chamber wall instead of being in contact with the specimen to be characterized, which is thus less invasive than the setup presented in Figure 1-22. One of those devices is presented and detailed in the first study by A. Chrysochoos [69,79]. The schematics of the experimental environment and the calorimeter itself are shown in Figure 1-23. One of the key points to be noted is the attention paid to maintain constant environmental conditions to guarantee good repeatability: see air conditioners, fans and heaters in Figure 1-23-a. Figure 1-23-b is a schematic view of the calorimeter itself. The specimen (in the center of the drawing) is inserted in the micro-calorimeter and is in contact with PVC insulation. The thermocouples are placed in series and alternately inside and outside the wall chamber. Therefore, the electrical potential difference measured at the ends of the series of thermocouples is proportional to the thermal imbalance between the inside and outside temperatures of the chamber. The heat calculation is based on the measured electrical potential difference, the temporal characteristics of the chamber, the temporal characteristics and a sensitivity constant depending on the specimen under test; for more information see Ref. [69].

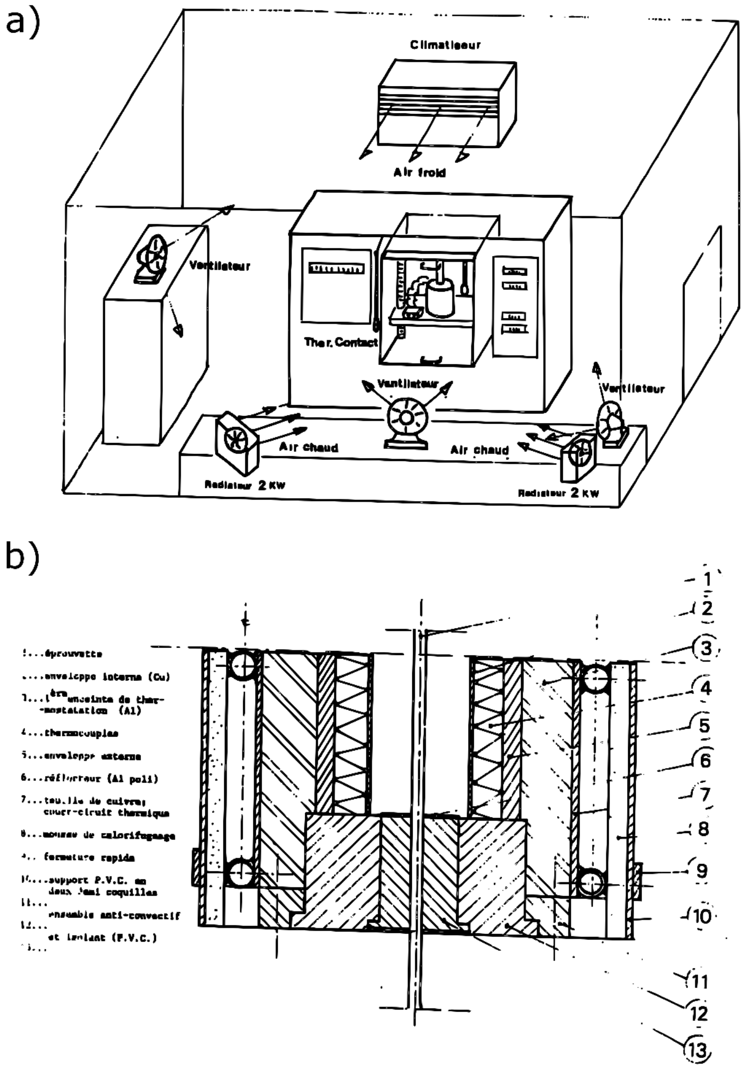

Figure 1-23: So-called micro-calorimeter: **a)** experimental room setup, **b)** details (image taken from [79]).

### 1.2.3.2 Infrared-based calorimetry

In the 70s, the development of IR imaging systems for temperature measurement became available, despite a high cost. The development of such systems was a great opportunity for material scientists and engineers. The first available system (called SPATE) was developed in the UK for the so-called *thermal stress analysis* (TSA): it was possible to capture the thermoelastic response (in practice the stress field) at the surface of metallic components [80,81]. The first application of IRT to characterize the dissipation of a material under mechanical loading is reported in Ref. [82]. In this study, it was proved the possibility of using IR imaging to characterize the thermal signature of a heterogeneous deformation process, as presented in the next paragraphs.

### Indirect evaluation of stored energy using IRT (Oliferuk's approach)

In the 80s, the first application of IRT to the assessment of heat due to mechanical loading was made in the work of Oliferuk et al. [83]. An innovative two-step method was proposed and successfully applied to stainless steel. First, the specimen is tested while thermal fields at the specimen surface are recorded. Second, a free-stress virgin specimen is heated using the Joule effect controlled with a PID loop aiming to follow the same temperature variation as the specimen under mechanical loading. Therefore, the heat released by the loaded specimen can be quantified from the input electrical power provided to the stress-free specimen. Thermal images at different times are presented in Figure 1-24. The temperature increases of 7 K at a deformation of 7.3% (from image (a) to image (d)) was recorded. This method is indirect. It deserves to be mentioned for its originality. Moreover, results were confirmed by direct methods (A comparative study will be presented in the next section). However, this method can only estimate the heat of homogeneous phenomenon: spatio-temporal thermal information cannot be estimated. Other indirect methods have been found in the literature: see for instance Refs [84–86].

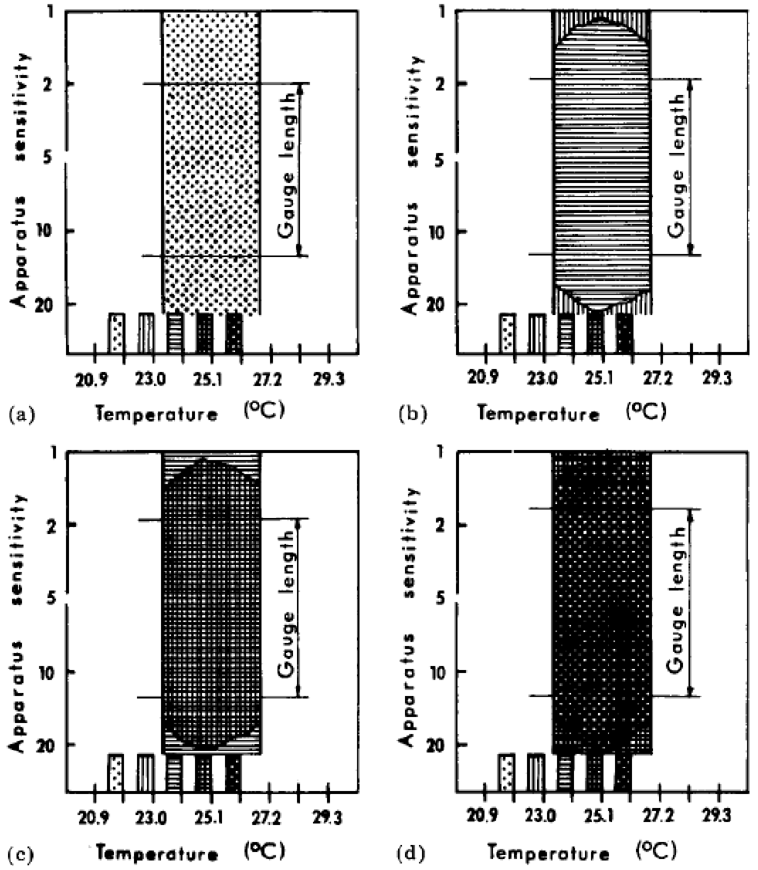

Figure 1-24: Temperature distribution on the surface of steel specimen: **a)** before elongation, **b)** after 19 s of elongation, **c)** after 30 s of elongation, and **d)** after 40 s of elongation (image taken from [83]).

### Direct method evaluation of stored energy using IRT (heat source reconstruction)

The last known method to our knowledge is called *heat source reconstruction* (HSR), also named heat source estimation or dissipation technique [69,87,88]. It is based on the heat diffusion equation [89]. In a single-step approach, the local heat power density is reconstructed directly from the temperature fields measured by an IR camera at the surface of the specimen under test. Calorimetric spatio-temporal information can be thus obtained [90–92].

Thanks to the improvement of the IRT, the new cameras are equipped with a matrix of more than 1 megapixel, and enable to obtain temperature fields with a low spatial resolution (up to a few µm) depending on the size of the field of view), a high acquisition frequency (up to 100 kHz) and a high measurement resolution (typically 20 mK after calibration for cold cameras) [93].

It is important to recall that temperature fields are captured at the surface of the material specimen during the mechanical test. As the heat diffusion equation is three-dimensional, it is mandatory to adapt it. This is possible for specific specimen geometries of the specimen. Three different approaches are proposed in the literature: one-dimensional (1D) version for elongated specimens, two-dimensional (2D) version for thin plane specimens, and zero-dimensional (0D) in the case of the homogeneous response of the specimen: see Ref. [91]. In the three cases, the heat exchange by convection with ambient air is taken into account in the formulation of the equation.

### 1.2.3.3 Comparison of the deformation calorimetry methods

We propose here a summary of two studies using the three different methods to metallic materials: micro-calorimetry, Oliferuk's approach, and heat source reconstruction (HSR).

**Validation of IRT for deformation calorimetry**

In Ref. [69], a comparison between micro-calorimetry (noted "µC.") and HSR (noted "I.R.") is presented. At first glance, Figure 1-25 depicts a good correlation between these two techniques. The results presented come from simultaneous measurements performed on the same specimen: one part of the specimen was analyzed by IR thermography and the second part by micro-calorimeter. We note a dispersion of the heat estimated by micro-calorimeter on four specimens. IR measurements on two specimens gave very similar results. Results can vary as can be also observed in the tests reported in other papers from Chrysochoos (see Refs [69,88,94]), but these experiments confirmed the relevancy of IRT for deformation calorimetry. To our best knowledge, to date, no similar comparative studies have been carried out. It is worth noting that, in the absence of phase transition such as in SMAs, the heat can never be of a higher intensity than that the work: the ratio between plastic-origin heat and plastic work can never be greater than 1.

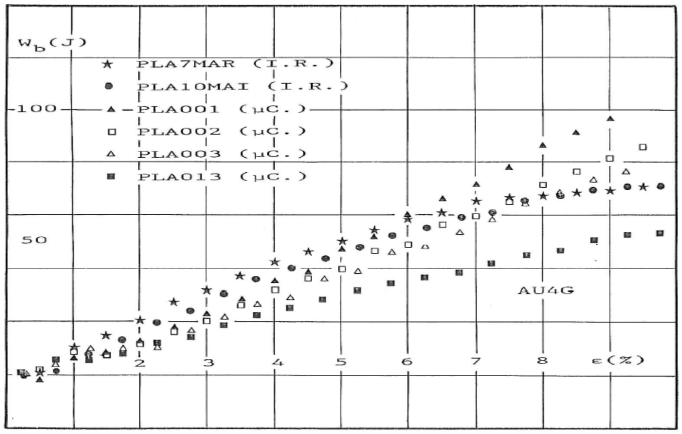

Figure 1-25 Comparison between results by micro-calorimetry and HSR for an AU4G aluminum alloy (image taken from [69]).

### Comparison of stored energy evolutions

Two studies were selected to compare measurements of the evolution of the stored energy during the deformation of two metals: an aluminum alloy in Ref. [69] using HSR, and stainless steel in Ref. [83] using Oliferuk's approach. In Figure 1-26, it can be seen that a maximum of the ratio of stored energy $E_S$ over work $W$ is reached shortly after the onset of plasticity for both materials (at about 0.8% of deformation). Then, the energy storage decreases as the material continues to be deformed. The energy storage process is directly related to the microstructural modifications (mainly growth of the dislocation network [72,83]). As the material approaches fracture, it stores less and less energy as voids grow, and grain boundaries dislocate.

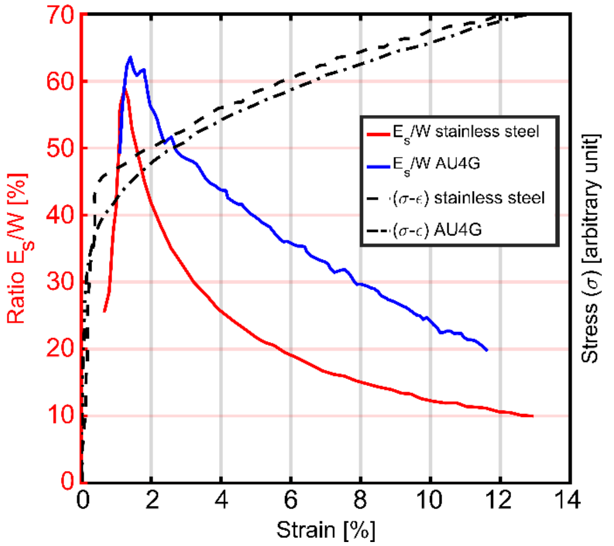

Figure 1-26: Comparison of the ratio of stored energy $E_S$ over work $W$ as a function of strain for an aluminum alloy (blue curve) and stainless steel (red curve). Corresponding normalized stress-strain curves are also displayed (black curves). Data for stainless steel were taken from Ref. [83], and for aluminum alloy (AU4G) from Ref. [69].

In conclusion, the different non-contact methods showed similar results in terms of released heat accompanying plastic deformation processes. Note that the micro-calorimetric method requires metrological considerations for its implementation, but no further modifications are needed. The two-step method proposed by Oliferuk requires the estimation of the electrical power applied to the dummy specimen. Only the HSR approach can be used for the assessment of heterogeneous heat power density fields, as the other two methods only allow us to estimate the total amount of heat (over the whole specimen). In the following section, some applications of HSR to NiTi SMA are presented.

## 1.2.4 Deformation calorimetry applied to SMAs

There is an extensive collection of papers on the thermal response of NiTi based on contact measurement [23,95–97] and IR thermography [44,98–104]. However, deformation calorimetry is far from being a commonly applied technique. HSR in the case of homogeneous heat response (called the 0D approach) has been applied for the characterization in tension and compression [43,44,105]. The measurement of heterogeneous heat fields in 1D [43,106,107] and 2D [100,106] has been applied to NiTi plates and tubes tested in tension. **It is worth noting that the 1D HSR approach has never been applied to NiTi wires it is seemingly a very appropriate method.** Note finally that the 1D approach was used for a comparative study with DSC measurement to characterize TIMT, i.e. without mechanical loading [68,108–110].

In contrast to conventional metallic materials which exhibit thermoelastic couplings, SMAs are accompanied by another reversible heat, namely the latent heat associated with MT. Therefore, evaluating the stored energy at any given time of a test is not a simple procedure and requires additional assumptions. For this purpose, models based on the thermodynamics of involved deformation processes have been developed in the literature to separate the different sources of heat involved in the deformation process [23,44].

### 1.2.4.1 The 1D approach applied to NiTi plate

Figure 1-27 shows the deformation and temperature fields on a NiTi plate subjected to uniaxial tension from Refs [106,107]. Strain field measurements were performed by DIC on one side of the specimen. Temperature fields were obtained by IRT on the other side. 1D heat source profiles (heat power density, in W/m$^3$) and corresponding heat profiles (in J.m$^{-3}$) were then reconstructed: see Section 4 about the details on HSR processing. In order to improve the resolution of the measurements, let us note that the strain and temperature maps were averaged in the direction transverse to the mechanical load, leading to 1D space-time color maps. It should be noted that Ref. [107] is the first one presenting a heterogeneous heat field (in J/m$^3$) accompanying deformation process in NiTi, i.e. the time integration of heat sources (in W.m$^{-3}$) over the test duration.

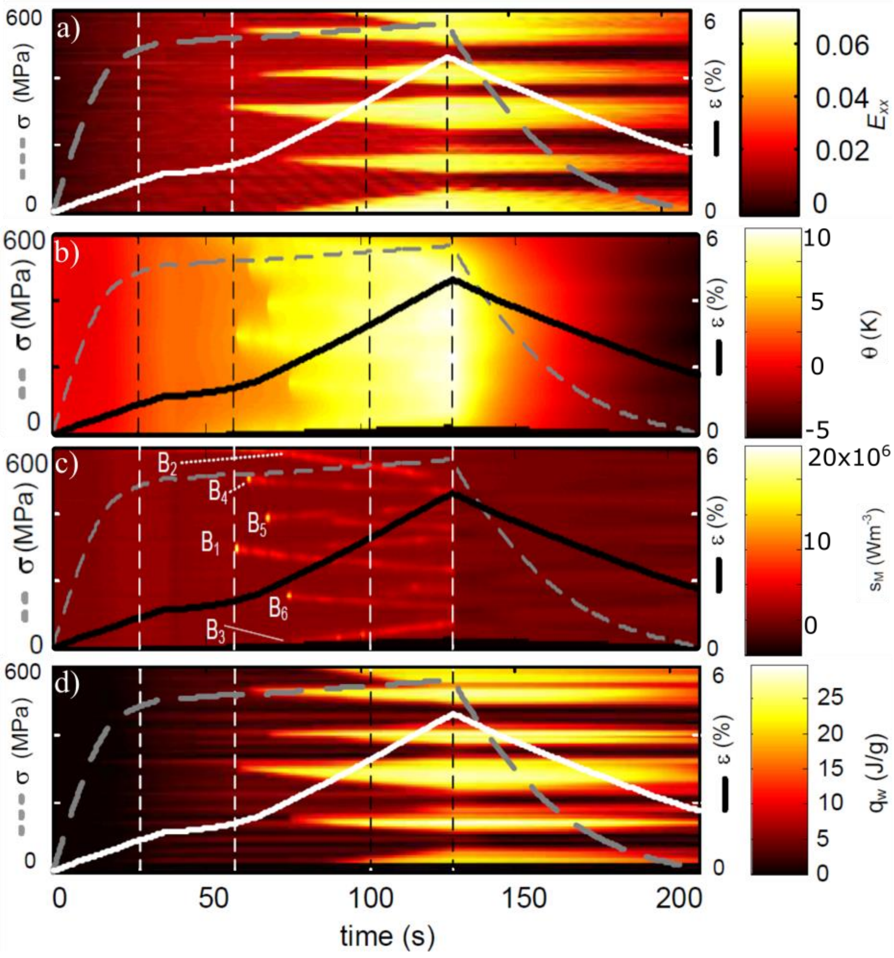

Figure 1-27: Thermomechanical 1D response of a NiTi plate in tension, a) strain field, b) temperature change field, c) heat source field, d) specific heat field (adapted from [107]).

The NiTi plate was stretched up to 4.5% (macroscopic deformation) and then unloaded. Figure 1-27-a-b shows the deformation and temperature fields respectively. In the deformation field (Figure 1-27-a), it can be seen that the specimen has been partially transformed. At the maximum stretch level, strain heterogeneity is evidenced. Some parts of the specimen have deformations of around 1% (red color) while others are at about 7% (white-yellow color). The advantage of reconstructing the heat sources is demonstrated in this study: the temperature field alone does not allow estimating the proportion of the specimen transformed because of the heat conduction (Figure 1-27-b). The fields of the heat source (Figure 1-27-c) and specific heat (Figure 1-27-d) allow us to clearly identify the areas where the material has transformed. HSR allows seeing the calorific response of the material getting rid of the heat transfer effects. The nucleation sites of MT can be clearly seen (see points B in Figure 1-27-c), as well as the propagation fronts (lines following the nucleation points). In Figure 1-27-d, the specific heat field is obtained using time integration by the trapezoidal method. It can be noted that the energy field is very similar to the deformation one. Finally, the measured specific heat is of the same order as the specific heat values reported for NiTi MT in the literature, typically between 10 $J.g^{-1}$ and 30 $J.g^{-1}$ [41,100,115].

As a general remark, let us recall that heat sources are heat *power* (in $W.m^{-3}$), so they enable us to track the kinetics of the phenomena involved [111].

### 1.2.4.2 The 0D approach applied to a NiTi wire

In Ref. [44], HSR and DIC were applied to characterize a NiTi wire that was preliminary heat-treated at low temperature (< 525 K). The specimen deformed homogeneously, so the 0D approach could be applied. Figure 1-28 shows the thermal and mechanical power densities during a SE cycle. The data acquired during the test are shown in Figure 1-28-a: macroscopic strain, strain rate, as well as *averaged* temperature change. Figure 1-28-b shows the mechanical power and the thermal power (i.e. the heat source) during the loading and unloading stages as a function of the macroscopic strain. The thermal power is about twice the mechanical power when the phase transformation occurs due to the phase transformation latent heat.

The main result of this study is the determination of the latent heat. Indeed, in some NiTi like the one characterized here, there are no peaks of transformation observable in the calorimetric data classically obtained by DSC, making it impossible to measure transformation latent heat. The authors have thus applied HSR and used a model based on the thermodynamic function of the Gibbs free potential to extract the enthalpy difference for both the direct and inverse transformations. Contrary to classical DSC data, heat could be clearly identified during the transformation. Besides, values found were very close to those known for other NiTi alloys: 19.6 $J.g^{-1}$ for the forward transformation and 14.6 $J.g^{-1}$ for the reverse transformation. This study proved that HSR is a complementary method to conventional DSC.

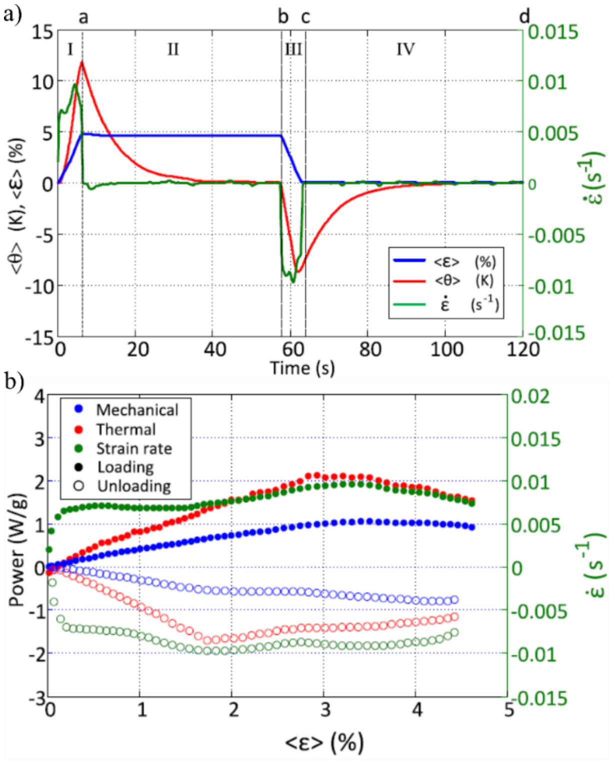

Figure 1-28: Homogeneous response of a SE NiTi wire during a load-unload cycle in tension: a) strain, temperature change and strain rate variations, b) mechanical power, heat source and strain rate as a function of macroscopic strain (image adapted from [44]).

# 1.3 Thermodynamical formalism

## 1.3.1 Introduction

The keystone of the present research work is the implementation of HSR (heat source reconstruction) to characterize superelastic NiTi wires. In the previous sections, we have presented the fundamental principles of NiTi followed by state of the art on deformation calorimetry, including some HSR results. Before presenting details about HSR in Section 4, the present section is devoted to the presentation of the theory related to the thermomechanical characterization of materials. It is a review of various papers: Refs [69,90,112–115].

### 1.3.1.1 Concept of a thermodynamical system

Classical thermodynamics studies the exchange of matter and energy that occurs between a body and its environment. A body is a material system of known size with a real or fictitious surface containing the studied matter. A large quantity of subsystems defines it. The environment is everything that does not belong to the system. In the context of the present research work, we are discussing here only *closed* systems, i.e., when the material is in solid form with no material exchange with the environment (only energy exchange). Within the framework of the study of solids, we consider that the preponderant source of energy that is exchanged between a system and its environment is of thermal origin, so we will only consider heat exchanges (no magnetic or chemical interactions).

In order to make a quantitative description of the state of a system (Figure 1-29), it is necessary to define a reasonable amount of independent physical variables. Intensive variables have values that do not depend on the amount of material. Extensive variables are proportional to the amount of material making up the system concerned.

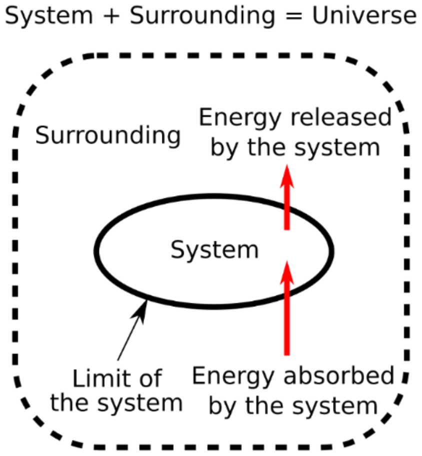

Figure 1-29: Schematic of a thermodynamical system.

### 1.3.1.2 Energy balance of a mechanical test

**Hypotheses**

Within the framework of the thermomechanics of materials, a solid system that undergoes a deformation is considered an out-of-equilibrium thermodynamic system. It is the site of an irreversible process. We have defined in the previous section that our system is considered closed. Thus, only energetic exchanges take place. It is assumed that at any moment, any out-of-equilibrium thermodynamic system can be considered as a succession of homogeneous thermodynamic subsystems in a state of equilibrium. And therefore, the time of return to equilibrium of each subsystem is infinitely smaller than the time of the return to equilibrium to the global system.

**Different cases of energy balance**

Figure 1-30 shows different thermodynamic paths in the form of stress-strain-internal variable diagram $(\sigma - \epsilon - \alpha)$ that can be encountered during thermomechanical testing as presented in Ref. [115]. Symbol $\alpha$ corresponds to the set of internal variables of the material. We consider mechanical load-unload cycles $(\sigma_A = \sigma_B)$, beginning in a state $A = (T_A, \epsilon_A, \alpha_A)$ and ending in a state $B = (T_B, \epsilon_B, \alpha_B)$. Three different thermodynamic paths can be identified:

- The first case (Figure 1-30-i) corresponds to a specimen undergoing deformation for which an irreversible mechanical process occurs (for example a plastic process: $\epsilon_A \neq \epsilon_B$). The curve in the $\sigma - \epsilon - \alpha$ space is not a closed loop: $A \neq B$. The material state has been irreversibly changed: $\epsilon_A \neq \epsilon_B$ and $\alpha_A \neq \alpha_B$.
- In the second case (Figure 1-30-ii), the deformation of the system leads to a closed curve in the $\sigma - \epsilon$ diagram. No residual deformation is observed but the internal variables $(\epsilon_A = \epsilon_B)$. But the temperatures and/or the internal variables in A and B are not the same: so $A \neq B$. This test is named mechanical cycle.

- In the last case (Figure 1-30-iii), the curve in the $\sigma - \epsilon - \alpha$ space is a closed loop. The cycle is perfectly reversible. This type of cycle is referred to as *isentropic* and we will name it *thermodynamic cycle* because it is fully reversible: $A = B$.

The diagrams presented clearly show that the evaluation of mechanical dissipation cannot be made on the basis of mechanical quantities $(\sigma - \epsilon)$ alone. The establishment of an energy balance is essential to estimate mechanical dissipation. In the following section, the mathematical framework of thermodynamics of irreversible processes (TPI) is developed.

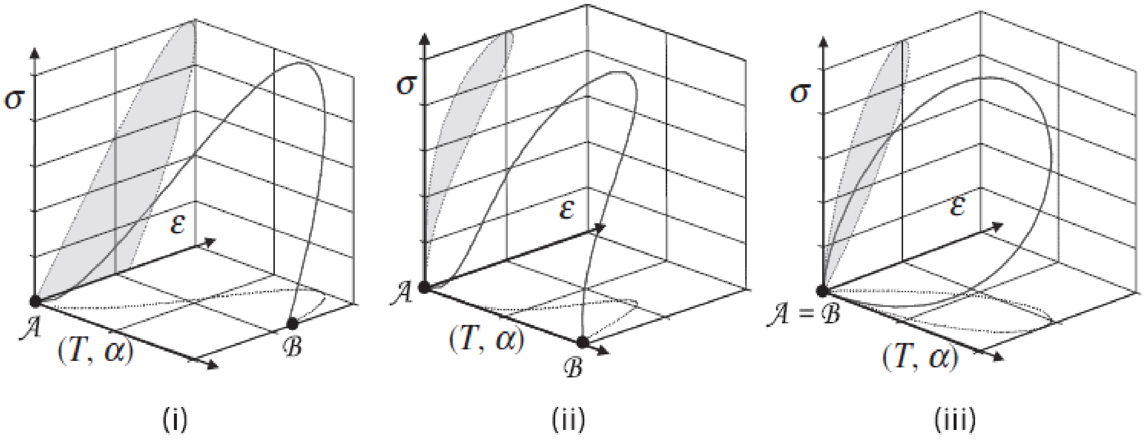

Figure 1-30: Thermodynamical paths in stress-strain-internal variable $(\boldsymbol{\sigma} - \boldsymbol{\epsilon} - \boldsymbol{\alpha})$ space (image taken from [115]).

### 1.3.2 The first principle of thermodynamics

The first principle of thermodynamics states that for a closed system, the sum of the energies exchanged between the system and its environment is equal to zero. The mathematical form of the first principle is as follows:

$$W + Q = 0 \tag{1-7}$$

The term $W$ represents the work and $Q$ represents the heat. The work can be decomposed into 2 terms:

$$W = W_M + W_U \tag{1-8}$$

where $W_M$ represents the work due to mechanical forces and $W_U$ is the work of other physical origin (electric, magnetic, nuclear and others). The mechanical work $W_M$ is the addition of the atmospheric pressure effect $(W_A)$ and the external force effect $(W_E)$. However, in the framework of the mechanics of materials, atmospheric and other physical energy work contributions can be neglected. Thus, only the forces from the mechanical origin are considered.

$$W = W_M + W_U = W_E + W_A + W_U \cong W_M \tag{1-9}$$

The total energy $E$ of a system is the sum of the internal energy $U$ and kinetic energy $K$:

$$E = U + K \tag{1-10}$$

The kinetic energy is defined by:

$$K = \frac{1}{2}\int_{\Omega} \rho\vec{v}.\vec{v}\, dV \tag{1-11}$$

where $\rho$ is the density and $\vec{v}$ is the material point velocity.

The kinetic energy theorem states that the variation of kinetic energy is equal to the sum of the working forces (internal and external) that are applied to the system under consideration:

$$\dot{K} = \dot{W}_{\text{ext}} + \dot{W}_{\text{int}} \tag{1-12}$$

The internal energy of a system having a volume Ω is defined by:

$$U = \int_{\Omega} \rho u\, dV \tag{1-13}$$

where $u$ is the specific internal energy of the material point. The internal energy is the thermodynamic function directly associated with the first principle.

One of the consequences of the first principle is that the rate of change over time of the total energy of a continuous body is the sum of the rate of external mechanical work plus the heat rate changes:

$$\dot{U} = \dot{W}_{\text{ext}} + \dot{Q} \tag{1-14}$$

where the terms $\dot{U}, \dot{W}_{\text{ext}}$ and $\dot{Q}$ represent respectively the rate of internal energy, the external work and the heat power changes. The latter is the sum of the external volume heat source $r$ and the heat flux passing through the boundaries of the system:

$$\dot{Q} = \int_{\Omega} r\, dV - \int_{d\Omega} \vec{q}.\vec{n}\, dS \tag{1-15}$$

the heat flux $\vec{q}$ is defined by the Fourier law:

$$\vec{q} = -k\,\overrightarrow{\text{grad}}\,T \tag{1-16}$$

So,

$$\dot{W}_{\text{ext}} = \int_{d\Omega} \vec{T}.\vec{n}\, dS + \int_{\Omega} \vec{f} dV = \int_{\Omega} \sigma\, \dot{\epsilon}\, dV = -\dot{W}_{\text{int}} \tag{1-17}$$

where the term $\vec{T} = \sigma\vec{n}$ is the surface traction vector (dot product of the stress $\sigma$ to the unit vector $\vec{n}$) and the term $\vec{f}$ the body force vector (which is generally neglected).

To describe the state of a continuous medium, the local form of the first principle of thermodynamics is thus defined by:

$$\dot{U} = -\dot{W}_{\text{int}} + \dot{Q} \tag{1-18}$$

$$\frac{d\left(\int_{\Omega} \rho u dV\right)}{dt} = \int_{\Omega} \sigma\dot{\epsilon}\, dV + \int_{\Omega} r\, dV - \int_{d\Omega} \vec{q}.\vec{n}\, dS \tag{1-19}$$

Using the divergence theorem, the local form of the first principle of thermodynamics is thus:

$$\rho\dot{u} = \sigma\dot{\epsilon} + r - div\, \vec{q} \tag{1-20}$$

### 1.3.3 The second principle of thermodynamics

Irreversible processes are not taken into account by the first principle of thermodynamics. From the first works by Sadi Carnot, then by Rudolf Clausius, the need to establish a second principle (also called the principle of evolution) leads to the definition of entropy (meaning change of direction in Greek). The general definition of entropy states that an exchange of energy between a system and its environment is equal to the scalar product of an intensive variable and an extensive variable: the extensive physical quantity is $S$ (the entropy of the system) and is defined by the following relation:

$$\dot{Q} = T\,\dot{S} \quad \text{where } \dot{S} = \dot{S}_{\text{exchanged}} + \dot{S}_{\text{produced}} \quad \text{with } \dot{S}_{\text{produced}} \geq 0 \tag{1-21}$$

In the framework of a closed system, the entropy rate for an elementary transformation using the equations 1-15 and 1-21 is expressed as:

$$\dot{S} \geq \int_{\Omega} \frac{r}{T} dV - \int_{d\Omega} \frac{\vec{q}.\vec{n}}{T} dS \tag{1-22}$$

That means that the production of entropy throughout a thermodynamical cycle is equal to or higher than the volume of external heat sources plus the heat sources going through the surface of the considered system. The specific entropy $s$ is defined by:

$$S = \int_{\Omega} \rho s \, dV \tag{1-23}$$

Using the inequality defining entropy production and the divergence theorem, we obtain the local form of the second principle of thermodynamics.

$$\rho \dot{s} - \frac{r}{T} + \frac{\operatorname{div} \vec{q}}{T} \geq 0 \tag{1-24}$$

### 1.3.4 Clausius-Duhem inequality

To establish the energy balance and the expression of dissipation, we have to combine the first and second principles of thermodynamics. Let us recall the local form of the first principle:

$$\rho \dot{u} = \sigma \dot{\epsilon} + r - div \, \vec{q} \tag{1-25}$$

$$\rho \dot{u} - \sigma \dot{\epsilon} - r + div \, \vec{q} = 0 \tag{1-26}$$

and of the local form of the second principle:

$$\rho \dot{s} - \frac{r}{T} + \operatorname{div}\left(\frac{\vec{q}}{T}\right) \geq 0 \tag{1-27}$$

Subtracting the second principle (eq. 1-27) to the first one (eq. 1-26), we obtain the general form of the Clausius-Duhem inequality:

$$\rho(T\dot{s} - \dot{u}) + \sigma \dot{\epsilon} - \frac{\vec{q}}{T} \, \overrightarrow{\operatorname{grad}} \, T \geq 0 \tag{1-28}$$

In order to describe the evolution of a closed system, it is possible to use free energy potentials. We will then use Helmholtz's free energy potential, whose definition is as follows:

$$\phi = u - Ts \tag{1-29}$$

We then differentiate in the time:

$$\dot{u} = \dot{\phi} + \dot{T}s + T\dot{s} \tag{1-30}$$

The new form of the Clausius-Duhem inequality (also called the dissipation inequality) is:

$$\sigma\dot{\epsilon}-\rho\big(\dot{\phi}+\dot{T}s\big)-\frac{\vec{q}.\overrightarrow{\mathrm{grad}}\,T}{T}\geq 0 \qquad \text{1-31}$$

### 1.3.5 Mechanical and thermal dissipations

The state variables describe thermodynamical sub-systems in an equilibrium state. Two kinds of variables exist: the internal variables and the observable ones. The internal energy is defined by the entropy ($s$), strain ($\epsilon$), and internal variable ($\alpha_i$):

$$u=u(s,\epsilon,\alpha_i) \qquad \text{1-32}$$

Thus, the Helmholtz free energy $\phi$ (which is the Legendre transforms of internal energy) is:

$$\phi=\phi(T,\epsilon,\alpha_i) \qquad \text{1-33}$$

where $i=1,\dots n$. Note that $\alpha_1$ is considered to be the strain. The state laws are defined by the state variables. They summarize the properties of state equilibrium to the conjugated state variables:

$$\begin{cases} s=-\dfrac{\partial\phi}{\partial T} \\ \sigma^{\mathrm{rev}}=\rho\dfrac{\partial\phi}{\partial\epsilon} \\ A_j=\rho\dfrac{\partial\phi}{\partial\alpha_j} \quad \text{for } j=2,\dots n \end{cases} \qquad \text{1-34}$$

where $\sigma^{\mathrm{rev}}$ is the reversible stress and $A_i$ the complementary thermodynamical forces. The derivative of the Helmholtz potential writes:

$$\dot{\phi}=\frac{\partial\phi}{\partial T}\dot{T}+\frac{\partial\phi}{\partial\epsilon}\dot{\epsilon}+\frac{\partial\phi}{\partial\alpha_j}\dot{\alpha}_j \qquad \text{1-35}$$

And the Clausius-Duhem inequality becomes:

$$\sigma^{\mathrm{irr}}\dot{\epsilon}-A_j\dot{\alpha}_j-\frac{\vec{q}.\overrightarrow{\mathrm{grad}}\,T}{T}\geq 0 \qquad \text{1-36}$$

where $\sigma^{\mathrm{irr}}$ is the irreversible part of the stress. The dissipation can be separated in two main terms: the intrinsic mechanical dissipation:

$$d_1 = \sigma^{\mathrm{irr}}\dot{\epsilon} - A_j\dot{\alpha}_j \ \geq 0 \tag{1-37}$$

and the thermal dissipation:

$$d_2 = -\frac{\vec{q}.\overrightarrow{\mathrm{grad}}\,T}{T} \geq 0 \tag{1-38}$$

From a mechanical standpoint, the second principle shows the weight of the different sources of irreversibility. If the evolution of a thermodynamic system is said to be reversible, thus:

$$d_1 = \ d_2 = 0 \tag{1-39}$$

### 1.3.6 The general form of the heat equation

The heat equation can be deduced from the first principle and from the decomposition of the expression of the specific internal energy derivative:

$$\dot{u} = \dot{\phi} + \dot{T}s + T\dot{s} \tag{1-40}$$

$$\rho\dot{u} = \sigma\dot{\epsilon} + r - \mathrm{div}\,\vec{q} \tag{1-41}$$

The derivations of the Helmholtz free potential ($\dot{\phi}$), the specific entropy ($s$) and its time derivation ($\dot{s}$) write:

$$\dot{\phi} = \frac{\partial\phi}{\partial T}\dot{T} + \frac{\partial\phi}{\partial\epsilon}\dot{\epsilon} + \frac{\partial\phi}{\partial\alpha_j}\dot{\alpha}_j \tag{1-42}$$

$$s = \frac{-\partial\phi}{\partial T} \tag{1-43}$$

$$\dot{s} = -\left(\frac{\partial^2\phi}{\partial T^2}\dot{T} + \frac{\partial^2\phi}{\partial T\partial\epsilon}\dot{\epsilon} + \frac{\partial^2\phi}{\partial T\partial\alpha_j}\dot{\alpha}_j\right) \tag{1-44}$$

Therefore, the evolution of the specific internal energy is expressed by:

$$\dot{u} = \frac{\partial\phi}{\partial\epsilon}\dot{\epsilon} + \frac{\partial\phi}{\partial\alpha_j}\dot{\alpha}_j - T\left(\frac{\partial^2\phi}{\partial T^2}\dot{T} + \frac{\partial^2\phi}{\partial T\partial\epsilon}\dot{\epsilon} + \frac{\partial^2\phi}{\partial T\partial\alpha_j}\dot{\alpha}_j\right) \tag{1-45}$$

The expression of the heat capacity at constant strain $\epsilon$ and internal variable $\alpha_j$ is defined by:

$$C_{\epsilon,\alpha_j} = -T\frac{\partial^2\phi}{\partial T^2} \tag{1-46}$$

The first principle becomes:

$$\rho\left[\frac{\partial\phi}{\partial\epsilon}\dot{\epsilon} + \frac{\partial\phi}{\partial\alpha_j}\dot{\alpha}_j - T\left(\frac{\partial^2\phi}{\partial T^2}\dot{T} + \frac{\partial^2\phi}{\partial T\partial\epsilon}\dot{\epsilon} + \frac{\partial^2\phi}{\partial T\partial\alpha_j}\dot{\alpha}_j\right)\right] = \sigma\dot{\epsilon} + r - div\vec{q} \tag{1-47}$$

An extended expression of the heat equation with thermomechanical coupling is thus obtained:

$$\rho C_{\epsilon,\alpha_j}\dot{T} = \sigma\dot{\epsilon} + r - div\vec{q} - \rho\left(\frac{\partial\phi}{\partial\epsilon}\dot{\epsilon} + \frac{\partial\phi}{\partial\alpha_j}\dot{\alpha}_j\right) + \rho T\left(\frac{\partial^2\phi}{\partial T\partial\epsilon}\dot{\epsilon} + \frac{\partial^2\phi}{\partial T\partial\alpha_j}\dot{\alpha}_j\right) \tag{1-48}$$

The above expression is the starting point that will provide us the framework for the reconstruction of the heat sources from the knowledge of the temperature measured by an IR camera at the surface of a material specimen. Some comments can be done about the different terms of the expression:

- The left-hand side of the equation is called heat storage and is defined by $s_{\mathrm{HS}} = \rho C\,\dot{T}$. When the observed medium undergoes locally large displacements, it is necessary to use the particular derivative as follows: $s_{\mathrm{HS}} = \partial T/\partial t + \vec{v}.\overrightarrow{\mathrm{grad}}T$ where $\vec{v}$ is the velocity of the material point. The use of a full-field measurement technique for the displacements is therefore necessary.
- The expression of the intrinsic dissipation (also called mechanical dissipation) is: $d_1 = \sigma\,\dot{\epsilon} - \rho\left(\frac{\partial\phi}{\partial\epsilon}\dot{\epsilon} + \frac{\partial\phi}{\partial\alpha_j}\dot{\alpha}_j\right)$.
- The thermomechanical couplings term is defined by the following expression: $s_{\mathrm{TMC}} = \rho T\left(\frac{\partial^2\phi}{\partial T\partial\epsilon}\dot{\epsilon} + \frac{\partial^2\phi}{\partial T\partial\alpha_j}\dot{\alpha}_j\right)$. It is worth to be mentioned that the first term corresponds to the thermo-elastic coupling.

So, equation 1-48 becomes:

$$\rho C_{\epsilon,\alpha_j}\dot{T} = d_1 + r - \mathrm{div}\,\vec{q} + s_{\mathrm{TMC}} \tag{1-49}$$

In the following, the thermomechanical couplings term ($s_{\mathrm{TMC}}$) and the mechanical dissipation ($d_1$) will be represented by the term $s_{\mathrm{int}}$:

$$s_{\mathrm{int}} = d_1 + s_{\mathrm{TMC}} \tag{1-50}$$

The final general form of the heat equation thus writes:

$$\rho C_{\epsilon,\alpha_j}\dot{T} + \mathrm{div}\,\vec{q} = s_{\mathrm{int}} + r \tag{1-51}$$

However, the general form of this equation cannot be used. Indeed, the temperature fields are acquired in 2D at the surface of the material specimen under study (acquisition of thermal "images"). It will therefore be necessary to adapt equation 1-51 according to the geometry of the material specimen.

# 1.4 Fundamentals of HSR

In the present work, we focus on the characterization of NiTi SMA wires. The general form of equation 1-51 cannot be used as-is. Indeed, an IR camera embeds a plane matrix of detectors which only allows the acquisition of a 2D thermal field at the surface of the material specimen. In the present research work, we have performed tensile tests on wires, so a one-dimensional (1D) approach is possible. The approach was introduced in Ref. [116], and was applied to cylindrical specimens [100,114,117–119] and flat specimens [91,106,113,120–124]. The next section 1.4.1 recalls the two types of heat equation that will be used in the present research work, namely a 1D version and a so-called 0D version which is useful for specific cases. Then, Section 1.4.2 will present an overview of the HSR processing, focusing on a 1D example by H. Louche [120].

## 1.4.1 Several versions of the heat equation

Before presenting a simplified version (1D) of the thermal equation in the gauge length of wires, we recall the assumptions that have been adopted during our tests presented in the next chapters.

### 1.4.1.1 Hypotheses

Four hypotheses are introduced:

**1-** The conduction of heat follows a linear law. The material is assumed to be isotropic and is defined by Fourier's law:

$$\vec{q} = -k\,\overrightarrow{\text{grad}}\,T \qquad 1\text{-}52$$

where $k$ is the thermal conductivity of the material. As a consequence, the divergence operation div $\vec{q}$ can be replaced by a Laplacian operator.

**2-** The specific heat is assumed to be constant:

$$C_{\epsilon,\alpha_j} = C \qquad 1\text{-}53$$

**3-** The convective term from the particular derivative of the heat storage term is overlooked.

$$\frac{dT}{dt} = \frac{\partial T}{\partial t} + \vec{v}.\overrightarrow{\text{grad}}T \simeq \frac{\partial T}{\partial t} \qquad 1\text{-}54$$

**4-** The temperature is considered nearly homogeneous in the cross-section of the wire. Actually, IRT data are acquired at the surface of the wire:

$$T_{\text{measured}}(\Theta,z,t)=T(R,\Theta,z,t) \qquad 1\text{-}55$$

where $R$ is the radius of the wire. We assume:

$$T(r,\Theta,z,t)\approx T_{\text{measured}}(\Theta,z,t) \qquad 1\text{-}56$$

Figure 1-31 below shows a NiTi wire installed in the jaws of a tensile machine. The wire is discretized in its axial direction, corresponding to the pixels of the field of view of the IR camera. The different types of heat exchange of a wire slice (illustrated by the $i^{th}$ element in Figure 1-31) are: conduction in the axis of the wire, convection with ambient air, radiation with the environment. Note that $T_{\text{measured}}\approx T$ does not mean that there is no convection.

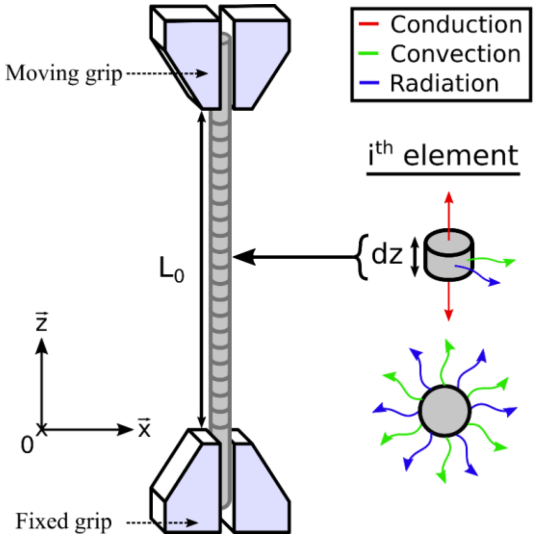

Figure 1-31: Schematic view of a wire clamped in the jaws of a testing machine.

Taking into account the last hypothesis, we can average the measured temperature data in the transverse direction. However, several precautions must be taken in order to perform an IR measurement: the emissivity of the specimen surface must be known. For this purpose, a high thermal emissivity coating is classically applied on the surface of metallic specimens. However, when the surface of the body to be observed is curved, the relative emissivity varies as a function of the angle around the axis of view of the camera. This relative emissivity has been measured for different materials as shown in Figure 1-32 [125]. It can be observed that, for the materials considered in this study, the emissivity is relatively constant for an angle between $\pm 40°$. Considering that thermal images consist of 2D matrices whose components $(x,z)$ are defined in the specimen plan perpendicular to the camera axis, the expression of the 1D temperature profiles can be obtained by the following averaging operation:

$$T(z,t)=\frac{1}{n_x}\sum_{x=-R/2}^{x=+R/2}T(x,z,t) \qquad 1\text{-}57$$

where $n_x$ is the number of pixels in the transverse direction.

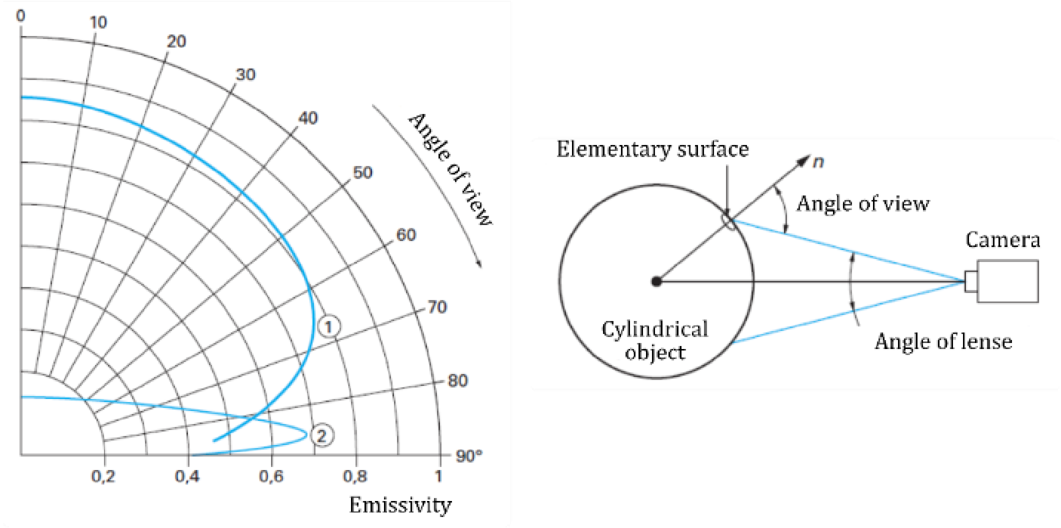

Figure 1-32: Observation angle and directional emissivity of rubber at 80°C (1) and a stainless steel 304 (2) (adapted from [125]).

### 1.4.1.2 Boundary conditions

On the surface of a wire ($r = R$), heat exchanges are made by convection of ambient air:

$$\phi_{\text{cond}} = \phi_{\text{conv}} \text{ ,so} - k\,S\left[\frac{\partial T}{\partial r}\right]_{r=R} = h\,P\,(T_{r=R} - T_\infty) + \epsilon\,\sigma\,\left({T_{r=R}}^4 - T_\infty^4\right) \tag{1-58}$$

where $\phi_{\text{cond}}$ and $\phi_{\text{conv}}$ are the conduction flux in the radial direction of the wire and in the surrounding par convection respectively. $S$ and $P$ are the area and the perimeter of the cylinder cross-section respectively. $h$ is the heat convection coefficient. $T_\infty$ is the temperature of the surrounding air. Let us recall that $\epsilon$ and $\sigma$ are the thermal emissivity of the surface and the Stefan-Boltzmann constant, respectively.

### 1.4.1.3 1D version of the heat equation

In the case of elongated specimens, the conduction term of the heat diffusion equation can be reduced to its 1D form:

$$-k\Delta T = -k\frac{d^2T}{dz^2} + \frac{2}{R}[h(T - T_\infty) + \epsilon\sigma(T^4 - T_\infty^4)] \tag{1-59}$$

where $T(z,t)$ is in practice the temperature measured at the specimen surface. It can be noted that the term $2/R$ is the simplification of the perimeter over the area. Assuming that temperature variations are lower than a few tens of degrees, the term related to radiation can be linearized:

$$T^4 - T_\infty^4 = (T_\infty + \theta)^4 - T_\infty^4 \simeq T_\infty^4 + 4T_\infty^3\theta \qquad \text{1-60}$$

where $\theta = T - T_\infty$ is the temperature variation with respect to the air temperature. The heat equation in 1D can be then written:

$$\rho C \frac{\partial T}{\partial t} - k \frac{d^2T}{dz^2} + \frac{2}{R}[h\theta + \epsilon\sigma(T_\infty^4 + 4T_\infty^3\theta)] = s_{\text{int}} + r \qquad \text{1-61}$$

In the HSR method, it is preferable to express the heat equation as a function of the temperature variation $\theta$.

$$\rho C \frac{\partial T_0}{\partial t} - k \frac{d^2T_0}{dz^2} + \frac{2}{R}\epsilon\,\sigma\,T_\infty^4 = r \qquad \text{1-62}$$

where $T_0$ is the field of temperature just before starting the mechanical test (in practice in a steady state regime). So, when considering that $T_\infty \approx T_0$, it comes

$$\rho C \frac{\partial \theta}{\partial t} - k \frac{d^2\theta}{dz^2} + \frac{2(h + 4T_\infty^3\epsilon\sigma)}{R}\theta = s_{\text{int}} \qquad \text{1-63}$$

A further modification can be made by dividing the heat equation by $\rho C$. It comes:

$$\frac{\partial \theta}{\partial t} - \frac{k}{\rho C}\frac{d^2\theta}{dz^2} + \frac{\theta}{\tau_{1\text{D}}} = \frac{s_{\text{int}}}{\rho C} \qquad \text{1-64}$$

$\tau_{1\text{D}}$ is a characteristic time of the heat exchanges between the wire and the ambient air (more precisely the heat exchanges with the environment except by contact with the jaws of the testing machine). It can be expressed by $\frac{\rho CR}{2(h+4T_\infty^3\epsilon\sigma)}$. In practice, it can be simply identified by considering a natural cooling after preliminary homogeneous heating of the specimen “suspended in the air” (i.e., without contact with the jaws of the testing machine). Indeed, the solution of Eq. 1-64 with $s_{\text{int}} = 0$ and $d^2\theta/dz^2 = 0$ is an exponential decay:

$$\theta_{\text{cooling}}(t) = \theta_0 \exp\left[\frac{-(t - t_0)}{\tau_{1\text{D}}}\right] \qquad \text{1-65}$$

where $\theta_0$ is the temperature change at the time $t_0$ during the natural cooling. Natural return to equilibrium can be considered as reached in about 4 or 5 times $\tau_{1\text{D}}$. The value of $\tau_{1D}$ depends on the potential air flow around the specimen and potentially to the value of $\theta$. It is generally considered as a constant in most of the experiments for temperature changes of a few degrees.

Note finally that the “heat source” term $s_{\mathrm{int}}/\rho C$ is expressed in K.s$^{-1}$. It corresponds to the temperature rate associated with heat production/absorption in adiabatic conditions.

### 1.4.1.4 0D heat equation

When the heat sources are homogeneous within the gauge zone of the specimen (in particular when the specimen deforms homogeneously), a so-called 0D approach has been proposed:

$$\rho C\left(\frac{\partial \Theta}{\partial t}+\frac{\Theta}{\tau_{\mathrm{0D}}}\right)=s_{\mathrm{int}} \qquad \text{1-66}$$

where $\Theta$ is the average temperature changes over the gauge zone of the specimen. It is worth noting that **temperature change homogeneity is not required**. In fact, the temperature profiles are in general strongly heterogeneous due to the contact with the metallic jaws of the testing machine. The hypothesis at the base of the 0D approach is the heat exchanged by contact with the jaws is *proportional* to the mean temperature change $\Theta$. This is verified in certain configurations [112,126,127].

In practice, the characteristic time $\tau_{\mathrm{0D}}$ can be simply identified by considering a natural cooling after preliminary homogeneous heating of the specimen simply “clamped in the jaws of the testing machine” (without axial loading). Indeed, the solution of Eq. 1-66 with $s_{\mathrm{int}}=0$ is an exponential decay:

$$\Theta_{\mathrm{cooling}}(t)=\Theta_0 \exp\left[\frac{-(t-t_0)}{\tau_{\mathrm{0D}}}\right] \qquad \text{1-67}$$

Two points can be noted:

- $\tau_{\mathrm{0D}}$ depends on the material properties (the thermal diffusivity in particular), the specimen geometry (radius and length) and the potential air flow around the specimen.
- $\tau_{\mathrm{0D}} < \tau_{\mathrm{1D}}$ because the contact with the jaws “accelerates” the heat exchanges of the specimen with its environment (compared with the heat exchanges by convection with ambient air only).

### 1.4.2 HSR processing overview

**Principle**

The first step of the method is to choose the version of the heat equation (0D, 1D or 2D) to describe the problem. In the case of an elongated specimen, it can be noted that both the 0D and 1D can be used along the test depending on whether the heat sources are (a priori) homogeneous or not. In the processing, it is necessary to calculate some differential operators (first-order time derivation and second-order spatial derivation). Despite all the precautions that can be taken when acquiring temperature data, these differential operators cannot be directly estimated by derivation of the temperature data (by finite differences for example) due to measurement noise. Indeed, the signal-to-noise ratio is generally small to obtain satisfactory results, especially for the second-order spatial derivation. Within the framework of the 0D approach (equation 1-66), the first-order differentiation (i.e., the time derivative) is an operation moderately sensitive to the measurement noise. On the other hand, for the 1D and 2D approaches, the second-order differentiation is very sensitive to noise, which was an obstacle to the method and has been a known problem since the first work using this method [69]. HSR thus relies primarily on signal processing algorithms to remove noise in a meaningful way. It should be noted that the strength of the approach is in the rapid numerical evaluation of the heat sources without knowing the theoretical thermal solution or the boundary conditions at the extremities of the specimens. The method can be qualified as direct. Note that indirect approaches for HSR also exist.

**Signal processing for HSR**

A wide range of different approaches have been developed in the literature to filter noise in a meaningful way: local polynomial approximation [128], recursive low-pass filters [117], Fourier transform [91,111], correct orthogonal decomposition [129,130], derived Gaussian filter [131], spatio-temporal filter [132], anisotropic gradient diffusion filter [133], among many others for smoothing thermal data.

**A study case**

Figure 1-33 shows the different operators reconstructed using a low-pass filter based on Fourier transform of a steel plate deformed in tension [90]. A 1D approach was used:

- Figure 1-33-a shows the spatio-temporal variation field of the temperature in K (the abscissa axis is the time, and the ordinate axis is the space, i.e. the vertical direction of the specimen). Two main events can be noticed. First from $t$ = 40 s to $t$ = 50 s, a “band” of temperature increase is clearly evidenced. Then, temperature mainly increases in the center of the specimen, reaching a maximum value at $t$ = 150 s before unloading the specimen.
- Figure 1-33-b and c show the spatio-temporal field of the derivative terms of the temperature. One can clearly see the localized “shape” of the event occurring from t = 40 s to t = 50 s.
- Figure 1-33-d shows the reconstructed space-time field of heat sources (i.e., the right-hand term of equation 1-63).

It can be noted that the kinetics of the thermal phenomena strongly induces the weight of each term of the heat diffusion equation. For example, a fast test will generate a higher weight of the time derivative. For different kinetics of thermal phenomena along a test, the filtering strategy should be adapted.

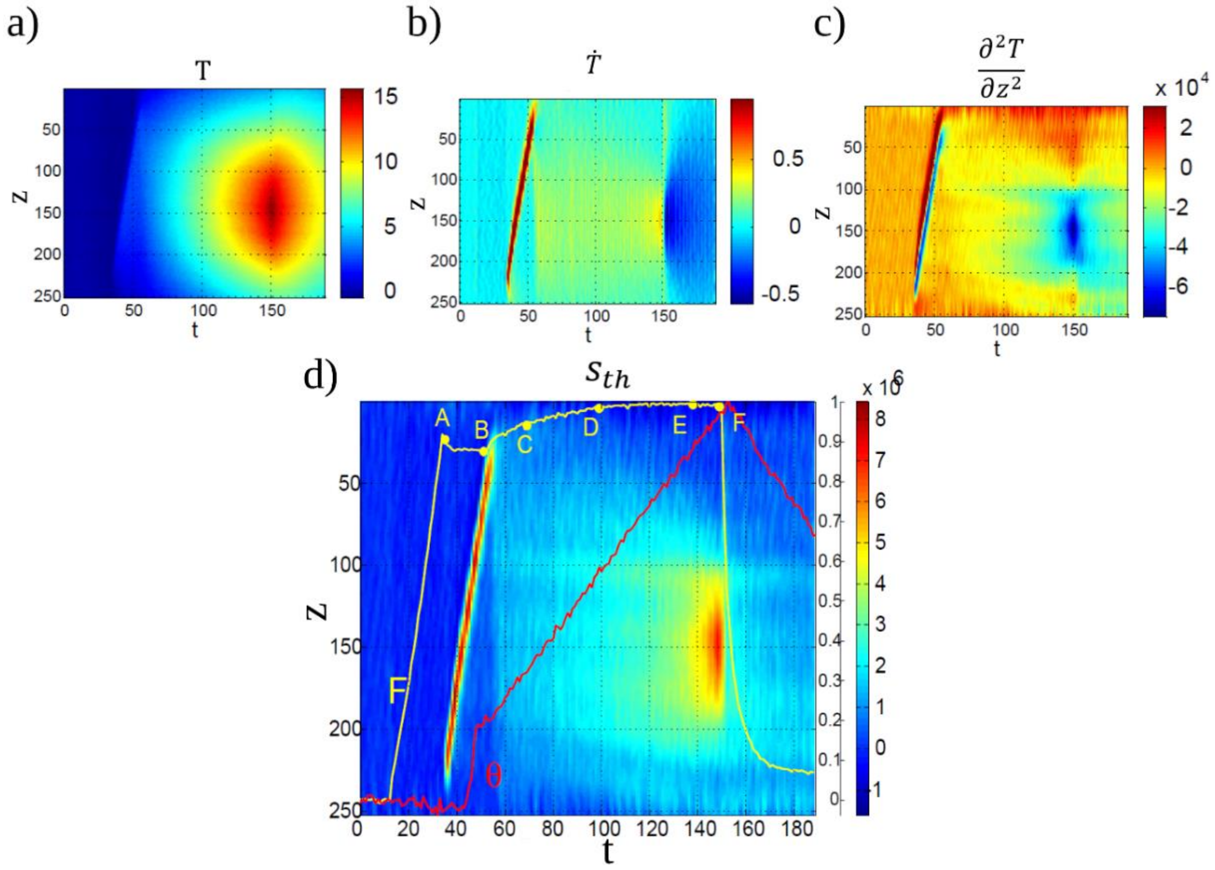

Figure 1-33: Example of 1D heat source reconstruction for a tensile test on S322MC steel: a) experimental thermal variation [K], b) first-order time derivative $[K.s^{-1}]$, c) second-order spatial derivative $[K.m^{-2}]$, d) heat source field $[W.m^{-3}]$ (adapted from [90]).

### Final remarks about HSR

In summary, HSR requires:

- the control of the experimental conditions to ensure that quantitative thermal data are obtained;
- a choice of spatial resolution and acquisition frequency of the thermal fields adapted to the object observed and to the kinetics of the thermal phenomena;
- the choice of a suitable form of the heat equation, consistent in particular with the geometry of the material specimen to be characterized;
- a thermal signal processing strategy appropriate to the spatio-temporal resolution of the thermal fields and to the kinetics of the thermal phenomena.

## 1.5 Conclusion

In this review chapter, we presented a background concerning all the critical points that this thesis work addressed. First of all, the fundamentals of NiTi SMAs were presented with emphasis on their thermo-mechanical couplings. Then we presented a review of the “deformation calorimetry”, which is a known technique but only rarely applied in mechanics of materials. In this context, a comparison between different proposed methods using infrared (IR) thermography was discussed. The mathematical framework of the thermomechanics of materials was also recalled. We presented two groups of “internal” heat sources (produced or absorbed by the material due to a change in its mechanical state):

- the thermo-mechanical couplings, including thermoelastic coupling and latent heat in the case of SMAs;
- the mechanical dissipation, also named intrinsic dissipation. This heat quantity is associated with any mechanical irreversible phenomena, typically plasticity.

We presented the bases of the heat source reconstruction (HSR) technique, which relies on the heat diffusion equation to measure the heat power density in a material specimen subjected to mechanical loading. The previous works using this method for NiTi were cited. In summary, HSR requires:

- the control of the experimental conditions to ensure that quantitative thermal data are obtained;
- a choice of spatial resolution and acquisition frequency of the thermal fields adapted to the object observed and to the kinetics of the thermal phenomena;
- the choice of a suitable form of the heat equation, consistent in particular with the geometry of the material specimen to be characterized;
- a thermal signal processing strategy appropriate to the spatio-temporal resolution of the thermal fields and to the kinetics of the thermal phenomena.

# Chapter 2. Reconstruction of heat sources induced in superelastically loaded Ni-Ti wire by localized deformation processes

## 2.1 Introduction

Based on the literature review in the previous chapter, it can be seen that only a few studies have been carried out using the full potential of infrared (**IR**) thermography with post-processing by heat source reconstruction (**HSR)** technique for nickel-titanium (**NiTi**) shape memory alloys (**SMA**s). A large collection of full-field IR measurements of NiTi under mechanical loading can be found (see for instance Refs [35,47,104,117,134–139]), but HSR has been applied only a few times [43,44,100,102,106,114,140]. Surprisingly, the one-dimensional (**1D**) approach of HSR has never been applied to NiTi SMA wires.

Let us recall that the macroscopic stress-strain curve of a superelastic NiTi wire generally presents a "stress plateau" in the case of a quasi-static displacement-controlled loading [15,29,30,141–144]. In such a case, the phase transformation generally manifests as one or two transformation fronts propagating along the wire. Conversely, multiple bands are expected for force-controlled loadings [35,137]. The nucleating and spreading phase transformation bands give rise to multiple heat bursts that lead to complex spatio-temporal temperature patterns, which are very challenging for HSR. We selected this problem of strong thermomechanical coupling for two reasons: firstly for its scientific relevance, as such force-controlled loading is expected in some applications such as shock dampers [145]; secondly to show how the HSR method is robust. The objective is to evidence and quantify the calorific signature of the forward and reverse phase transition, both in time and in space along the wire, proceeding at relatively high load rates during a force-controlled loading-unloading cycle.

This chapter is organized as follows:

- Section 1.2 is a brief reminder on the HSR in a 1D version, as well as in the zero-dimensional (**0D**) version which is relevant in the case of homogeneous heat source field;
- Section 1.3 presents the material, the test procedure and the experimental setup;
- Section 1.4 proposes an enhanced procedure to determine the heat exchange between the specimen and the surroundings, as well as a procedure for the evaluation of the thermal diffusivity of both austenite and martensite;
- Section 1.5 presents the experimental results and the reconstructed heat source fields;
- Section 1.6 discusses the results of the performed test.

## 2.2 A brief reminder on heat source reconstruction

To recall, we mean by a *heat source* or *internal heat source* the heat power density (in W.m$^{-3}$) produced or absorbed by a material due to a change in its physical state. Thermomechanics of materials distinguishes between two different groups of internal heat source origins as follows:

- *intrinsic dissipation* ($d_1 > 0$) due to any irreversible mechanical phenomena such as viscosity, plasticity, dislocations, cracks or fatigue damage. It is to be distinguished from the thermal dissipation $d_2$, both terms being involved in the Clausius-Duhem inequality $d_1 + d_2 > 0$;
- *thermomechanical couplings* ($s_{\mathrm{th-mec}}$) involving thermoelastic contribution ($s_{\mathrm{th-el}}$) present in all materials: $s_{\mathrm{th-el}}$ is negative when stress increases and positive when stress decreases. In SMAs, a latent heat term ($s_{\mathrm{transf}}$) is also involved: it is positive when A→M transformation occurs, and negative for the reverse transformation.

In the heat diffusion equation, the internal heat source appears through the total term $s_{\mathrm{int}} = d_1 + s_{\mathrm{th-mec}}$, i.e., $s_{\mathrm{int}} = d_1 + s_{\mathrm{th-el}} + s_{\mathrm{transf}}$:

$$\rho C \frac{dT}{dt} - k\,\overrightarrow{\mathrm{grad}}\,T = s_{\mathrm{ext}} + s_{\mathrm{int}} \qquad 2\text{-}1$$

where $\rho$ is the density (kg.m$^{-3}$), $C$ the specific heat (J.kg$^{-1}$.K$^{-1}$), $k$ the thermal conductivity (W.m$^{-1}$.K$^{-1}$), $T$ the temperature (K) and $s_{\mathrm{ext}}$ the power density of heat-induced by external field sources such as Joule heating induced by applied electrical field (W.m$^{-3}$).

Equation 2-1 can be reduced to a 1D version relevant in the case of long thin specimens [68,106,112,121,124,129,146–149]. It can be written in the following form after division by $\rho C$ and considering that $s_{\mathrm{ext}}$ does not vary in time during the temperature measurement:

$$\frac{\partial \Theta}{\partial t} + \frac{\Theta}{\tau_{\mathrm{1D}}(\Theta)} - D\frac{\partial^2 \Theta}{\partial z^2} = s \qquad 2\text{-}2$$

where $\Theta$ is the temperature change with respect to the equilibrium state, $\tau_{\mathrm{1D}}$ the characteristic time (s) for heat exchange between the specimen and ambient air, $D$ the thermal diffusivity (m.s$^{-2}$) along longitudinal direction $z$, and $s$ the internal heat source here expressed in K.s$^{-1}$ ($s = s_{\mathrm{int}}/\rho C$). This later quantity is simply named "heat sources" in the following, whatever the sign of $s$ (positive for a heat production or negative for heat absorption). Note that:

- $\Theta$ is a function of time $t$ and space $z$. An equilibrium state is defined in practice as the steady temperature field captured by the IR camera just before the beginning of mechanical loading. Thus $\Theta(z,t) = T(z,t) - T(z,0)$;
- $\tau_{\mathrm{1D}}$ is here assumed to be potentially dependent on temperature change $\Theta$, see Section 2.4.1 for its identification. For small temperature changes (a few K), it is usually considered as a constant and sometimes named $\tau_{\mathrm{th}}^{\mathrm{1D}}$ in the literature [16,26–34];

- thermal diffusivity is generally different for austenite and martensite. The superelastic SMA wire in the present study is entirely in the austenite phase at the beginning of the test at zero stress, i.e. $D(z,0) = D_{\mathrm{aust}}$, and progressively transforms to martensite upon loading.

A further simplification of the heat diffusion equation can be applied in the case of homogeneous heat source fields at the considered spatial resolution, i.e. when $s(z,t) = s(t)$. It is worth noting that this equality does not imply the homogeneity of the thermal profiles. The latter are generally heterogeneous because of the contact with metallic jaws and depend on the thermal history of the specimen along with the mechanical test. A so-called zero-dimensional (0D) version of the heat equation can then be used (see Refs [102,112,126,127] and references included):

$$\frac{d\Theta_{\mathrm{0D}}}{dt} + \frac{\Theta_{\mathrm{0D}}}{\tau_{\mathrm{0D}}(\Theta_{\mathrm{0D}})} = s \tag{2-3}$$

where $\Theta_{\mathrm{0D}}$ is the average temperature change over the specimen gauge length. The term $\tau_{\mathrm{0D}}(\Theta_{\mathrm{0D}})$ here is the characteristic time for heat exchange between the specimen and its entire environment, i.e. ambient air, IR radiation and jaws of the testing machine. For small temperature changes (a few K), it is usually considered as a constant and named $\tau$ or $\tau_{\mathrm{eq}}$ in the literature.

HSR can be performed by evaluating the heat source $s$ by *direct* calculation of the left-hand side of Equations 2-2 and 2-3. The strength of the approach is in the fast numerical evaluation of heat sources without knowing the theoretical thermal solution. The difficulty is that experimental data are unavoidably noisy (see equation 2-4), which is strongly penalizing for the calculation of the derivative terms. Thus, the acquired signal $\Theta(z,t)$ can be written as:

$$\Theta(z,t) = \Theta_{\mathrm{specimen}}(z,t) + n(z,t) \tag{2-4}$$

where $\Theta_{\mathrm{specimen}}(z,t)$ is the specimen thermal variation and $n(z,t)$ the noise to remove to obtain a proper HSR result. Among the various algorithms of thermal signal processing that were discussed in the chapter devoted to the bibliographical review, we have chosen the Gaussian Derivative Filter [150,151]. Thus, the processing was carried out by convolution with truncated derivative Gaussian functions, both for the time and spatial derivatives, in order to filter and derivate in a single operation as expressed by equation 2-5:

$$\frac{\partial^m \Theta(z,t)}{\partial x^m} = \Theta(z,t) * \left|\frac{\partial^m g}{\partial x^m}\right| \tag{2-5}$$

where * denotes the convolution operator, $x$ the differentiation "direction" ($z$ or $t$), $g$ a Gaussian kernel (which can be different for spatial and temporal differentiation), $\partial^m \Theta / \partial x^m$ the $m^{th}$ derivative of the thermal variation (with $m$=1 for the derivation in time, and $m$=2 for the derivation in space), and $|\partial^m g / \partial x^m|$ the norm of the $m^{th}$ derivative of the Gaussian kernel. This results in a one-step signal denoising and differentiation. The assessment of the cut-off frequency is difficult to define. There is a compromise between the measurement resolution, spatial resolution and temporal resolution. Due to the properties of the convolution, the data at the specimen boundaries are not well handled and induced errors in the reconstruction. Thus, we have chosen to crop the data at specimen boundaries to eliminate this filtering artifact beyond half size of the Gaussian kernel.

Note that an *indirect* approach for HSR was also used in the present study to determine the thermal diffusivity of the material (see Section 2.4.2). It consists of minimizing the error between experimental temperatures and theoretical temperatures provided by a selected model [86].

Compared to the analysis of the temperature fields that depend in particular on the specimen shape, the advantage of the approach by HSR is to "remove" effects of heat dissipation due to both heat conduction within the specimen and heat exchanges with the specimen environment. The former is removed through the term $-D\partial^2 \Theta/\partial z^2$ in the 1D approach. The latter is removed through the term $\Theta/\tau_{1\mathrm{D}}(\Theta)$ characterizing the heat exchanges with ambient air in the 1D approach, or the term $\Theta_{0\mathrm{D}}/\tau_{0\mathrm{D}}(\Theta_{0\mathrm{D}})$ characterizing the heat exchanges with the entire environment in the 0D approach.

## 2.3 Material and experimental setup

NiTi medical-grade wires, 1.78 mm in diameter, were supplied by Fort Wayne Metals in the as-drawn state with final cold work of 40 %. At first, 120 mm long specimens were placed into the hydraulic jaws of the servohydraulic Instron 8872 tensile machine so that 80 mm gauge length remained between the grips. Such clamped specimens were then heat-treated by Joule effect using a 100 A current for 0.875 s supplied between the grips and followed by natural cooling down to the room temperature. Then, to ensure the homogeneity of the specimen 20 mm at each end were cut-out to obtain a specimen of 80 mm and a final gauge length of $L$ = 40 mm, as depicted in Figure 2-1a,b. Finally, the specimens were subjected to mechanical training (not presented here) consisting of twenty superelastic loading-unloading cycles at room temperature up to 800 MPa in force control regime at ±400 N.s$^{-1}$. The training ensured the stability of the cyclic stress-strain response, which was essential for the repetitiveness of the results in our further research.

The in-situ thermography during a superelastic cycle was performed using an Infratec 8300 MWIR camera equipped with a close-up (0.3 m) telephoto lens (50 mm) and calibrated for the range [268 K,333 K] with noise equivalent temperature difference (NETD) of 20 mK at room temperature. 1D temperature profiles along the wire were all constructed by averaging over 14 pixels in the radial direction, as compared with the 22 pixels corresponding to the wire diameter. Useful IR data were thus captured on a surface featuring an inclination angle $\varphi$ with the camera axis in the range $\pm\arcsin(14/22)\times 180/\pi = \pm 40°$, i.e., on a surface with nearly-constant thermal emissivity $\varepsilon(\varphi)$ (as introduced in the review chapter). Note that the average operation enabled us to improve the measurement resolution of the temperature by reducing the noise by the square root of the number of considered pixels.

In the following, we mean by *measurement resolution* the change in quantity being measured that causes a change in the corresponding indication of greater than *one standard deviation* of the measurement noise [152]. Measurement resolution must be distinguished from the *spatial* and *temporal resolutions*, which can be defined as the minimum distance and minimum duration, respectively, between two *independent* measured quantities. The camera was synchronized with the loading waveform applied by the tensile machine. The specimens were sprayed with high thermal emissivity (0.96) paint that was also used for painting the grips and surroundings to limit parasitic reflections. The spatial and temporal resolutions of the temperature color map, defined here as the size of the pixel projected on the wire and the acquisition period of time, were equal to 82.6 µm and 2.86 ms respectively. These parameters are hereinafter denoted as $dz$ and $dt$, respectively.

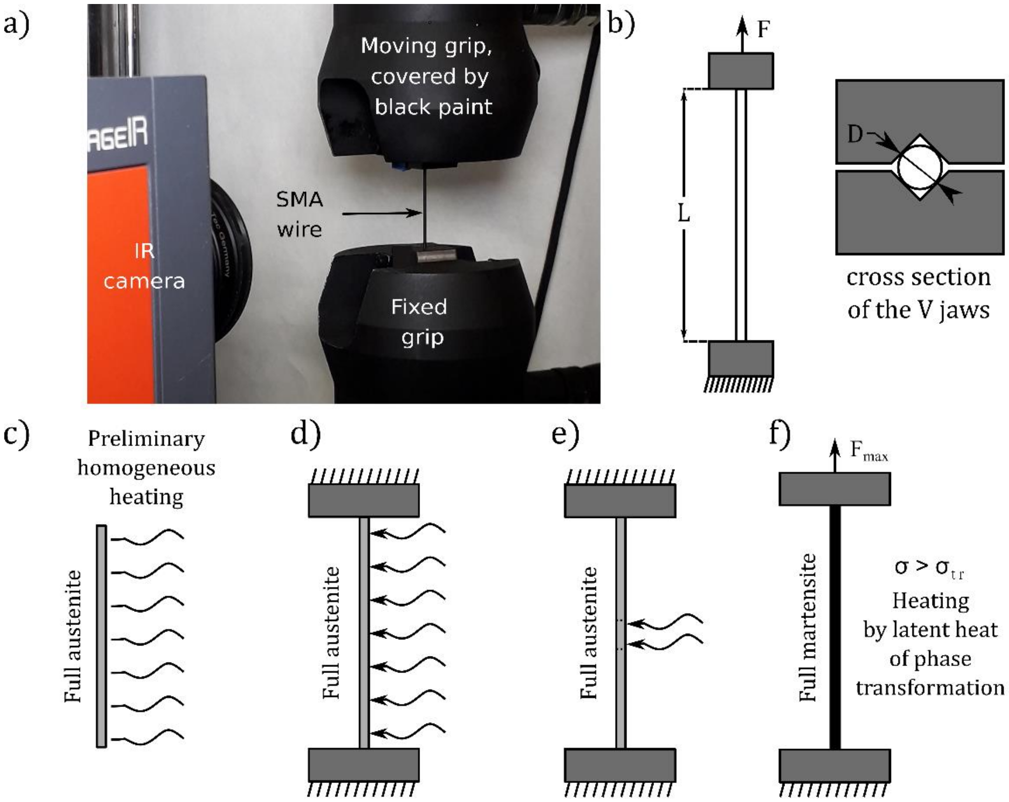

Figure 2-1: Experimental setups: **a)** photograph of SMA wire clamped in hydraulic jaws with installed IR camera; **b)** schematic view of a wire clamped in steel jaws. **c-f)** schemes for identification of thermophysical parameters to measure: characteristic time of heat exchange with surrounding air (c), characteristic time of heat exchange with entire surroundings i.e. air and jaws (d), thermal diffusivity of the austenite phase (e) and thermal diffusivity of the martensite phase (f).

## 2.4 Experimental identification of thermophysical properties

The procedure for HSR requires as inputs the values of thermophysical parameters, namely, the thermal diffusivity and parameters quantifying the heat exchange between the wire and its surroundings as defined in the Background section. Hereinafter, experimental methods used to identify the thermophysical parameters are presented. Finally, the values of thermal diffusivities identified for austenite and martensite phases are presented and compared with data available in the literature.

### 2.4.1 Heat exchange with the environment

In Equation 2-6, $\tau_{1\mathrm{D}}$ considers the heat exchanges with surrounding air and the IR radiation. The method used for its identification is based on preliminary homogeneous heating of the specimen suspended in the air (no contact with the jaws of the testing machine, see Figure 2-1c, followed by a natural return to equilibrium with measurement of temperature decay recorded by the IR camera and averaged over the wire length (negligible heat conduction along the $z$-axis, so $\Theta(z,t) = \Theta(t)$). In practice, the specimen was suspended using an adhesive tape and heated by passing an electrical current through two small electrode spots (50 µm) welded at both ends. In this way, we achieved homogeneous preheating, while creating negligible heat sinks during the natural return to the ambient temperature (electrode diameter of 50 µm as compared with the wire diameter of 1780 µm). Figure 2-2a shows a typical example of measured temperature decay. For homogeneous cooling of material not exhibiting any phase change, the temperature decay follows the equation 2-6 derived from 2-3 by excluding all heat sources ($s = 0$) and heat diffusion term ($-D\partial^2 \Theta/\partial z^2 = 0$):

$$\frac{d\Theta}{dt} + \frac{\Theta}{\tau_{1\mathrm{D}}(\Theta)} = 0 \qquad \text{2-6}$$

Parameter $\tau_{1\mathrm{D}}(\Theta)$ in Equation 2-6 characterizes the ability to exchange heat with the surrounding. Temperature dependence was piecewise-fitted by exponentially decreasing curves. Figure 2-2a shows an example of a fitted curve (in red). In practice, time intervals of 15 s were used. Red dots in Figure 2-2b are the values $\tau_{1\mathrm{D}}(\Theta_i)$ obtained, where $\Theta_i$ is the average temperature change over the time interval considered. Finally, the set of $\left(\Theta_i, \tau_{1\mathrm{D}}(\Theta_i)\right)$ pairs were fitted by an analytical function to obtain a continuous function $\tau_{1\mathrm{D}}(\Theta)$: see Equation 2-7 and the blue dashed curve in Figure 2-2b. Note that the discrepancy for $\Theta_i$ lower than about 2 K is explained by the fact that the signal-to-noise ratio of the curve $\Theta(t)$ decreases more and more when the latter tends toward zero.

$$\tau_{1\mathrm{D}}(\Theta) = 52.1 + 33.8 \times \exp\left(\frac{-\Theta}{5.3}\right) \qquad \text{2-7}$$

For comparison purposes, a constant value for $\tau_{1\mathrm{D}}$ was also determined by fitting the complete recorded temperature curve: $\tau_{1\mathrm{D}}$ = 58 s (horizontal black line in Figure 2-2b. To quantify the increase in accuracy when considering the temperature-dependent heat exchange parameter as opposed to the constant one, residual heat sources and their histograms are compared in Figure 2-2c, d. Heat sources are equal to zero for a natural return to ambient temperature. Residual heat sources obtained by HSR are closer to zero using $\tau_{1\mathrm{D}}(\Theta)$ than using the constant value $\tau_{1\mathrm{D}}$ = 58 s; see also the lower standard deviation of related histograms in Figure 2-2d. Note that even if residual heat sources are significantly greater for $\Theta$ greater than 18 K, values remain smaller to -0.08 K.s$^{-1}$ and -0.04 K.s$^{-1}$ for $\tau_{1D}$ constant or not respectively, which are several orders of magnitude lower than the amplitude of the calorific events observed during the superelastic tests.

The same procedure was applied from the configuration in Figure 2-1d to identify the $\tau_{0\mathrm{D}}(\Theta_{0\mathrm{D}})$ function in Equation 2-3 considering 0D HSR approach, leading to:

$$\tau_{0\mathrm{D}}(\Theta_{0\mathrm{D}}) = 35.5 + 15.7 \times \exp\left(\frac{-\Theta_{0\mathrm{D}}}{7.7}\right) \qquad \text{2-8}$$

It can be noted that $\tau_{0\mathrm{D}} < \tau_{1\mathrm{D}}$, which is consistent with their respective definitions where $\tau_{0D}$ characterizes both heat exchanges with the air by convection, with the electromagnetic IR radiation by surrounding objects and with the jaws by conduction whereas $\tau_{1D}$ characterizes the convective and radiative contributions. Finally, note that formulae in Equations 2-7 and 2-8 are considered as "symmetric" in the sense that $\tau_{1\mathrm{D}}(\Theta)$ and $\tau_{0\mathrm{D}}(\Theta_{0\mathrm{D}})$ become $\tau_{1\mathrm{D}}(|\Theta|)$ and $\tau_{0\mathrm{D}}(|\Theta_{0\mathrm{D}}|)$ respectively. In other words, characteristic times of heat exchange are assumed to be the same below and above room temperature.

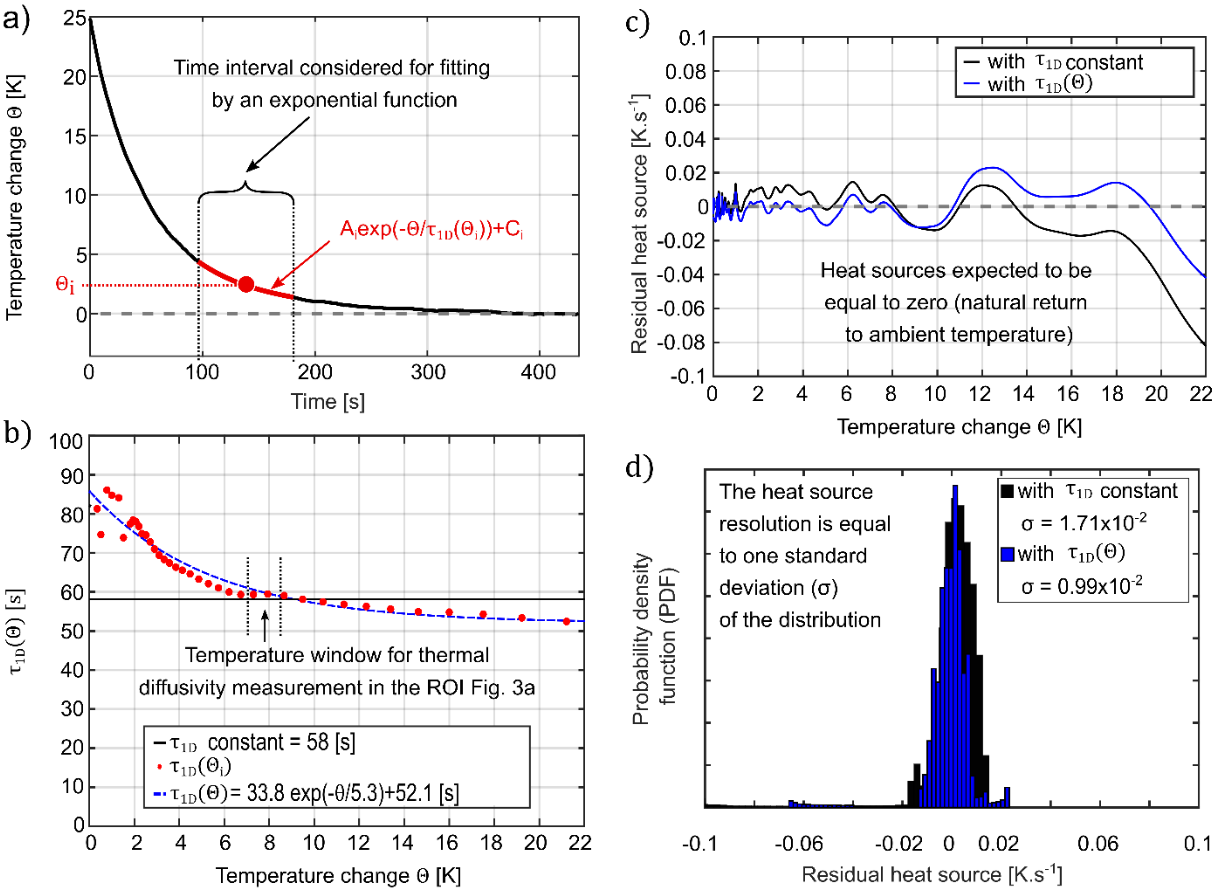

Figure 2-2 : Evaluation of the heat exchanges: **a)** natural cooling of the specimen in the configuration depicted in Figure 2-1c; **b)** constant and temperature-dependent characteristic times of heat exchange with the surrounding air; **c)** time evolutions of residual heat sources; **d)** histograms of residual heat sources.

### 2.4.2 Thermal diffusivity

To the best knowledge of the authors, the use of thermography for the assessment of *in-plane* thermal diffusivity was firstly proposed in Ref. [153] using an indirect approach. In Refs [68,153–157], the authors determined the thermal properties of NiTi specimens both using conventional methods and from thermographs processed by direct approach. In the present study, both direct and indirect approaches were applied to determine the thermal diffusivities of both austenite and martensite phases. Sections 2.4.2.1 and 2.4.2.2 present respectively both the methods while the following section presents identified values of thermal diffusivities of both the phases in comparison to data available in the literature.

#### 2.4.2.1 Direct method

In practice, the specimen is clamped in jaws and locally heated by using small electrodes, 10 mm spaced as shown in Figure 2-1d,e,f while recorded natural cooling is reduced into a 1D spatio-temporal colormap as shown also in Figure 2-3a. This color map is then used to directly calculate the thermal diffusivity from Equation 2-2, which in the case of no internal heat sources reduces to Equation 2-9 as follows:

$$D = \frac{\frac{\partial \Theta}{\partial t} + \frac{\Theta}{\tau_{1\mathrm{D}}(\Theta)}}{\frac{\partial^2 \Theta}{\partial z^2}} \qquad \text{2-9}$$

Numerically, Equation 2-9 is evaluated using Gaussian derivative filters [151] at each pixel and at each time of region of interest (ROI) defined in space and time. Figure 2-3a shows the input data, i.e. the thermal field $\Theta(z,t)$. ROI was properly selected to maximize the signal-to-noise ratio (SNR) of the temperature field. This selection is in particular dictated by the evaluation of the second derivative in the denominator $\partial^2 \Theta / \partial z^2$ being highly sensitive to SNR. Note that during natural cooling both numerator and denominator in Equation 2-9 tend to zero, which is a decisive factor for time interval selection. Figure 2-3b presents the field $D(z,t)$ related to the austenite phase of the studied material and calculated in the ROI shown in Figure 2-3a. Figure 2-3c shows the histogram of $D(z,t)$, where its mean value is considered as the value of diffusivity. Finally, the quality of thermal diffusivity identification is assessed by evaluating the residual heat sources as shown in Figure 2-3d for the austenite phase. To quantify the quality of measurement, the average values and scatters of the histogram extracted from the residual heat source color map were evaluated. Figure 2-3e presents a histogram of the residual heat sources obtained; the mean value of the distribution is centered at 0 and the standard deviation is about 0.02 K.s$^{-1}$.

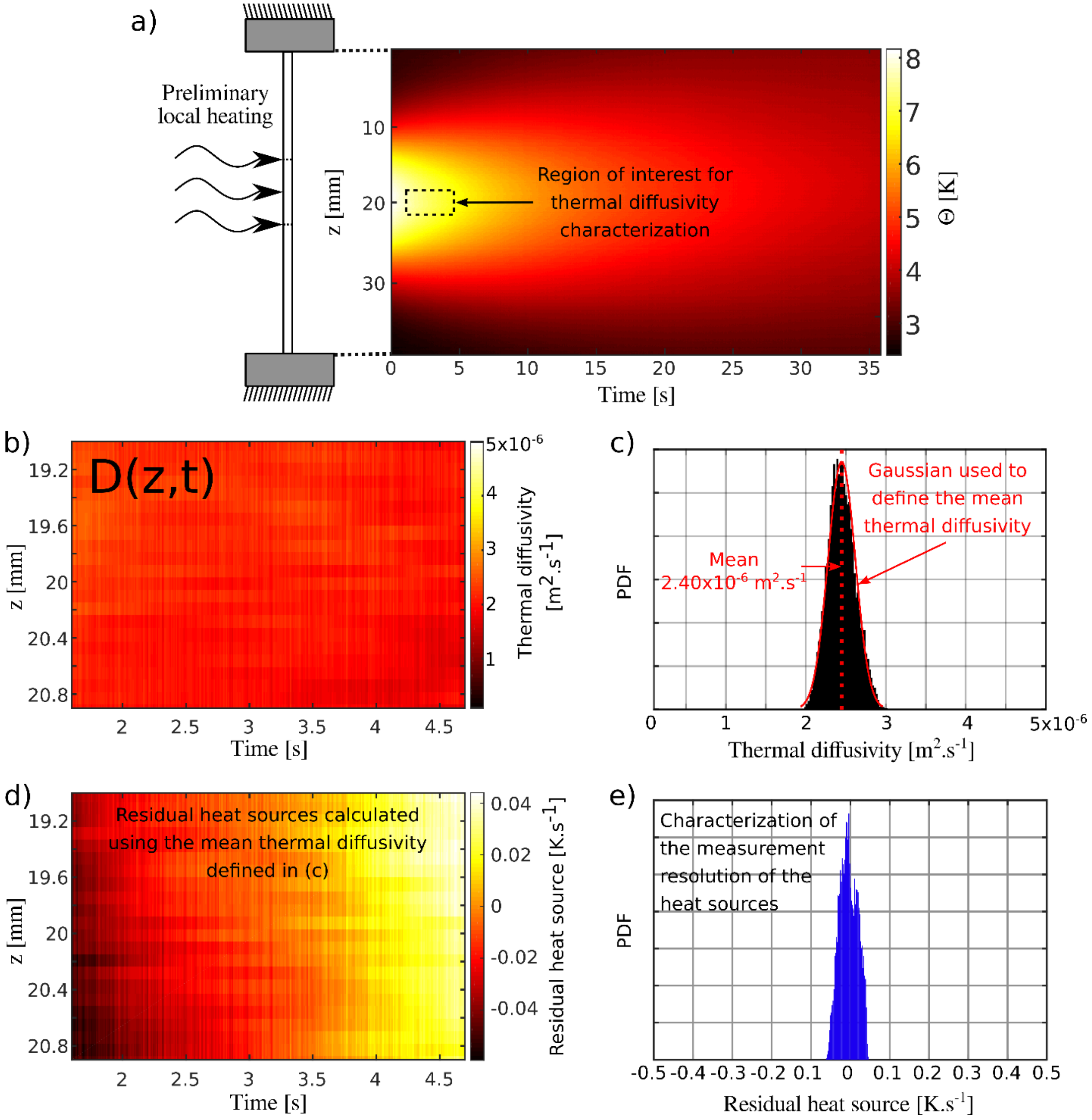

Figure 2-3: Evaluation of the thermal diffusivity: **a)** temperature colormap after preliminary local heating as depicted in Figure 2-1e and spatio-temporal region of interest (ROI) for identification of the austenite thermal diffusivity; **b)** thermal diffusivity color map determined by direct method on the ROI; **c)** thermal diffusivity histogram over the ROI; **d)** color map of residual heat sources evaluated on the ROI; **e)** residual heat source histogram over the ROI.

### 2.4.2.2 Indirect method

The indirect method is based on the comparison between the temperature field recorded during natural cooling as described previously and the theoretical temperature field calculated from a model. Theoretical temperature field $\theta_{\mathrm{model}}$ is a solution of the following equation including initial and boundary conditions:

$$\frac{\partial \theta_{\mathrm{model}}}{\partial t} + \frac{\theta_{\mathrm{model}}}{\tau_{1\mathrm{D}}(\theta_{\mathrm{model}})} - D\frac{\partial^2 \theta_{\mathrm{model}}}{\partial z^2} = 0 \tag{2-10}$$

$$\theta_{\mathrm{model}}(z,0) = \theta(z,0) \tag{2-11}$$

$$\theta_{\mathrm{model}}(L,t) = \theta(L,t) \tag{2-12}$$

$$\theta_{\mathrm{model}}(0,t) = \theta(0,t) \tag{2-13}$$

The unknown diffusivity in Equation 2-10 is determined from a minimization problem 2-14, where the absolute value of the difference between theoretical and experimental temperature fields is being minimized.

$$(D_{\mathrm{aust}})_{\mathrm{indirect}} = \underset{D\in[10^{-8},10^{-4}]}{\operatorname{argmin}} \left(|\theta - \theta_{\mathrm{model}}|\right) \tag{2-14}$$

Note that experimental data are used as the initial condition (Equation 2-11) and boundary conditions at the two ends of the wire $z$ = 0 and $z$ = $L$ (Equations 2-12 and 2-13, respectively). The minimization problem 2-14 was solved in Matlab® environment using *fminbnd* function while Equation 2-10 was resolved at each iteration using the Method of Lines [158] employing Ordinary Differential Equation solver *ode15s* for time solver where the finite differences were used to compute the spatial derivative. As a measure of the quality of determination of thermal diffusivity using the indirect approach, the distribution of temperature differences between measurement and model is evaluated in terms of average value and standard deviation as shown in Figure 2-4 for the case of the austenite phase of the studied material. Note that the standard deviation, in this case, is in good agreement with NETD, i.e. the so-called measurement resolution of the IR camera given by the manufacturer.

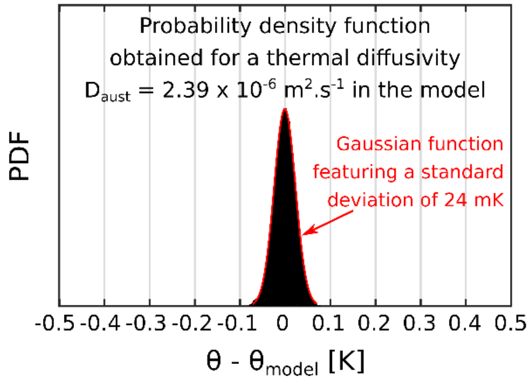

Figure 2-4 : Statistical mismatch between measured temperatures and theoretical temperatures calculated using the thermal diffusivity of the austenite phase estimated by the indirect method

Table 1 : Summary of the thermal diffusivities and related residual heat sources as identified using direct and indirect method considering constant and temperature-dependent heat exchange parameters. Residual heat results are provided in terms of mean value μ and standard deviation $\sigma$

| | | Austenite | | Martensite | |
|---|---|---|---|---|---|
| | | $\tau_{1D}$ constant | $\tau_{1D}(\Theta)$ | $\tau_{1D}$ constant | $\tau_{1D}(\Theta)$ |
| Direct method | Thermal diffusivity [$m^2.s^{-1}$] | $2.43\times10^{-6}$<br>$\pm0.2\times10^{-6}$ (±8%) | $2.41\times10^{-6}$<br>$\pm0.2\times10^{-6}$ (±8%) | $3.07\times10^{-6}$<br>$\pm0.8\times10^{-6}$ (±26%) | $3.15\times10^{-6}$<br>$\pm0.3\times10^{-6}$ (±10%) |
| | Residual heat source [$K.s^{-1}$] | $\mu = -6.5\times10^{-4}$<br>$\sigma = 9.2\times10^{-3}$ | $\mu = -4.5\times10^{-4}$<br>$\sigma = 8.4\times10^{-3}$ | $\mu = 7.4\times10^{-5}$<br>$\sigma = 2.0\times10^{-2}$ | $\mu = 7.6\times10^{-5}$<br>$\sigma = 2.0\times10^{-2}$ |
| Indirect method | Thermal diffusivity [$m^2.s^{-1}$] | $2.39\times10^{-6}$ | $2.39\times10^{-6}$ | $3.24\times10^{-6}$ | $3.23\times10^{-6}$ |
| | Residual heat source [$K.s^{-1}$] | $\mu = 4\times10^{-4}$<br>$\sigma = 2.1\times10^{-2}$ | $\mu = -1\times10^{-4}$<br>$\sigma = 2.1\times10^{-2}$ | $\mu = 7.2\times10^{-3}$<br>$\sigma = 4.2\times10^{-2}$ | $\mu = 1.4\times10^{-2}$<br>$\sigma = 4.2\times10^{-2}$ |

#### 2.4.2.3 Summary on thermal diffusivity

Table 1 presents the mean values and standard deviations of thermal diffusivity of austenite and martensite phases as measured by both the direct and indirect methods when considering both the constant and temperature-dependent heat exchange parameters. Besides, the mean values and standard deviations of residual heat sources are presented I n

Table 1 as accuracy quantifiers for individual determinations of the thermal diffusivity. Note that the diffusivity of martensite was also identified so that the martensite was stress-induced in NiTi specimen using a prestress of 800 MPa being above the stress level $\sigma_{tr}$ needed to stress-induced the martensite at room temperature. Therefore, the value of martensite diffusivity is related to so-called detwinned (oriented) martensite. It can be concluded from

Table 1 that the values of the thermal diffusivity of austenite coincide when rounding to the first digit, while the values identified for the martensite present a scatter within the first digit. Values are compared in Table 2 with the literature. The latter shows a large scatter which can be attributed to the fact that the values were identified using different methods (DSC, Flash 3ω method) on various NiTi alloys and heat treatments. Nevertheless, we can conclude that the values from the present study are inferior to all cited values and that they match reasonably well to those in Ref. [157]. Note that to the best knowledge of the authors, literature provides values only for self-accommodating martensite while our method allows identifying the thermal diffusivity of stress-induced martensite. Therefore, the present work assessed for the first time the thermal diffusivity of detwinned martensite being higher by a factor of 1.3 compared to that of austenite.

Table 2 : Comparison of values of the thermal diffusivity [$10^{-6}$ $m^2.s^{-1}$] of NiTi SMAs available in the literature and identified in the present study

| | Faulkner [155] | Zanotti [156] | Zanotti [157] | Rohde [154] | Delobelle [110] | Present study |
|---|---|---|---|---|---|---|
| Austenite | 7.39 | 3.2<br>(at 390 K) | 3.0<br>(at 375 K) | 6.25<br>(at 373 K) | 3.83 | 2.40<br>(at 298 K) |
| Self-accommodating martensite | 4.85 | 3.8<br>(at 320 K) | 3.2<br>(at 340 K) | 5.58<br>(at 273 K) | 4.37 | / |
| Oriented martensite | / | / | / | / | / | 3.17<br>(at 298 K) |

## 2.5 Heat sources due to stress-induced martensitic transformation

Heat sources due to stress-induced phase transitions were analyzed in superelastic NiTi wire by using the previously introduced HSR method. Let us recall that 20 superelastic (SE) cycles at ±400 $N.s^{-1}$ were applied as detailed in Section 2.3 prior to application of the HSR method on the 21st SE cycle, at ±20 $N.s^{-1}$. A lower rate was applied to limit the number of sites of the martensitic transformation nucleation thus facilitating the analysis of heat source patterns.

### 2.5.1 Macroscopic thermomechanical response

SE cycle consisted of loading-unloading the NiTi wire in force-control regime at ±20 N.s$^{-1}$. Table 3 sums up all experimental setup parameters including temporal and spatial resolutions of temperature field measurements. The macroscopic thermomechanical response of the wire was evaluated in terms of stress, strain, and temperature; defined as nominal stress, engineering strain, and average temperature calculated respectively from the applied force, measured grip's displacement, and spatially averaged temperature fields of the wire's gauge section. Figure 2-5a shows a rather typical superelastic stress-strain curve (blue line) with superimposed temperature-strain evolution (red line) showing maximum and minimum temperatures at the ends of upper and lower plateaus, respectively. These extreme values reflect near completion of the forward and reverse martensitic transformations, respectively, during which the latent heat of the phase transformation is being released and absorbed, respectively (residual austenite or martensite may have continued to transform after the stages of extreme activity of heat sources). The extreme values are close to temperature gradients reported in the literature for quasi-adiabatic loadings [46,104,136]. In fact, the force control loading employed in this work approaches adiabatic conditions as the forward and reverse martensitic transformation in NiTi wires proceeds via nucleation and propagation at constant stresses [30]. Therefore, high strain rates are reached during the forward and reverse transformation as reported in Figure 2-5b showing the time evolution of strain (blue line) with the superimposed time evolution of average temperature (red line) showing sharp maximum and minimum indicating the highest rate of forward and reverse martensitic transformation. Note that the high-temperature gradients reached during forward and reverse martensitic transformations lead to inclined stress plateaus that are horizontal (black dashed line in Figure 2-5a) for isothermal loading. The inclination is due to the temperature dependence of transformation stresses being for NiTi wires approximately 6 MPa.K$^{-1}$ [159].

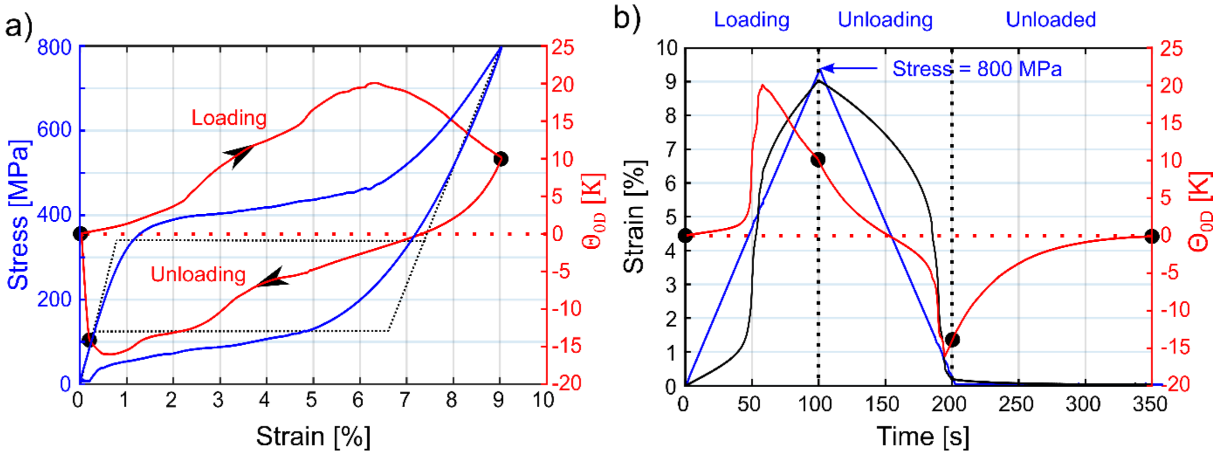

Figure 2-5 : Macroscopic response during the superelastic cycle: **a)** temperature (averaged over the whole gauge length of the wire) vs. engineering strain curve (red solid line), engineering stress vs. engineering strain curve (blue solid line), and scheme of isothermal superelastic response (black dashed line); **b)** time evolutions

Table 3: Parameters of the mechanical test and thermographs acquisition used in the reconstruction of heat sources on NiTi wire subjected to superelastic cycle.

| Symbol | Definition | Value |
|---|---|---|
| $L$ | Gauge length of the SMA wire | 40 mm |
| $D$ | Diameter of the wire | 1.78 mm |
| $F_{\mathrm{max}}/\sigma_{\mathrm{max}}$ | Maximal force/stress | 2000 N/800 MPa |
| $F_{\mathrm{min}}/\sigma_{\mathrm{min}}$ | Minimum force/stress | 20 N/8 MPa |
| $\dot{F}/\dot{\sigma}$ | Force rate/Nominal stress rate | $\pm$20 N.s$^{-1}$ /8 MPa.s$^{-1}$ |
| $T_{\mathrm{room}}$ | Room temperature | 298 K |
| $dt$ | Temporal resolution of the thermal measurement | 2.86 ms (350 Hz) |
| $dz$ | Spatial resolution of the thermal fields | 82.6 μm |

### 2.5.2 Heat sources

HSR during the SE cycle is based on the recorded time evolution of the temperature field during loading-unloading and final stress-free natural cooling. As discussed previously, the cylindrical specimen's geometry allows the dimensional reduction of the problem into 1D. Hence, the time evolution of the temperature field may be represented by a spatio-temporal color map, where columns are associated with the time of individually recorded specimen thermographs averaged in the transversal direction, while rows are associated with actual positions of material points along the wire axis. Note that the vertical spatial axis was limited to those material points that remained within the field of view during the complete SE cycle. The spatio-temporal color maps as recorded in the present work are shown in Figure 2-6a with the superimposed time evolution of engineering axial strain responding to linear force increase/decrease during the force control loading and unloading. The colormaps in Figure 2-6a are split by black verticals into time segments according to test stages – loading, unloading, and unloaded stage, where the specimen experienced stress-free cooling. In addition, the loading and unloading segments are marked with pairs of dashed white lines delimiting the occurrence of forward and reverse martensitic transformation. Figure 2-6b,c show in detail these zones, where the latent heat released/absorbed during forward/reverse transformation creates spatio-temporal temperature gradients. These temperature gradients reveal initiations of individual transformation events that clearly occur in two sequences. However, the ends of individual events cannot be resolved as they are hidden in the overall temperature change due to heat diffusion. Thanks to 1D HSR, the ends can be detected as seen in the corresponding heat source color map shown in Figure 2-6d,e that reveals the complete information on the spatial range and time duration of transformation events as well as on the magnitude and sign of related heat sources. As the transformation events bring about the transformation strain, the latter is superimposed in red/blue solid lines in Figure 2-6b-e for better interpretation of HSR in terms of phase transformation activity discussed in the next section. Note that the heat source color map was identified in two steps. First, an average value of heat diffusivity from that of austenite and martensite was assumed to perform approximate HSR revealing localized transformation events, which enables the creation of the binary color map shown in Figure 2-6f. This color map clearly delimits spatio-temporal zones of near full martensite from zones from parent phase(s). Then HSR was refined by assigning the zones of near full martensite the diffusivity of martensite while the other zones were assigned the diffusivity of austenite. Heat sources identified using the 0D HSR approach are reported in Figure 2-6g. Thanks to the use of the 0D approach allowing for a spatial integration of recorded thermographs, an evolution of heat sources lower than 1 K.s$^{-1}$ could be successfully identified. Note that the temporal resolution (for the 0D and 1D approaches) and the spatial resolution (for the 1D approach) of the heat sources color map were equal to 17.2 ms and 744 µm respectively. These values resulted from the choice of the filtering parameters detailed in Ref. [160] (Appendix A).

See next page

Figure 2-6 : Thermography and HSR during the superelastic cycle: **a)** time evolution of thermographs represented by a colormap where columns and rows represent times and wire axial direction respectively; **b), c)** details of the temperature colormap delimited by the white vertical dashed lines, focusing on the time intervals of localized forward/reverse phase transformation, respectively; **d), e)** heat sources reconstructed over the two selected time intervals; **f)** binary color map of martensite phase distribution based on identified localized transformation events; **g)** time evolution of weak heat sources (WHS) reconstructed in time intervals where no localized events appeared.

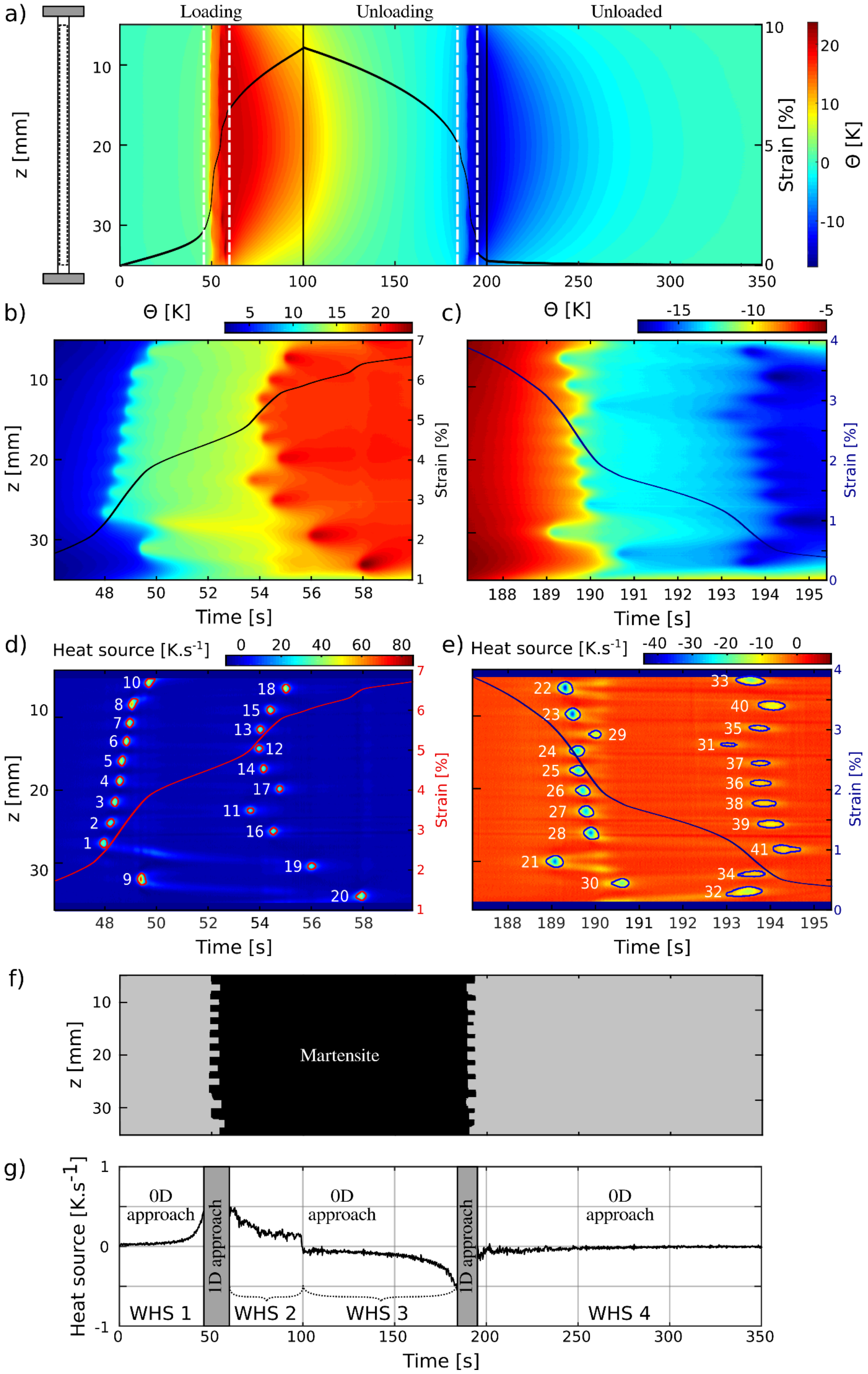
a)
Loading
Unloading
Unloaded
z [mm]
Strain [%]
Θ [K]
b)
Θ [K]
Strain [%]
Time [s]
c)
Θ [K]
Strain [%]
Time [s]
d)
Heat source [K.s$^{-1}$]
Strain [%]
Time [s]
1 2 3 4 5 6 7 8 9 10 11 12 13 14 15 16 17 18 19 20
e)
Heat source [K.s$^{-1}$]
Strain [%]
Time [s]
21 22 23 24 25 26 27 28 29 30 31 32 33 34 35 36 37 38 39 40 41
f)
z [mm]
Martensite
g)
Heat source [K.s$^{-1}$]
0D approach
1D approach
0D approach
1D approach
0D approach
WHS 1
WHS 2
WHS 3
WHS 4
Time [s]

## 2.6 Heat source analysis and discussion

HSR during the SE cycle reveals the localization, kinetics, and magnitude of heat effects during solid-solid phase transformation. Applying both 0D and 1D HSR approaches allowed us to identify weak heat effects as well as localized heat effects. The magnitude of heat sources (heat power density) identified at each time increment of the SE cycle may be considered as a superposition of all potentially active heat sources, namely, the latent heat of phase transformations, intrinsic dissipation, and thermoelastic coupling. However, the latter will be neglected in the present discussion as it is a weak heat effect estimated to about -0.008 $K.s^{-1}$ for austenite under adiabatic conditions, which is a value being on average 3 orders of magnitude lower than maxima of localized effects and 1 order of magnitude lower than weak heat sources. Considering this assumption, HSR reflects primarily the latent heat being positive in the case of the forward martensitic transformation induced by loading and negative in the case of the reverse martensitic transformation taking place upon unloading superimposed with the heat due to the intrinsic dissipation being strictly positive in both loading and unloading. Provided that these two heat sources can be distinguished, HSR can be used to track down the progress of the stress-induced martensitic transformation with a spatio-temporal resolution since the latent heat scales with the variation of the volume fraction of martensite, similarly to the transformation strain or electric resistivity.

The reconstructed localized heat sources and simultaneously measured strain evolutions in Figure 2-6d, e can be associated with the progress of the stress-induced martensitic transformation. Upon loading (Figure 2-6d), the occurrence of multiple positive heat sources along with an increase of the strain rate is indirect evidence of the forward localized exothermic stress-induced martensitic transformation into detwinned martensitic crystalline structure bringing about a transformation strain in the direction of the loading. Upon unloading (Figure 2-6e), the occurrence of negative heat sources along with an increase of the magnitude of strain rate is an indirect evidence of the localized reverse endothermic stress-induced martensitic transformation into austenite accompanied with the recovery of the transformation strain.

### 2.6.1 Patterns of transformation events

HSR enables to interpret patterns of transformation events in terms of the thermomechanical coupling that is particularly strong in the case of force-controlled loading and unloading applied in the present work. Under this regime, the strain rates may become very high, particularly when the stress-induced transformation proceeds under isothermal conditions. As illustrated by the black dashed curve in Figure 2-5a, the isothermal response features stress plateaus associated with the forward (upper plateau) and reverse (lower plateau) martensitic transformation accompanied by transformation strains that appear and disappear when reaching the plateau stresses during forward and reverse martensitic transformation, respectively. Therefore, the transformation would theoretically occur almost instantaneously when the controlled force would have reached the transformation stress levels. However, under real non-isothermal conditions, the latent heat locally generated/absorbed by the forward/reverse transformation increases/decreases the temperature of the material volume in the neighborhood of the transforming material thus increasing/decreasing the stress (Figure 2-6b,c) required to transform the neighboring material volume since the transformation stress is temperature-dependent. Consequently, the superelastic response becomes rate-dependent, as illustrated in Figure 2-5a comparing theoretical isothermal stress-strain curve (black dashed curve) with stress-strain response measured under force-controlled regime (blue solid curve) [35,46,47,104,134,136,161].

#### 2.6.1.1 Forward martensitic transformation

In the case of the loading (Figure 2-6b), the fast martensite nucleation leads to local heating of surrounding not yet transformed material thus increasing locally the transformation stress approximately by a factor of 6 MPa.K$^{-1}$ [159]. Consequently, the propagation of martensite band fronts into their surrounding is hindered since the stress required for the forward transformation has been locally increased in this volume. As a result, a new nucleation site is created at a distant location not affected by released latent heat. These processes of nucleation bursts and transformation arrests proceed along the axis of the wire as seen in Figure 2-6d where the reconstructed heat sources 1-10 represent the nucleation sites. The nucleated martensite bands bring about the transformation strain, which adds up to the elastic strain and increases the measured strain rate, as confirmed by strain measurement overlapped in Figure 2-6d. As a result of the sequence of 10 transformation nucleation events, the temperature of the specimen is homogeneously increased by 12 K, which leads to an increase of transformation stress by 72 MPa. With the applied loading rate of 8 MPa.s$^{-1}$ (see Table 3), 9s were necessary after the first burst to reach the increased transformation stress. During this period of time, the martensitic transformation was indeed suppressed as indicated in Figure 2-6b by the absence of heat sources and a decrease in strain rate. Finally, when the increased transformation stress was reached pairs of martensite band fronts from adjacent nucleation sites start to propagate until they merge. This proceeded again sequentially in locations 11-20 due to the effect of local temperature changes as in the case of the nucleation sequence.

#### 2.6.1.2 Reverse martensitic transformation

Analogically to the forward martensitic transformation, the reverse transformation proceeded in two stages – austenite sequential nucleation in locations 21-30 (Figure 2-6e), followed by a short band fronts propagation, and sequential merging of martensite bands in locations 31-41 by austenite band fronts propagations from nucleation sites. The evolution of strain during the reverse transformation confirms this process as the magnitude of the negative strain rate increased during the sequences of nucleation and band fronts propagations.

#### 2.6.1.3 Summary

To sum up, the local temperature changes due to latent heat release/absorption lead first to sequential forward/reverse martensitic transformation nucleated at several nearly equidistantly located sites. These events are followed by short propagations of band fronts that are arrested by a homogeneous increase/decrease of the specimen temperature as the thermodynamic conditions for martensitic transformation are not satisfied. The transformation via merging of martensite band fronts is completed only after the controlled external tensile force reaches the transformation stress at actual increased/decreased temperature. The sites of nucleation and band front merger can be characterized through its width along the wire axis, kinetics, and magnitude of heat sources. A characteristic width of these events was identified to be in all cases similar to the diameter size (see Figure 2-7b-e and Figure 2-8d,e), which is in agreement with the size of the martensite band front analyzed in detail by the 3D-XRD method in Ref. [29].

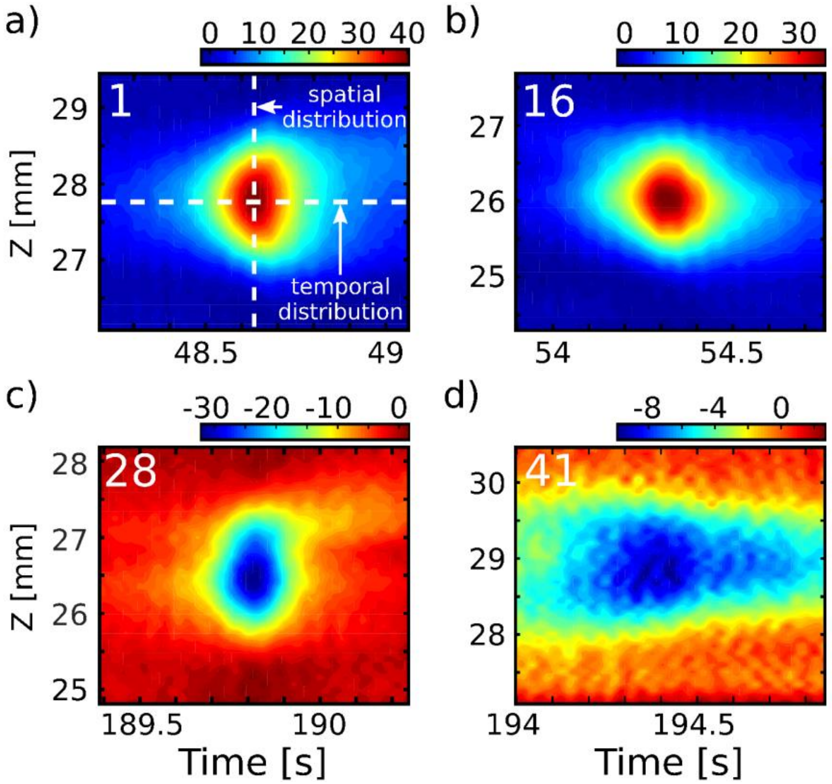

Figure 2-7 : Focus over different localized events: **a, b)** spatio-temporal color matrices of reconstructed localized heat sources in $K.s^{-1}$ related to martensite nucleation and merging events that appeared during loading at locations 1 and 16 as depicted in Figure 2-6d, respectively; **c), d)** same for austenite nucleation and merging events that appeared during unloading at locations 28 and 41 as depicted in Figure 2-6e, respectively.

### 2.6.2 Weak heat sources prior and post localized heat effects

Weak heat sources were identified in time intervals, indicated by the "0D approach" in Figure 2-6g, where no local heat sources were active. The weak heat sources were about 100 times lower than the localized heat effects. Positive weak heat sources were identified during the loading stage, where they progressively increased during the loading prior to the appearance of the localized heat sources. The weak heat sources reappeared and exponentially decreased during loading when the activity of localized heat sources ceased. During unloading, the negative weak heat sources appeared with an increased magnitude prior to the appearance of the localized heat sources. Weak heat sources reappeared again when the activity of the localized heat events ceased.

The identified weak heat sources cannot be solely due to thermoelasticity since the weak heat sources are positive during loading and negative during unloading, i.e., the signs are inversed in comparison to temperature effects due to the thermoelasticity. The weak sources may be signs of martensitic transformation initiated prematurely at sites of the microstructure with preferable conditions for the transformation induced by previous training. The positive heat effects during loading prior to the localized heat effects might also be assigned to austenite-R-phase transformation [43,44,138,159], transformation paths established by the previous training [15], or other precursors events. Although the intensity of these heat sources is weak, the amount of heat generated or absorbed was non-negligible as they were active for a longer time compared to the localized heat sources. The intensities of heat sources are discussed in the following section.

### 2.6.3 Spatio-temporal distributions and intensities of heat sources

As discussed previously, the recorded localized heat sources may be categorized into four types of events: martensite nucleation and merging events appearing upon loading at locations 1-10 and 11-20, respectively, as shown in Figure 2-6d; austenite nucleation and merging events appearing upon unloading at locations 21-30 and 31-41, respectively, as shown in Figure 2-6e. The shape of spatio-temporal distributions of martensite nucleation/merging and austenite nucleation events are comparable but different from the distribution of austenite merging events as illustrated in Figure 2-7. The austenite merging event in Figure 2-7d is more diffused in time compared to other events in Figure 2-7a-c. It features a characteristic elliptical shape with a major axis aligned with the time-axis as shown by contour lines of heat sources 31-41 in Figure 2-6e. This was found to be characteristic of all austenite merging events. In a sharp contrast, the spatio-temporal color maps of other events in Figure 2-7a-c feature rather circular shapes as underlined by contour lines of heat sources 1-30 in Figure 2-6d, e.

For the statistical treatment of individual events, horizontal and vertical cross-sections through the maxima of spatio-temporal distributions were considered as illustrated in Figure 2-7a. The horizontal cross-sections reflecting the temporal distributions of heat sources were averaged for all events of the same type and plotted in Figure 2-8a, where standard deviations of their maxima are also shown. The comparison of temporal distributions in Figure 2-8a confirms that the austenite merging events are more spread in time compared to other types. To characterize the localized events, averages and standard deviations of FWHM (Full Width at Half Maximum) of temporal distributions were evaluated in Figure 2-8b for individual types of localized heat sources. It shows that the FWHM of the austenite merging events is twice as large compared to other events.

The vertical cross-sections of localized heat effects were used to evaluate the average spatial distributions and standard deviations at their maxima as plotted in Figure 2-8d. The comparison of spatial distributions in Figure 2-8d shows no substantial difference in the size and shape of heat source events, which is confirmed by Figure 2-8e comparing averages and standard deviations of the FWHM evaluated on spatial distributions of individual types of events. Considering the conical-shaped martensite band front in NiTi wires reported in [35], Figure 2-8f plausibly explains the shape of spatial distributions by suggesting cross-sectional geometries of transforming volumes along the wire axis giving rise to the localized heat sources. In fact, two types of cross-sectional geometries may be formed by two adjacent conical interfaces: either a concave shape in the case of martensite nucleation and austenite merging (see MNE and AME in Figure 2-8f) or a lenticular shape in the case of martensite merging and austenite nucleation (see MME and ANE in Figure 2-8f). Localized heat sources of both geometries are indeed spatially most intensive in the center of transforming volumes and tend to vanish towards both interfaces thus giving rise to a Gaussian type of spatial distributions. The magnitudes of spatial distributions are, however, different similarly to temporal distributions shown in Figure 2-8a.

To evaluate *heat*, time integration of the heat sources was performed. Note that in agreement with the used heat source units ($K.s^{-1}$), the heat intensities are evaluated in Kelvin thus expressing temperature changes that the heat sources would cause to the specimen under adiabatic conditions. Figure 2-8c shows the average values and standard deviations of intensities for all types of localized events (red and blue indicators) and for the weak heat sources WHS 1-4 (black indicators) identified in four-time windows shown in Figure 2-6g. The intensities are proportional to the magnitudes of heat sources and the duration of their activities and, therefore, the weak heat sources released a non-negligible amount of heat compared to localized heat sources as they were active for considerably longer times. Figure 2-8c shows that the intensities of localized heat sources active during loading (martensite nucleation and merging) are on average higher than those active upon unloading (austenite nucleation and merging). On the one hand, this may be explained by different latent heats associated with the forward and reverse transformations as observed by HSR [44] and DSC measurement [162]. On the other hand, in the case of mechanically driven martensitic transformation, this difference can be due to the intrinsic dissipation accompanying the forward and reverse martensitic transformation under stress. As the intrinsic dissipation is always positive, it increases the amount of heat generated upon loading but decreases the amount of heat absorbed upon unloading.

Finally, it is interesting to note that the intensities of nucleation and merging events are different as evidenced by the distinct heights of red and blue indicators in Figure 2-8c. The difference is much more pronounced for the reverse transformation, i.e., austenite nucleation and merging, compared to forward transformation, where the average values differ within the standard deviations. These differences suggest that each type of event is accompanied by a release of a different amount of dissipative heat. The dissipative heat cannot be exactly determined from the present experimental data as the values of the latent heat released or absorbed during localized events are unknown. Nevertheless, the dissipative heat can be estimated under the conservative assumption that the dissipative heat is equally distributed between the forward and reverse transformation and that the latent heat of the forward and reverse transformation is constant. In such a case, the latent heat corresponds to the average value of intensities evaluated for the 4 types of events. Such estimated latent heat is plotted with a horizontal dashed line Figure 2-8c. The dissipative heats associated with the 4 types of events are then the differences denoted by black hatched bars in Figure 2-8c. The austenite merging events are associated with a twice as large amount of dissipative heat compared to austenite nucleation events.

Note that the comparison of dissipative heat associated to forward and reverse martensitic transformations cannot be reliably performed here as the value of the latent heat was estimated only. Nevertheless, this uncertainty does not affect the relative comparisons between nucleation and merging events of either forward or reverse martensitic transformation. The same applies to the evaluation of an average relative intrinsic dissipation associated with the localized events, which was evaluated to be 25% of the estimated latent heat by averaging relative intrinsic dissipation of individual events.

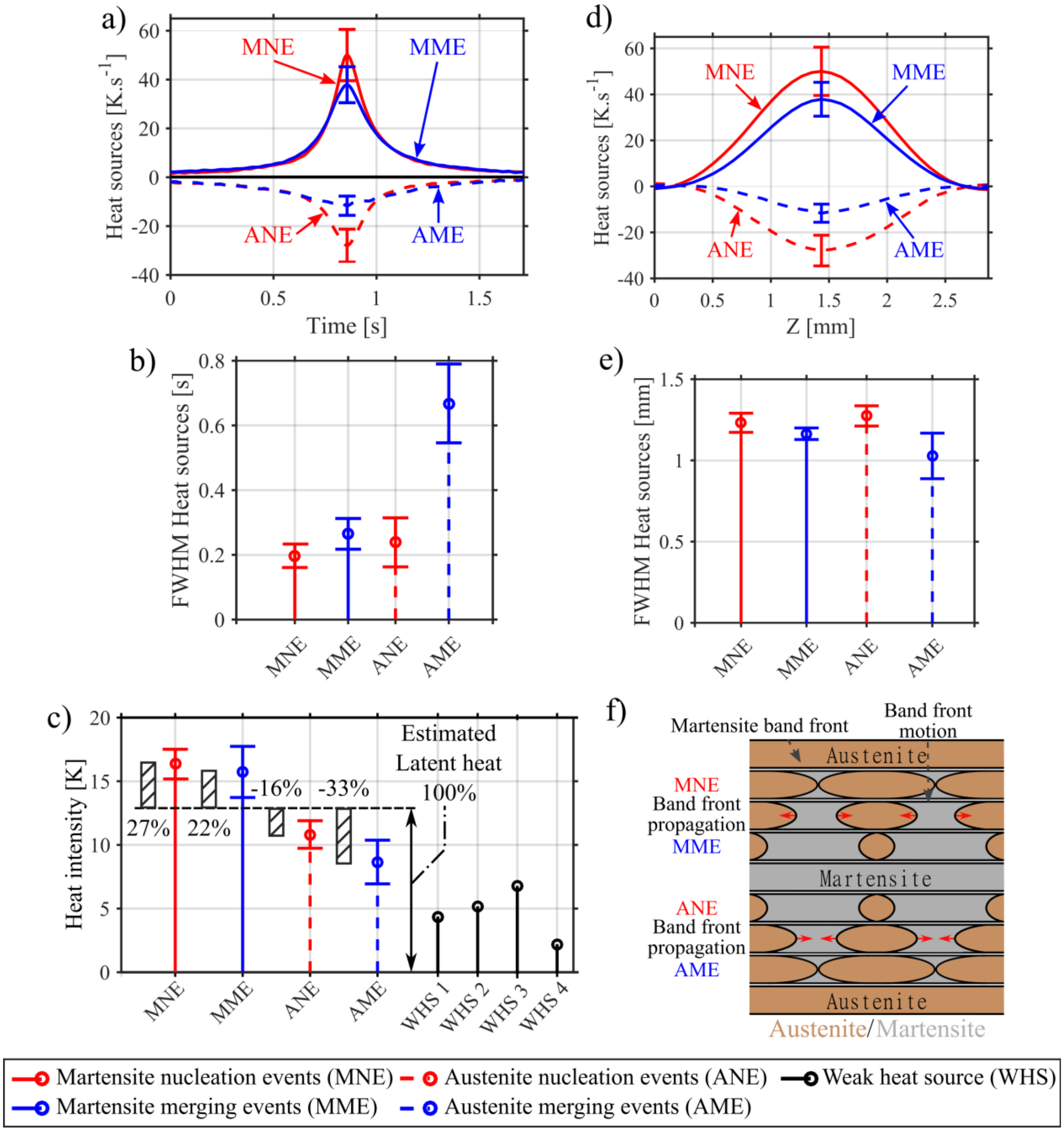

Figure 2-8 : Analyze of localized calorific events: **a), d)** averaged heat sources for each of the four types of localized events as a function of time and space, respectively. Standard deviations are also indicated at the maximum intensities; **b), e)** temporal and spatial Full Widths at Half Maxima (FWHM) of the localized heat sources, respectively; **c)** time integral distributions of the localized (from Figure 2-8a) and weak heat sources (from Figure 2-6g). The black dashed line represents the magnitude of the latent heat estimated as the average intensity. Hashed bars represent estimates of intrinsic dissipation; **f)** scheme of the progress of the localized transformation in the wire in a form of nose cone-shaped martensite band fronts [35] appearing/propagating/disappearing during loading and unloading. Red arrows denote the direction of the front motion.

### 2.6.4 Summary of results

The results can be summarized as follows:

1. The forward martensitic transformation during tensile loading proceeds in two stages. In the first stage, martensite bands nucleate sequentially at multiple equidistant locations along the wire and propagate along the wire. The series of nucleation events, however, gives rise to quasi-homogeneous heating of the volume of the wire between the nucleation sites. The temperature increasing in this volume causes a temporary transformation arrest during which the external stress required to drive the transformation increases. In the second stage, the transformation is completed by sequence of merging events in which two martensite band fronts propagating from the neighboring nucleation sites merge and the austenite disappears.
2. The series of nucleation and merging events are clearly evidenced by the appearance of the localized heat sources and the increase of the macroscopic strain rate.
3. Reverse martensitic transformation during unloading proceeds analogically to forward transformation but the heat bursts are negative.
4. The method allowed for detailed statistical analysis of the observed localized heat sources with respect to the type of events giving the following results.
    a. The integral intensity of localized heat sources corresponding to nucleation events is higher compared to the merging events.
    b. The integral intensity of localized heat sources related to forward martensitic transformation is higher compared to that of reverse transformation.
    c. The austenite merging events corresponding to the reverse transformation are more spread in time compared to other events.
    d. The observed heat sources correspond to the sum of latent heat due to martensitic transformation and intrinsic dissipation accompanying the progress of the transformation. The intrinsic dissipation associated with the nucleation and merging events is estimated to be ~25% of the released/absorbed latent heat.
    e. The austenite merging events during the reverse transformation are associated with higher intrinsic dissipation compared to preceding austenite nucleation events.
    f. The shape of spatial distributions of the localized heat effects correlates with the conical shape of austenite-martensite interface observed experimentally in Ref. [35].
5. The localized martensitic transformation (from the nucleation to the merging heat bursts) is preceded and followed by weak heat effects (positive during loading and negative during unloading) associated with homogeneously proceeding martensitic transformations that precede and follow the heat bursts. The amounts of heat generated/absorbed by the weak heat sources are two orders of magnitude lower compared to the heat generated/absorbed by the localized martensitic transformation. However, since they last longer, the total amounts of heat generated/absorbed by the weak heat sources correspond to 10–40% of the heat generated/absorbed by the localized martensitic transformation.

## 2.7 Conclusion

Heat sources induced by the deformation processes activated in a trained superelastic nickel-titanium wire subjected to a force-controlled tensile loading-unloading superelastic cycle were analyzed using a heat source reconstruction method. Particular attention was paid to the evaluation of the heat exchanges of the specimen with its environment. In addition, the thermal diffusivity of detwinned martensite was identified and was found to be higher than that of austenite by a factor of 1.3. The latent heat generated/absorbed during the forward/reverse martensitic transformation induced by the force-controlled cycle leads to strong thermomechanical coupling that drives the formation of the spatio-temporal distribution of localized transformation patterns and affects the stress-strain response of the SMA wire. The method allows for tracking the progress of the localized stress-induced martensitic transformation. Sequentially appearing patterns of localized transformation events of four types were identified. Upon loading, the events were associated with nucleations of martensite bands and their subsequent merging. Analogically, the events associated with nucleations of austenite bands and their subsequent merging were identified upon unloading. In addition, weak heat sources observed before and after the heat bursts were associated with the homogeneous martensitic transformation. The intrinsic dissipation heat associated with the nucleation and merging events, which is positive on both loading and unloading, is estimated to be ~25% of the released/absorbed latent heat.

# Chapter 3. Fast characterization of functional fatigue of NiTi SMA wires by IRT and HSR

## 3.1 Introduction

We propose now to apply infrared thermography (**IRT**) and heat source reconstruction (**HSR**) technique to the analysis of the *functional fatigue* of a nickel-titanium (**NiTi**) shape memory alloy (**SMA**) wire, i.e. considering several **SIMT** (stress-induced martensitic transformation) cycles starting from a virgin specimen. The calorific analysis of the first mechanical loading cycles is of prime interest for the understanding of the process of functional fatigue. Indeed, calorific data are complementary to mechanical data and can be also used in the development of thermomechanical constitutive models.

Functional fatigue can be revealed by the macroscopic stress-strain cyclic response of a virgin NiTi specimen: a ratcheting effect (cumulative anelastic deformation at each cycle) is generally evidenced in the first tens of cycles [25,119,163]. During these first cycles, large variations of different macroscopic parameters are observed: residual strain increment, transformation stresses, transformation temperatures, as well as mechanical dissipation per cycle. It should be noted that these changes are most significant during the first few cycles and diminish as the cycling process goes [27,164]. In the literature, the residual deformations during the first cycles are attributed to an incomplete reverse transformation [15] and to plastic deformation processes [59,165].

Calorimetric studies of functional fatigue associated with **TIMT** (temperature-induced martensitic transformation) of NiTi have been reported in Refs [12,26,42]. Regarding the functional fatigue associated with SIMT of NiTi, calorimetric studies have been performed both by thermocouples (Ref [166]) and IRT (Refs [21,30,102,114,119,140]). In this chapter, we propose to perform a calorimetric characterization of the functional fatigue associated with SIMT during fast loading. The benefits of fast loading are:

- Efficient application of the HSR technique — Indeed, the heat exchange terms in the heat diffusion equation are difficult to evaluate (compromise to be found between measurement resolution, spatial resolution and temporal resolution of each term of the heat equation). Tending towards adiabaticity is advantageous for HSR. However, it is important to note that a high loading frequency does not imply an adiabatic character of the evolution of the material specimen: the duration of the test (the number of loading cycles) must be considered.
- Application relevance — Fatigue characterization (in the broad sense) being generally long and costly, it is important to develop "accelerated" approaches. In the case of classical structural fatigue, so-called self-heating methods have been developed. We want to go in the same direction for functional fatigue, with the long-term objective to be able to characterize both functional and structural fatigue in a single measurement. Fast testing also reduces data collected by the IR camera, which accelerates the post-processing.

Therefore, this chapter proposes to apply IRT and HSR to the fast analysis of functional fatigue in a NiTi SMA wire. It is organized as follows:

- Section 3.2 provides some additional information about the context of the study;
- Section 3.3 is a short reminder of the HSR technique. Details of the calculation of the different amounts of energy involved are also detailed;
- Section 3.4 describes the experimental device and the preparation of the tested specimen;
- Section 3.5 shows the obtained temperature and heat source fields;
- Section 3.6 discusses the results of the heterogenous and homogeneous calorific responses of the material specimen.

## 3.2 Context

### 3.2.1 Characterization of functional fatigue by DSC

Calorimetric characterization of NiTi functional fatigue is not a new topic. For example in Ref. [42], the functional fatigue of TIMT was studied by differential scanning calorimetry (DSC) over 100 thermal cycles. A decrease in latent heat (-30%) and critical temperatures (-20 K) were observed during the cycles. After subsequent heating of the specimen (at 623 K), partial restoration of the material was observed: a partial return was measured for latent heat (-10% from the initial value) and for critical temperatures (-8 K compared to the initial values).

In Ref. [26], calorific responses of several NiTi specimens subjected to cyclic mechanical loading (between 1 and 300 cycles) were analyzed. The different specimens were cut to perform DSC measurements. A change in latent heat of the same order of magnitude as in Ref. [10] was measured: -22%. Besides, transformation temperatures have increased (up 10K). It should be noted that the decrease in latent heat is related to a decrease in transforming volume fraction. This decrease was confirmed by X-ray diffraction measurement of two specimens, a virgin specimen and another one after 200 superelastic cycles: it was found that residual martensite was present in the second specimen. It was hypothesized that the change in critical temperatures is governed by the deformation of the grain boundaries and the fraction of stored martensite. In addition, a linear relationship between the stored martensite fraction and the residual deformation was established. The authors were able to deduce that the plastic phenomena accompanying the phase transformation for the tested specimens are negligible.

### 3.2.2 Characterization by deformation calorimetry

In Ref. [44], it is reported that for certain NiTi alloys (low temperature annealed), DSC measurement does not enable to reveal a phase change. In contrast, the use of IRT and HSR allowed the authors to overcome this problem and estimate the latent heat of the A→M and M→A transformations.

In Ref. [119], IRT and HSR were applied for the in-situ study of the functional fatigue of the SIMT (100 cycles in quasi-isothermal regime). The authors used digital image correlation (DIC) to evaluate the work involved. A thermodynamic model was employed to separate the different sources of heat produced during the propagation of martensitic band fronts (**MBF**s) : latent heat of phase change, stored energy and mechanical dissipation heat. It has been shown that the mechanical dissipation heat in an MBF can reach 10% of the total heat generated by the material. In the same study, the volume fraction of martensite was evaluated. It is reported that the fraction transformed in an MBF reduces significantly along the cycles: from 95% to 60% for the A→M transformation; and from 65% to 25% for the M→A transformation. Changes in thermomechanical behavior are most prominent in the early superelastic cycles. This has been reported in the literature using stress-strain response in Refs [22,25,165], the mechanical dissipation in Refs [19,98,167,168] and by in-situ X-ray diffraction in Ref. [169].

# 3.3 HSR processing

## 3.3.1 Brief reminder

HSR technique applied to wires is based on the following one-dimensional (1D) version of the heat equation [116,119,146,170]:

$$\rho C\left(\frac{d\Theta(z,t)}{dt}+\frac{\Theta(z,t)}{\tau_{1D}\big(\Theta(z,t)\big)}\right)-k\frac{d^2\Theta(z,t)}{dz^2}=s_{\mathrm{int}} \qquad \text{3-1}$$

where:

- z is the coordinate along the specimen axis (z $\in [0;L]$ where $L$ is the gauge length;
- $\Theta(z,t)$ is the temperature variation with respect to the initial temperature profile. In practice, the latter is measured in steady-state right before the start of the mechanical load at $t$ = 0 s. In the case of a hydraulic testing machine, it is generally not homogeneous due to temperature difference between the two grips;
- $\rho$, $C$ and $k$ are the density, the specific heat and the thermal conductivity, respectively. Following values were considered in the present study on NiTi: $\rho$ = 6450 kg.m$^{-3}$, $C$ = 480 J.kg$^{-1}$.K$^{-1}$ and $k$ = 9.6 W.m$^{-1}$.K$^{-1}$;
- $\tau_{1D}$ is a characteristic time of the heat exchanges with ambient air. This quantity was considered as dependent on the temperature difference with ambient temperature, as identified in chapter 2: $\tau_{\mathrm{1D}}(\Theta)=52.1+33.8\exp(\Theta/5.3)$;
- $s_{int}$ is the "internal" heat source. To recall, it is the sum of a mechanical dissipation part ($d_1$ strictly positive) and a thermo-mechanical coupling part ($s_{\mathrm{tmc}}$). The former is associated to irreversible mechanical phenomena (such as plasticity or fatigue damage) occurring in the material, whereas the latter is the sum of the calorific signatures of the thermo-elastic coupling ($s_{\mathrm{te}}$) and the martensitic transformation ($s_{\mathrm{MT}}$). Thus, $s_{\mathrm{int}}=s_{\mathrm{tmc}}+d_1=s_{\mathrm{te}}+s_{\mathrm{MT}}+d_1$.

HSR consists of evaluating the internal heat sources $s_{\mathrm{int}}(z,t)$ using the left-hand side of Eq. 3-1 from the knowledge of the measured temperature changes $\Theta(z,t)$. However, filtering of the latter is required due to measurement noise strongly affecting the calculation of the derivative operators. In the present work, spatio-temporal thermal fields $\Theta(z,t)$ are preliminary filtered using proper orthogonal decomposition (POD) technique as in Ref. [129]. Next, derivative operations are performed by convolution with Gaussian derivative kernels as in Ref. [131]. Extracting the mechanical dissipation $d_1$ from the calculated "total" internal heat sources $s_{\mathrm{int}}$ requires time integration over mechanical cycles, as discussed in the following section.

## 3.3.2 Calculation of work and heat

The specific work $W$ to deform the specimen between two instants $t_1$ and $t_2$ can be expressed as follows:

$$W(t_2 - t_1) = \frac{1}{\rho}\int_{t_1}^{t_2} \sigma(t)\dot{\varepsilon}(t)dt \tag{3-2}$$

where $\sigma$ and $\varepsilon$ are the macroscopic engineering stress and strain, respectively.

We note $cycle\#$ the number of the cycle, $cycle\#$ = 1 corresponding to the cycle carried out on the virgin material. For simplicity, we use the same symbols $t_s$ and $t_f$ for the beginning and the end of any cycle. The specific work for each cycle is therefore written as:

$$W(cycle\#) = \frac{1}{\rho}\int_{t_s}^{t_f} \sigma(t)\dot{\varepsilon}(t)dt \tag{3-3}$$

The specific work during loading and unloading is noted $FMTW(cycle\#)$ and $RMTW(cycle\#)$ respectively. In the following, acronyms **FMTW** and **RMTW** stand for Forward Martensitic Transformation Work and Reverse Martensitic Transformation Work, respectively, although elastic work is obviously involved.

Let us consider load-unload cycles driven in stress with the same stress rate (in absolute value). We have then:

$$FMTW(cycle\#) = \frac{1}{\rho}\int_{t_s}^{t_f/2} \sigma(t)\dot{\varepsilon}(t)dt \tag{3-4}$$

$$RMTW(cycle\#) = W(cycle\#) - FMTW(cycle\#) \tag{3-5}$$

Replacing “W” by “Q” in the above equations, similar equations can be written for calorific quantities considering the spatial integration of the internal heat sources $s_{\text{int}}$ over the gauge length $L$ of the specimen:

$$Q(t_2 - t_1) = \frac{1}{\rho}\int_{t_1}^{t_2} \left[\int_0^L s_{\text{int}}(z,t)dz\right] dt \tag{3-6}$$

$$Q(cycle\#) = \frac{1}{\rho}\int_{t_s}^{t_f} \left[\int_0^L s_{\text{int}}(z,t)dz\right] dt \tag{3-7}$$

$$FMTQ(cycle\#) = \frac{1}{\rho}\int_{t_s}^{t_f/2} \left[\int_0^L s_{\text{int}}(z,t)dz\right] dt \tag{3-8}$$

$$RMTQ(cycle\#) = Q(cycle\#) - FMTQ(cycle\#) \tag{3-9}$$

In the following, another quantity will be displayed: the “local” specific heat produced over each cycle.

$$Q_{\mathrm{loc}}(cycle\#, z) = \frac{1}{\rho}\int_{t_0}^{t_f} s_{\mathrm{int}}(z,t)dt \qquad 3\text{-}10$$

## 3.4 Experimental setup

The material preparation procedure and the test parameters are the same as in the previous chapter (see section 2.3 and Figure 2-1), except for the loading conditions: **20 load-unload cycles at a force rate of ±400 N.s$^{-1}$ from a virgin specimen**. The differences with respect to Chapter 2 are thus:

- the loading rate, which is twenty times higher;
- the state of the NiTi specimen, which is initially virgin.

All other parameters are the same:

- NiTi medical-grade wire, 1.78 mm in diameter, supplied by Fort Wayne Metals in the as-drawn state with final cold work of 40 % and heat-treated by electropulse Joule effect;
- Instron 8872 uniaxial testing machine;
- gauge length $L$ between the jaws equal to 40 mm;
- minimum and maximum stresses equal to 20 MPa and 800 MPa respectively;
- Infratec 8300 MWIR camera equipped with a telephoto (50 mm) lens and a close-up lens (0.3 m), and calibrated for the range [268 K; 333 K].
- the surface of the specimen coated with a high thermal emissivity (0.96) paint;
- the spatial resolution of the temperature profiles equal to 82.6 µm, with spatial averaging in the transverse direction over 14 pixels to improve the thermal measurement (see Figure 3-1-b);
- thermal acquisition frequency set to 350 Hz (temporal resolution of 2.86 ms);
- spatial and temporal resolutions of the heat source maps equal to 743 µm and 25.7 ms respectively.

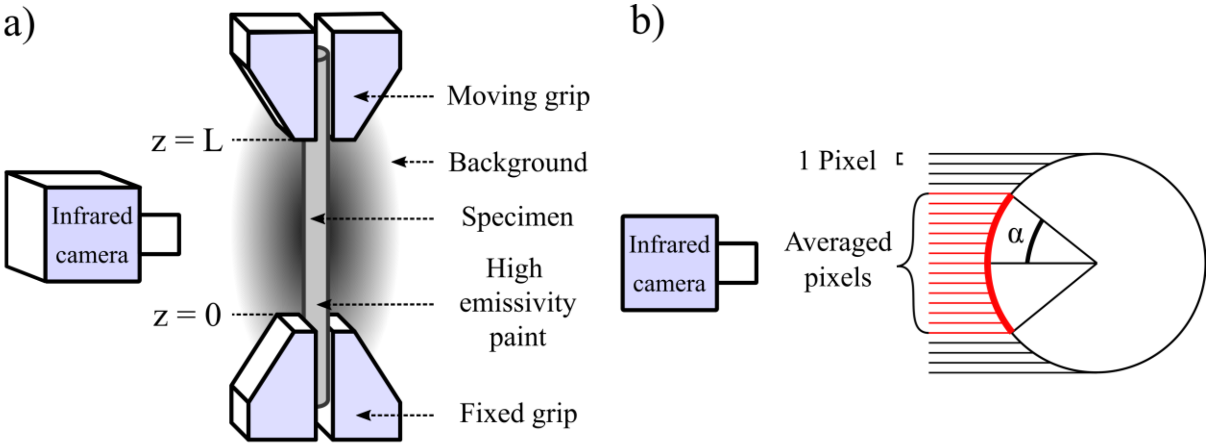

Figure 3-1: Reminder of the experiment.

## 3.5 Results

Results are presented in three sections. Section 3.5.1 provides the macroscopic information as a first step of the analysis. Section 3.5.2 presents the spatio-temporal field of temperature variation $\Theta(z,t)$ and the reconstructed heat source field $s_{\mathrm{int}}(z,t)$. Finally, Section 3.5.3 presents cyclic evolution of different energies defined in Section 3.3.2.

### 3.5.1 Macroscopic observations

Figure 3-2-a shows the macroscopic stress-strain curve along the 20 mechanical cycles. An inclined stress plateau is observed for each cycle, both during loading (A→M transformation) and unloading (M→A transformation). A significant residual strain (2.8%) is visible at the end of the first cycle. This residual deformation is a priori ascribed to the transformation of the wire zone clamped in the jaws. It can be assumed this zone is the first to transform due to the clamping pressure exerted by the jaws and remains transformed when the axial loading is removed. The residual strain increment and the stress plateau level decrease as far as the cycling goes. At the last 10 cycles, only a minor change of material response is observed, which could be interpreted as the stabilization of the material (completion of functional fatigue).

Figure 3-2-b shows the time evolution of the average temperature change $\Theta_{\mathrm{0D}}$ during the 20 cycles followed by the natural return to room temperature. Let us recall that this quantity $\Theta_{\mathrm{0D}}$ is the averaged temperature change over the distance between the jaws of the testing machine:

$$\Theta_{\mathrm{0D}}(t) = \frac{1}{L}\int_0^L \Theta(z,t)\,dz \qquad \text{3-11}$$

During cycle #1, $\Theta_{\mathrm{0D}}$ reached 37 K at the maximum force, before cooling down to a slightly negative value at the end of the unloading. During the cycling process, the maximum value and the peak-to-peak magnitude of $\Theta_{\mathrm{0D}}$ decreased, while the minimum value was reaching a negative value of -8 K at the end of cycle #20. One can see that $\Theta_{\mathrm{0D}}$ is not oscillating around a fixed value, even at the 20th cycle, which means that more cycles were needed for the system to reach steady thermal oscillations. The duration of thermal stabilization during cyclic loading depends on both the mechanical stabilization and the heat transfer conditions with the environment (ambient air and test machine jaws), as discussed in Ref. [47]. Note that the heat exchange conditions with the environment can be evaluated by the stage of natural return to thermal equilibrium after the end of the cyclic loading stage.

Figure 3-2-c emphasizes strong thermomechanical coupling in NiTi by showing the stress evolution as a function of $\Theta_{\mathrm{0D}}$. The inclination of the stress plateau is ascribed to the significantly non-isothermal response associated with SIMT. The decrease in critical transformation stresses during cyclic loading can be partially attributed to the specimen temperature. Indeed, while the stress plateau appears in the first cycle at a temperature higher than the room temperature it appears at a temperature lower than the room temperature in cycle 20. One can also note for example that the important temperature variations during the 20th cycle extend over a longer duration than during the 1st cycle (see the in-set graph in Figure 3-2-b showing the evolution of the temperature at cycles #1 and #20).

Figure 3–2-d shows a schematic for evaluation of the critical transformation stresses and the maximum (**Hmax**) and minimal (**Hmin**) stress hysteresis. Stress values were measured for each cycle by defining the beginning and the ends of the A→M et M→A transformation plateaus by the tangent method. We distinguished between martensitic nucleation and merging events (**MNE** and **MME** respectively) and austenitic nucleation and merging events (**ANE** and **AME** respectively). Figure 3–2-e shows the decrease in these critical stresses along the 20 cycles, without reaching stabilization. Figure 3–2-f shows that the minimum hysteresis decreases rapidly during the first 5 cycles before stabilizing. The maximum hysteresis appears to take more cycles to stabilize.

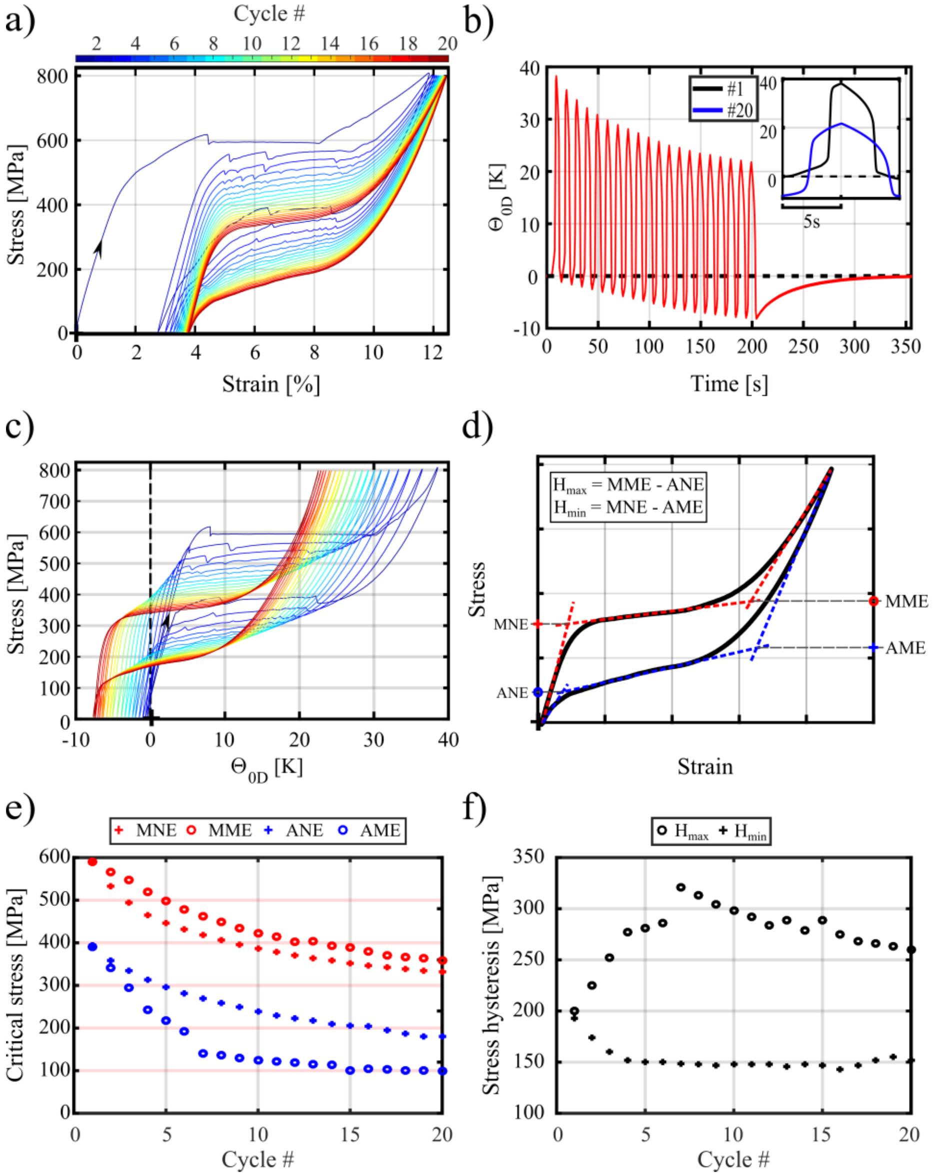

Figure 3-2: Macroscopic response: **a)** stress *vs.* strain, **b)** time evolution of the mean temperature change $\Theta_{0D}$ and focus on the 1st and 20th cycles, **c)** stress *vs.* $\Theta_{0D}$, **d)** scheme for evaluation of the critical transformation stresses and the maximum ($H_{max}$) and minimal ($H_{min}$) stress hysteresis. MNE, MME, ANE and AME correspond to events of martensitic nucleation, martensitic merging, austenitic nucleation and merging nucleation, respectively, **e)** evolution of the critical transformation stresses, **f)** evolution of $H_{max}$ and $H_{min}$.

Figure 3-3-a shows the evolution of the averaged internal heat sources (noted $s_{int\_0D}$) as a function of stress.

$s_{int\_0D}$ is calculated as follows :

$$s_{int\,0D}(t) = \frac{1}{L}\int_0^L s_{int}(z,t)\,dz \qquad 3\text{-}12$$

We preferred this approach instead of directly using the 0D approach in order to reduce potential errors of the macroscopic approach, as it has been demonstrated experimentally and numerically in Ref. [126]. Classically, the heat sources obtained by DSC are presented as a function of temperature. In the context of deformation calorimetry, we propose to plot the heat sources as a function of macroscopic stress. As the stress increases (direct transformation), the heat sources are positive, and the peak maxima are approximately halfway through the stress plateau. Decreasing temperature along the cycles results in decreasing transformation stresses, and thus a shift of the heat peaks to the left on the diagram. It is noted that the magnitude of the peaks decreases by about 2.5 times between the 1st and 20th cycles, and the width appears to increase.

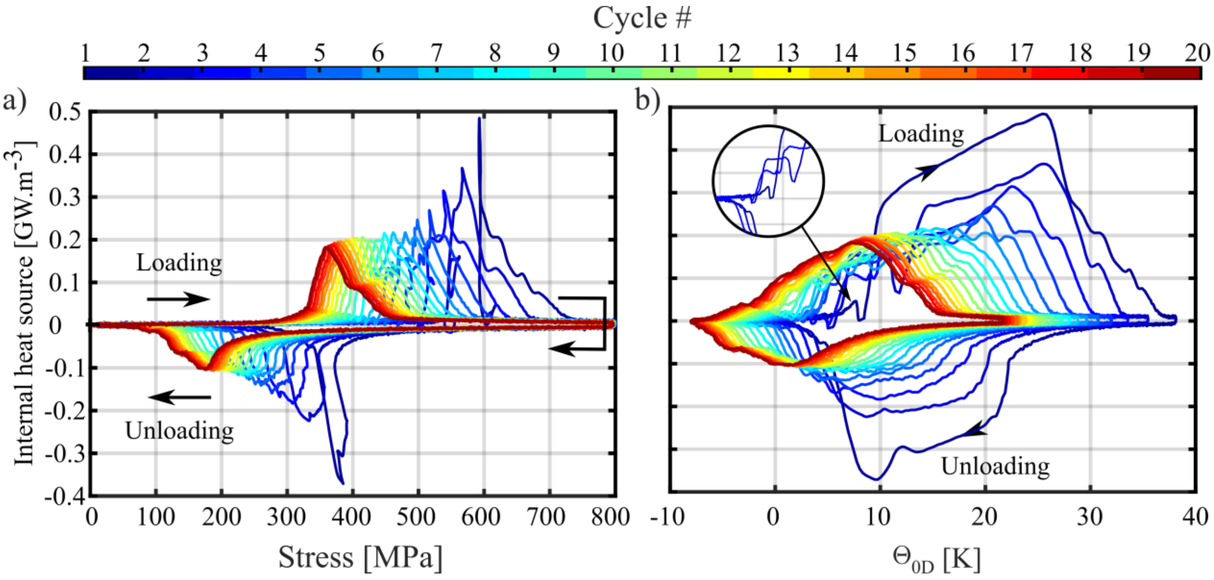

Figure 3-3: Macroscopic heat source response: **a)** mean internal heat source $s_{int\,0D}$ vs. stress, **b)** mean internal heat source $s_{int\,0D}$ vs. mean temperature variation $\Theta_{0D}$.

Figure 3-3-b shows the evolution of the mean internal heat sources as a function of mean temperature variation (noted $\Theta_{0D}$). The peaks shift to lower temperatures. During loading at the 1st mechanical loading, the (slightly positive) heat sources drop suddenly to 0 W.m$^{-3}$ at $\Theta = 7.5$ K (see close-up in the figure). This zero value appears at the small stress drop when entering the stress plateau (see Figure 3-2-a). These heat source drops are also observed at the beginning of the stress plateau during the 2nd and 3rd cycles**.** Figure 3-2-b also shows that the temperature hysteresis associated with MT decreases during the cycling process: it is around 37 K at the 1st cycle and decreases to 30 K at the 20th cycle. Due to the complex nature of NiTi stabilization, deconvolution of functional fatigue effects and temperature dependence of critical transformation stresses cannot be done without thermodynamic modeling.

### 3.5.2 Spatio-temporal observations

Figure 3-4 shows the « 1D+time » spatial-temporal fields of temperature variation at cycles #1, #5, #10 et #20 The maximum local temperature variation is 42 K (during the 1st cycle). The thermal responses within each cycle show three main time intervals (green→red/orange→ green). Spatial heterogeneities are visible at their transitions that are shown in Figure 3-5. Additional 1D spatio-temporal temperature and heat source fields are presented in Appendix B.

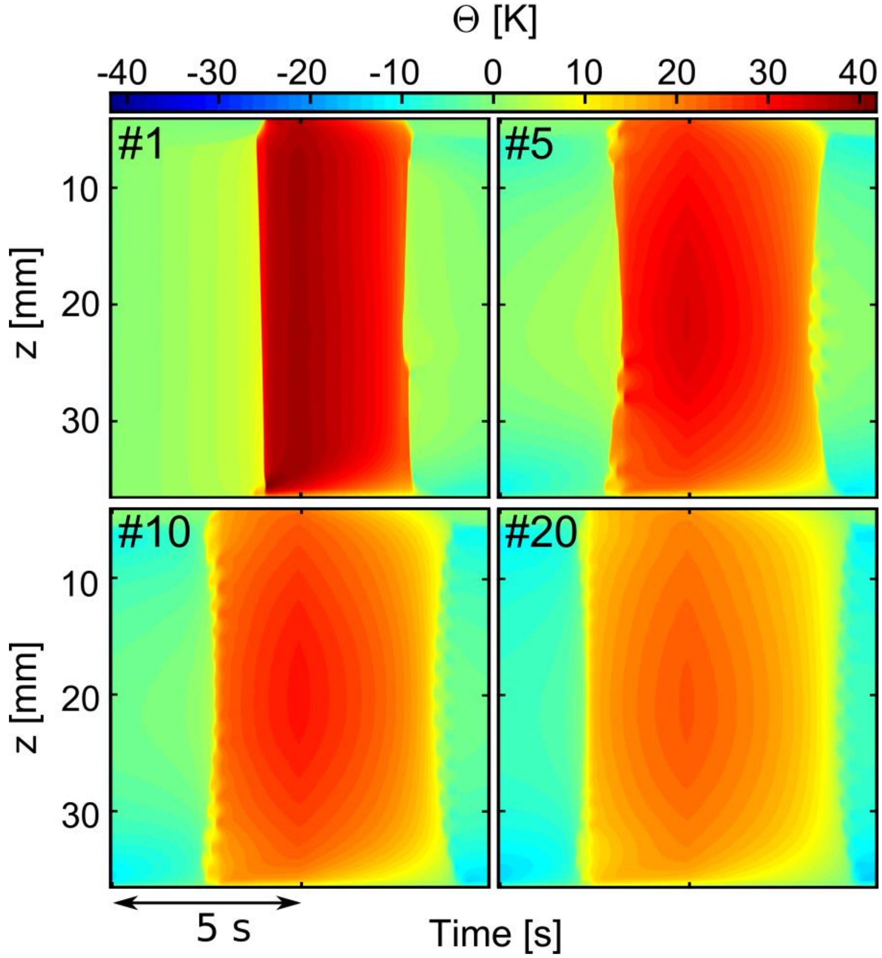

Figure 3-4: 1D Spatio-temporal field of temperature change during cycles #1, #2, #5, #10 and #20.

Figure 3-5 presents the spatio-temporal fields of temperature change and heat sources focused on short durations of transformation during cycles #1, #2, #5, #10 and #20. As positive/negative heat sources reflect the forward/reverse transformation events, these could be denoted using the following acronyms:

- **FMT** and **RMT** denote *Forward Martensitic Transformation* (upon loading) and *Reverse Martensitic Transformation* (upon unloading), respectively;
- **MBF**, **FMBF** and **RMBF** mean *Martensite Band Front*, *Forward Martensite Band Front* and *Reverse Martensite Band*, respectively;
- Let us recall that **MME**, **AME**, **MNE** and **ANE** mean *Martensite Merging Event*, *Austenite Merging event*, *Martensite Nucleation Events* and *Austenite Nucleation events*, respectively.

Temperature fields are displayed in the left-hand side of Figure 3-5 for information. Comments on the corresponding heat sources on right-hand side maps are here separated into two groups:

## For the FMT:

- At cycle #1, one MBF starts from the upper jaw of the testing machine and travels over the whole specimen gauge length (see FMBF in the map).
- In cycle #2, a first MBF appears from the bottom jaw. It is then inhibited and replaced by another moving one starting at the upper jaw at about 13.6 s: it merges with the first MBF at $z$ = 28.5 mm at about 13.8 s (see MME in the map);
- In cycle #5, one MBF first propagates shortly from the bottom jaw. It continues at a lower speed (i.e. with lower heat source intensity, see the yellow band) while a second MBF propagates from the upper jaw. This second MBF briefly stops when a martensite merging occurs (see MME in the map). Other events then occur, in particular two final simultaneous MNEs;
- In cycles #10 and #20, MBFs are not observed. Numerous MNEs and MMEs are visible. They appear in two stages. In the first stage, two MNE “waves” alternatively propagate from the two jaws. In a second stage, several MMEs occur nearly simultaneously (This phenomenon has not yet been reported to our knowledge);
- A maximum number of 14 nucleations (MNE) and 9 merging (MME) sites in a FMT were counted; see Figure 3-6 for additional comments.

## For the RMT:

- In cycle #1, RMT starts with the appearance of an ANE at about $z$ = 22.5 mm. From there, one high-magnitude RMBF then propagates in the direction of the upper jaw, while another propagates slowly (i.e. with a lower intensity, light blue band) towards the bottom jaw. A second high-magnitude RMBF is initiated by an ANE and propagates towards the bottom of the specimen. A final AME completes the RMT of the specimen.
- In cycle #2, a similar pattern of events is observed, except for the addition of 1 ANE and 2 AMEs.
- Cycle #5 is characterized by numerous ANEs. They appear in the form of two “waves” starting from the middle of the specimen (about at $z$ = 23.2 mm) and propagating alternatively. MBFs seem to propagate between some of the nucleation sites (see light blue bands). AMEs are more difficult to identify. Some of them seem to occur quite simultaneously.
- In cycles # 10 and #20, MBFs are not observed, similarly to the corresponding loading stages: numerous ANEs and AMEs are visible, appearing in two stages. First, two ANE “waves” alternatively propagate from $z$ = 21.8 mm. Then, several AMEs occur simultaneously.

See next page

Figure 3-5: Spatio-temporal colormap of temperature variation (left side) and heat source (right side) on short durations of transformation during cycles #1, #2, #5, #10 and #20. Forward and reverse martensitic transformation (FMT and RMT) are distinguished.

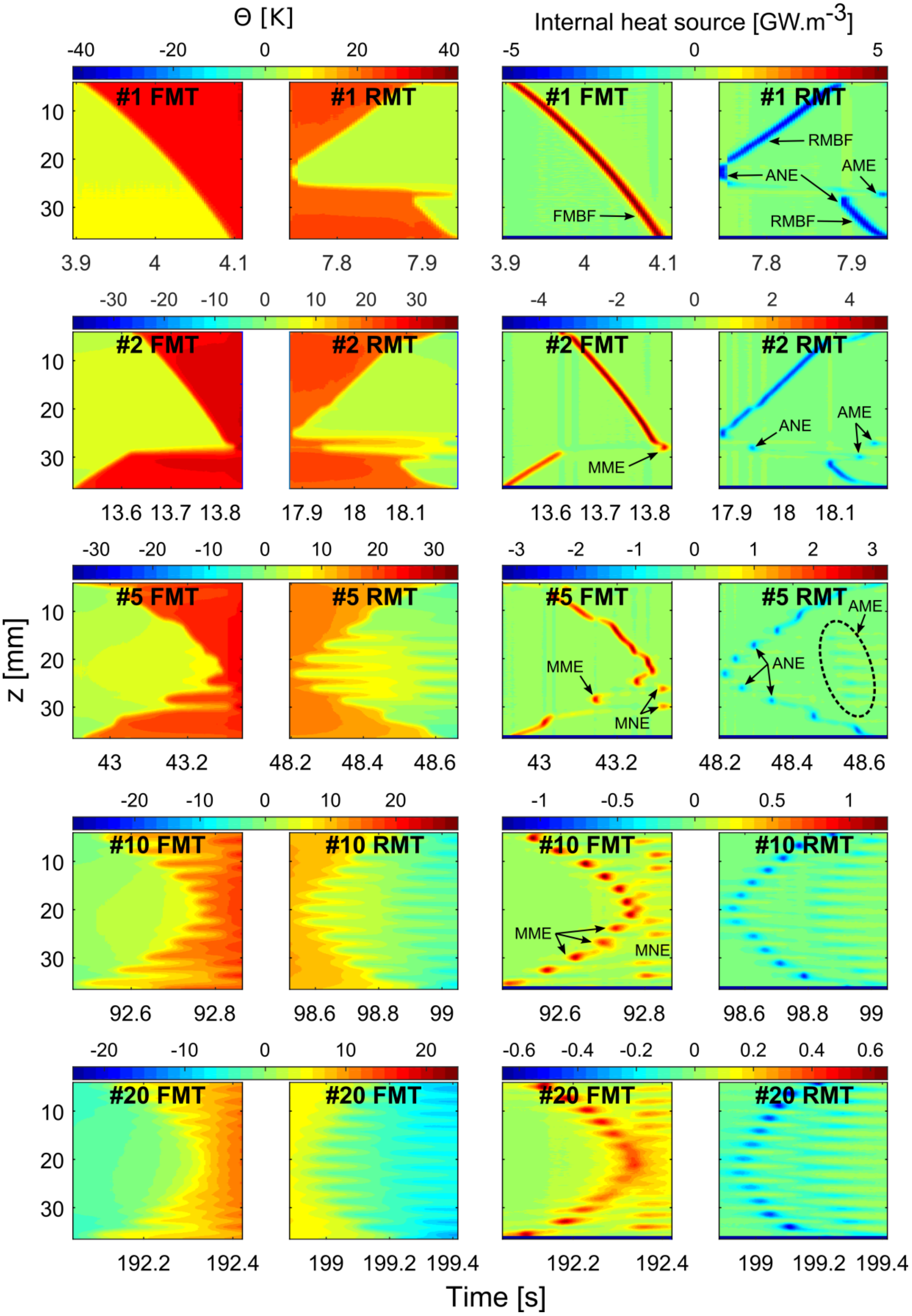
Θ [K]
Internal heat source [GW.m$^{-3}$]
-40 -20 0 20 40
-5 0 5
#1 FMT
#1 RMT
RMBF
ANE
AME
FMBF
3.9 4 4.1 7.8 7.9
-30 -20 -10 0 10 20 30
-4 -2 0 2 4
#2 FMT
#2 RMT
MME
13.6 13.7 13.8 17.9 18 18.1
-30 -20 -10 0 10 20 30
-3 -2 -1 0 1 2 3
#5 FMT
#5 RMT
MNE
43 43.2 48.2 48.4 48.6
-20 -10 0 10 20
-1 -0.5 0 0.5 1
#10 FMT
#10 RMT
92.6 92.8 98.6 98.8 99
-20 -10 0 10 20
-0.6 -0.4 -0.2 0 0.2 0.4 0.6
#20 FMT
#20 RMT
192.2 192.4 199 199.2 199.4
z [mm]
10 20 30
Time [s]

Figure 3-6 presents the number of nucleation and merging sites, as well as the total number of events, during the loading and unloading stages for all cycles. The counting of nucleation and merging sites was carried out with a Matlab segmentation toolbox with a threshold selected manually. It can be noted that the total number of events during the reverse transformation (RMT) is higher than that during the forward transformation (FMT). No threshold was found to properly detect the MNEs appearing at the center of the specimen during FMT. We can also notice that the number of events is globally constant from the 9th cycle, which can be related to mechanical stabilization.

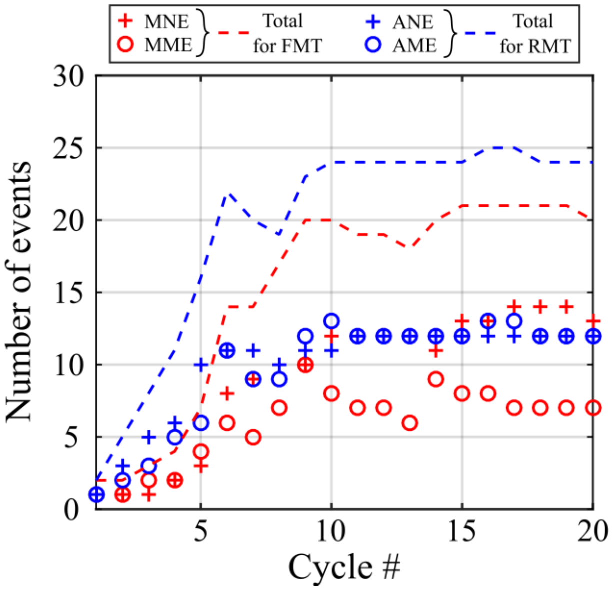

Figure 3-6: Number of events over the cycles.

Some final remarks can be made about the HSR technique in the present analysis. Due to the rapid loading, the effect of heat conduction was small. However, it was not negligible: the weight of the term $-k\ d^2\Theta/dz^2$ was evaluated at a maximum of 15% on the left-hand side of the heat diffusion equation. For information, the term $\rho C\ \Theta/\tau_{1D}$ associated to heat exchanges between the specimen and the ambient air corresponds to 1% at the maximum. Thus, the time derivative $\rho C\ d\Theta/dt$ represents the most important term for the reconstruction of the internal heat sources. Therefore, the heat capacity $\rho C$ is here a prime thermo-physical property for post-processing of thermal data by HSR.

## 3.5.3 Specific energies

### 3.5.3.1 Macroscopic energies

Figure 3-7-a shows the specific work $FMTW(cycle\#)$ and $RMTW(cycle\#)$ and the specific heat $FMTQ(cycle\#)$ and $RMTQ(cycle\#)$ over each loading and unloading stage, respectively: see equations 3-4, 3-5, 3-8 and 3-9 in Section 3.3.2. It must be noted that the RMT energies are presented in absolute value for comparison purposes with FMT energies. As expected, heats are greater than works (due to the latent heat) and forward quantities are greater than reverse ones. The decrease of the four types of energies is associated with functional fatigue.

Figure 3-7-b presents the dissipated work $W(cycle\#)$ and the dissipated heat $Q(cycle\#)$ over the whole cycles: see equations 3-3 and 3-7 in Section 3.3.2. Maximum dissipated specific heat is observed for cycles #2, #3, #4: $Q$ = 1.57 J.g$^{-1}$. The values then decrease and stabilize from the tenth cycle at about 1.15 J.g$^{-1}$. The dissipated specific work during the first cycle tends to be overestimated due to transformation in the jaws of the testing machine (see explanation in section 3.5.1) and cannot be used for material response interpretation. It can be seen then $W$ decreases along the cycles but does not seem to be stabilized at the 20th cycle.

The $FMTQ$ value decreases between the 1st and 20th cycle by 21%. The $RMTQ$ value decreases by 22.2%. These orders of magnitude are in agreement with the decreases in latent heat indicated in Refs [26,41–44,119]. As a reminder, the decrease in latent heat along the cycles can be attributed to martensite storage and accommodation at the grain boundaries.

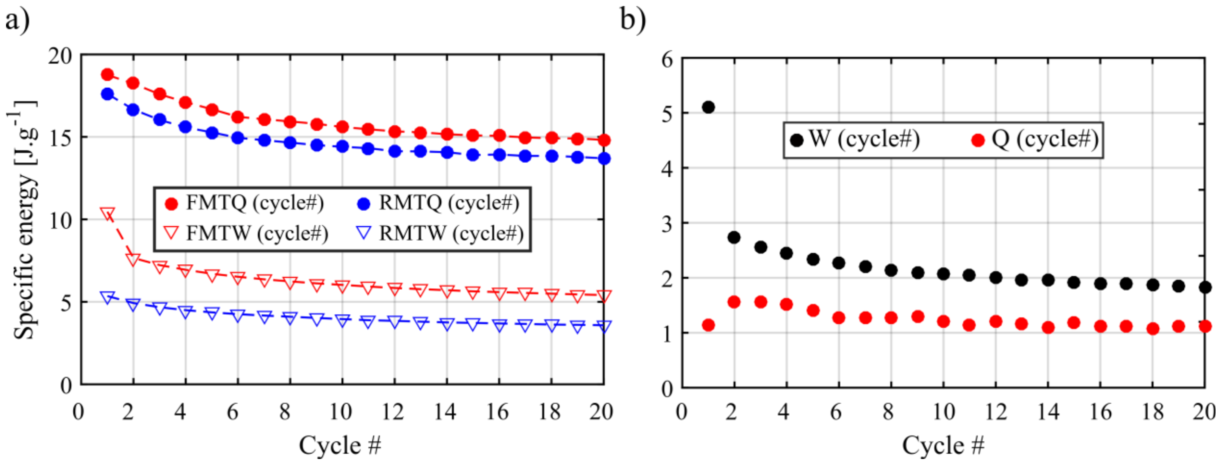

Figure 3-7: Cyclic evolutions of macroscopic specific energies in terms of **a)** work(W) and heat(Q) during forward(FMT)/reverse(RMT) MT **b)** dissipated heat and mechanical hysteresis over each cycle.

For more information, Figure 3-8 shows the same quantities as in Figure 3-7 as they evolve within the cycles. They are displayed as a function of the stress in the left-hand side column and as a function of time right-hand side column of the figure. This figure shows that:

- During elastic-like early stages of loading in each cycle, the heat produced is greater than the work developed: $Q > W$. This heat is attributed to early MT and associated MT mechanical dissipation;
- Over each cycle, the heat produced is lower than the work (supplied + restored): $Q < W$ which indicates that a portion of mechanical energy was stored in the material in form of microstructure defects and possibly into residual martensite;
- Comments about maximum values have been formulated above in the description of Figure 3-7.

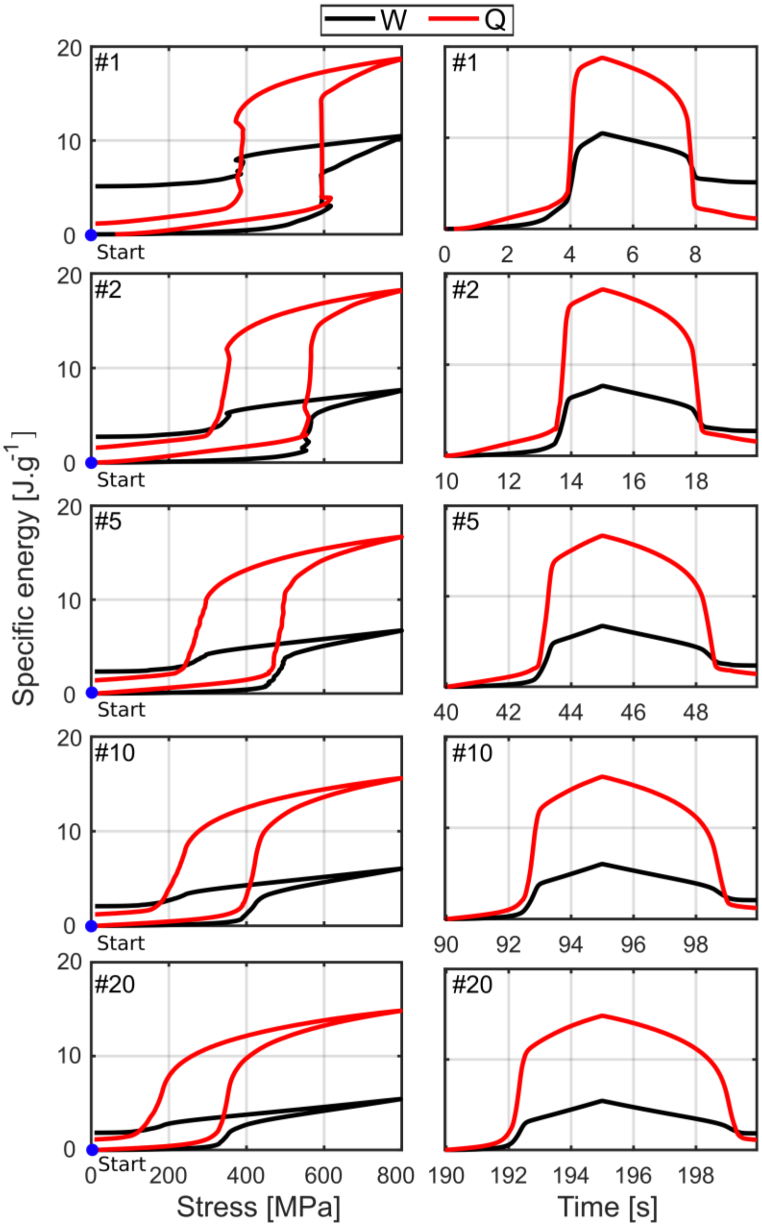

Figure 3-8: Macroscopic specific energies involved within the mechanical cycles. The red and black curves correspond to heat and work, respectively, from the beginning of the cycle.

#### 3.5.3.2 Energies associated with homogeneous deformation processes

Prior to and after localized MT events homogeneous deformation processes take place. Besides elasticity, homogeneous-like MT precedes localized events [170]. Figure 3-9-a shows the specific heat when the heat source response is homogeneous (and weak), distinguishing *prior* and *after* the occurrence of localized heat events. The same acronyms are used here as in Chapter 2: WHS1 and WHS2 during loading (FMT), WHS3 and WHS4 during unloading (RMT). See Figure 2-6-g in Chapter 2 to recall these phenomena. Let us note that weak heat sources (in W.m$^{-3}$) lead integrally to large heat energies (in J.m$^{-3}$) and then converted to specific heat (in J.g$^{-1}$) by dividing by the density.

Some factual remarks can be made about these results:

- Among the four quantities, WHS3 and WHS4 (prior and after RMT) are in magnitude the largest and smallest values respectively;
- WHS1 (prior FMT) decreases strongly from 3.90 J.g$^{-1}$ to about 2.15 J.g$^{-1}$ during the first 5 cycles, then stabilizes. WHS2 (after FMT) increases sharply during the first 10 cycles, from a value of 3.7 J.g$^{-1}$ to 5.8 J.g$^{-1}$;
- WHS3 is relatively constant along with the cycles. Values increase from -7.0 J.g$^{-1}$ to -7.5 J.g$^{-1}$ between the cycle #1 and cycle #20;
- WHS4 decreases continuously over the cycles, going from -1.7 J.g$^{-1}$ to -0.4 J.g$^{-1}$ between cycle #1 and cycle #20.

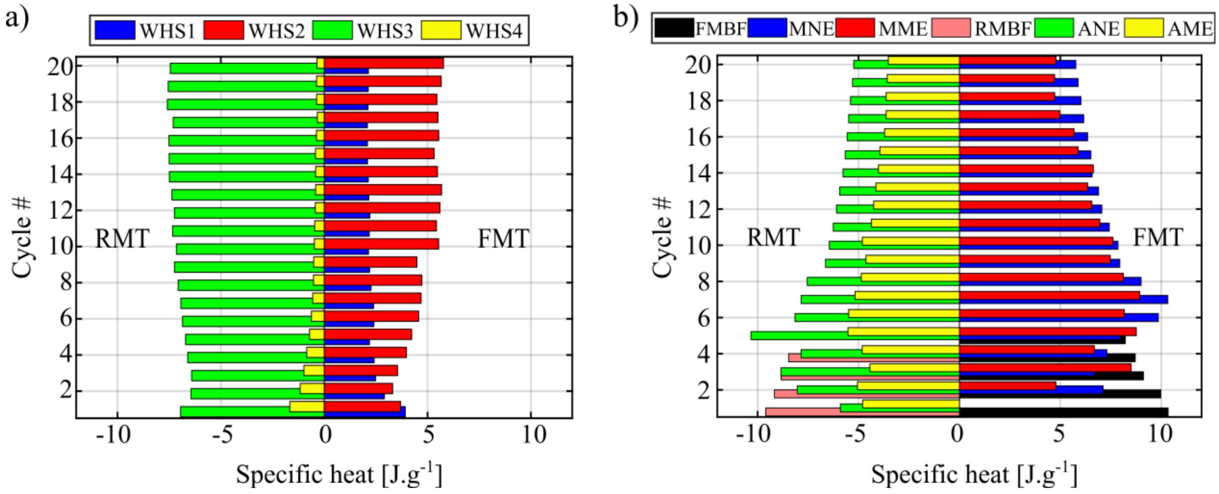

Figure 3-9: Mean specific heats: **a)** for homogeneous calorific events, **b)** for heterogeneous calorific events. See text for the meaning of the acronyms.

### 3.5.3.3 Energies associated with localized deformation events

Figure 3-9-b shows the average specific energies associated with localized heat events. We distinguished the events using the same acronyms as previously:

- during loading: propagation (FMBF), nucleation (MNE), and merging (MME) events;
- during the unloading: propagation (RMBF), nucleation (ANE), and merging (AME) events.

The MBF heat estimation was carried out by integrating MBF heat sources fitted with Gaussian function in every pixel as illustrated in Appendix C. The nucleation and merging sites heat estimation was carried out by integrating spatio-temporal zones, being of 9 standard deviation in time and space around the peak intensity of the associated site as illustrated in Appendix C.

Some remarks can be made about the results:

- during loading — propagation (FMBFs) was only observed during cycles #1 to #5. The corresponding specific heats are between 10.3 J.g$^{-1}$ and 8.2 J.g$^{-1}$, the maximum corresponding to the first cycle. The values for MNEs are between 7.1 J.g$^{-1}$ and 10.3 J.g$^{-1}$, the maximum corresponding to cycle #7. Those for MMEs are between 4.8 J.g$^{-1}$ and 9 J.g$^{-1}$, the maximum also corresponding to cycle #7;

- during unloading — propagation (RMBFs) was only observed during cycles #1 to #4. The corresponding specific heats are between -9.6 J.g$^{-1}$ and -8.5 J.g$^{-1}$ where the maximum (in absolute value) corresponds to the first cycle. The values for ANEs are between -5.2 J.g$^{-1}$ and -10.3 J.g$^{-1}$, the maximum magnitude corresponding to cycle #5. Those for AMEs are between -3.5 J.g$^{-1}$ and -5.5 J.g$^{-1}$, the maximum magnitude corresponding also to cycles #5 and #6.

#### 3.5.3.4 Comparaison between energies of homogeneous and localized processes

Figure 3-10 shows the proportions of the mean energies associated with the homogeneous and heterogeneous deformation processes. The percentages for loading are denoted by **WHS FMT** and **Local FMT**, respectively. The percentages for the unloading are denoted by **WHS RMT** and **Local RMT**, respectively. The evolution of the homogeneous calorific events proceeds in two stages. During the mechanical stabilization stage (cycles #1 to #9), WHS FMT is globally constant (between 40 and 45%). Between cycles #10 to #20, WHS FMT increases linearly from 45 to 60%. We deduce that the "delocalization" of the MT is the result of the stabilization of the material's microstructure that has been reported to evolve during the stabilization of superelastic response. The same qualitative comments can be made for the unloading. We can hypothesize that the continuation of the cycles would lead to a completely homogeneous MT.

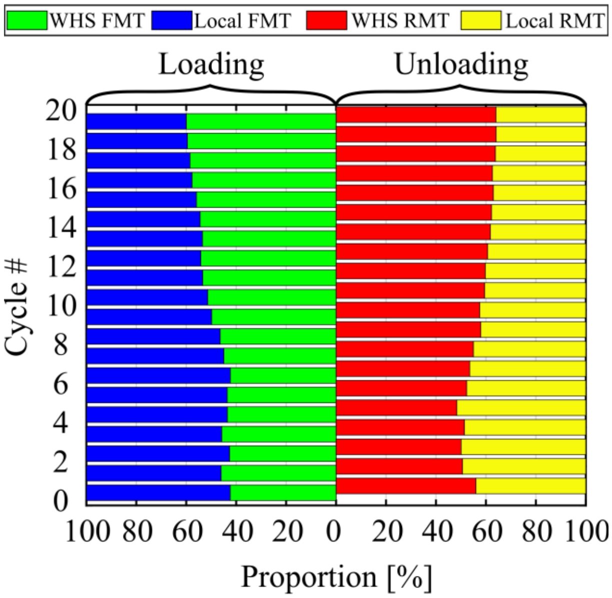

Figure 3-10: Proportions of mean energies associated with homogeneous and heterogeneous deformation processes.

#### 3.5.3.5 Spatial distribution of heat produced over a whole cycle

The distribution of specific heat $Q_{\mathrm{loc}}(cycle\#, z)$ is displayed in Figure 3-11 over cycles #1, #2, #5, #10 and #20 (see Equation 3-10 in Section 3.3.2). We observe that the distributions are strongly heterogeneous.

- For cycle #1, the distribution shows a localized peak at $z = 29$ mm. This corresponds to the austenite merging event (AME) in Figure 3-5 “#1 RMT”;
- For cycle #2, the distribution presents two peaks located at $z = 29$ mm and 32.5 mm. They correspond to the two AMEs in Figure 3-5 “#2 RMT”;
- For cycle #5, the distribution shows seven localized peaks, which can be mapped to the ANEs (excluding events at the two ends). The same comments can be made for cycles #10 and #20.

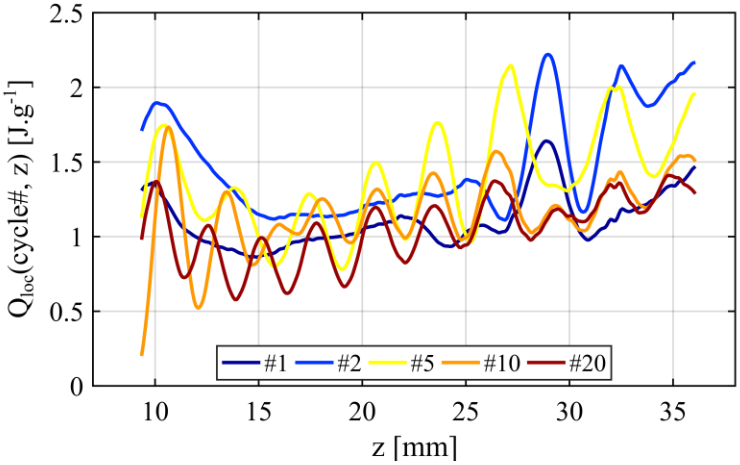

Figure 3-11: Spatial distribution of specific heat produced over cycles #1, #2, #5, #10 and #20.

## 3.6 Discussion

A test was carried out on a virgin NiTi wire under cyclic mechanical loading-unloading in force control at room temperature (295 K). MT was monitored using IRT and processed by HSR. The high loading frequency enabled us to reveal the thermomechanical couplings within the specimen.

A large temperature change of about 42 K (Figure 3-4) was observed during the 1st loading which may be due to the mechanical dissipation associated with MT. At the last cycles, the peak-to-peak temperature change was about 30 K, when the material showed a stabilized mechanical response. These observations confirm that NiTi is an excellent candidate for elastocaloric systems. The cooling capacity upon the reverse transformation can be observed and was 2 to 3 times higher than those measured in studies dedicated to this type of application [54,171]. In our experiment, larger temperature variations were reached due to an assumed nearly complete transformation, contrary to the studies in Refs [54,171] in which transformation was partial. To recall in adiabatic conditions, the maximal temperature variations $\Delta T_{\max}$ is the ratio of the phase transformation latent heat and the specific heat capacity. It is probably difficult to reach these temperature changes in a solid-state refrigeration system as heat has to be evacuated.

The decreasing temperature variations along the cycles modified the critical stresses of the forward and reverse phase transformations (Figure 3-2-a). Thermal stabilization was not achieved in 20 cycles (Figure 3-3-a and b) while mechanical stabilization was observed in about 9 or 10 cycles (Figure 3-2-a). It was noted in Refs [47,50] that for similar fast mechanical loading, thermal stabilization can occur beyond 100 cycles. It can be noted that the duration to reach thermal stabilization actually depends on the characteristic time

$\tau_{0\mathrm{D}}$. Thermal stabilization can be considered as reached from about 4 or 5 times $\tau_{0\mathrm{D}}$ when the mean heat source release is *constant*. With $\tau_{0\mathrm{D}} \approx 35.5$ s in the present study, it gives about 150 s, to be compared with the 200 s duration of the cyclic loading applied. As thermal stabilization was not reached in 200 s, it means that calorific response was not stabilized.

The heat source evolution within transformation mechanical cycles was presented (see Figure 3-3), as mechanical version of DSC curves. The mechanical DSC curves might be considered as a characterization of elastocaloric performance. Conversely to DSC response for TIMT, the magnitude of the heat source peaks decreases by about 2.5 between the 1st and the 20th cycle while the peak widths increase. The observed localized calorific events allowed the detection of different MT mechanisms: martensitic band fronts, nucleation sites and merging sites. These events were quantitatively visible in the 1D spatio-temporal thermal response (Figure 3-4) but heat source fields enabled a more precise and quantitative analysis (Figure 3-5). During the mechanical stabilization stage (in about ten cycles), the progressive disappearance of MBFs made room for the initiation of a large number of nucleation and merging sites (see Figure 3-6). During the stabilized mechanical stage, the distinction of local events became more delicate as MT became more and more homogenized (see for instance cycle #20 in Figure 3-4 and Figure 3-5).

We found by integrating the heat sources (Figure 3-7-a) that the specific heat during FMT was higher than that during RMT. This discrepancy is possibly related to different origins: 1) mechanical dissipation and 2) stored martensite.

Specific heat and specific work over a whole cycle demonstrated that only a portion of the work was converted into heat (Figure 3-7-b). The evolution of the heat dissipated within a cycle reached a maximum of 1.58 $\mathrm{J.g^{-1}}$ at cycles #2, #3, #4 and then tended to stabilize at about 1.15 $\mathrm{J.g^{-1}}$. Conversely, the work dissipated over a whole cycle decreased from 2.75 $\mathrm{J.g^{-1}}$ from the 2nd cycle to reach 1.83 $\mathrm{J.g^{-1}}$ at the 20th. The discrepancy between heat and work indicates that a portion of the work is not released in form of heat and was stored in the microstructure as residual martensite, defects, and deformation energy.

The MT “delocalization” was energetically analyzed (Figure 3-9 and Figure 3-10). Thanks to HSR, a homogeneous MT was clearly evidenced and proved as a significant and comparable heterogeneous MT. As a matter of fact, heat related to the homogeneous deformation process tended to increase after the mechanical stabilization. Indeed, while the portion of homogeneous heat response was 40 % at the 1st cycle, it reached 60 % at the 20th one.

The spatial periodic pattern of thermomechanical response was evidenced in NiTi wires by simulation in Ref. [31] and experimentally in Ref. [170]. Lately, in Ref. [172], simulation has been developed evidencing three ranges of mechanical loading strain-rates showing three different deformation modes in NiTi strips. At low strain-rate, nucleation, merging and MBF were observed. At mid strain-rate, square periodic pattern sites were observed. Finally, at a high strain-rate, MT occurred in a delocalized manner as it can be extrapolated from the present study.

Finally, the distribution of the spatial heat dissipated over a whole cycle was shown (Figure 3-11). We have observed that a maximum was obtained at cycle #5 and the location of the maximum values were corresponding to the nucleation sites of the RMT.

## 3.7 Summary and conclusions

The results of the present analysis of the calorific response over twenty mechanical cycles at a high force rate applied on a virgin NiTi specimen can be summarized as follows:

1. HSR has proved his efficiency as a fast calorimetric technique thanks to a “quite” adiabatic regime. In practice, the weight of the conduction and convection contributions were evaluated to a maximum of 15% and 1% respectively in the quantification of the heat source. Indeed, tests with large and fast temperature variation lead to a good signal-to-noise ratio of the different terms of the heat diffusion equation, which allows a more reliable heat source reconstruction than those under slower mechanical loading. HSR in combination with fast loading thus seems like an ideal method to assess the elastocaloric efficiency of SMAs.
2. In the present study, large temperature variations of about 42 K were observed at the first cycle. When the material was mechanically stabilized (after 10 mechanical cycles), the temperature change was about 30 K prior to reaching the thermal stabilization that was not reached even after 20 cycles applied in total. These temperature changes confirm that NiTi is an excellent candidate for elastocaloric systems.
3. 1D spatio-temporal fields of temperature variations and of heat sources showed the localized occurrence of MT in the form of martensite band fronts, nucleation sites and merging sites, followed by a progressive delocalization of MT.
4. The magnitude of the heat released during the FMT was greater than the one absorbed during the RMT, this asymmetry is assumed to be attributed to the stored martensite and work dissipated in form of heat.
5. The evaluation of the heat of the heterogeneous and homogeneous events evidenced that MT tends to be delocalized after the mechanical stabilization. Indeed, we have shown that heat coming from homogeneous events tends to be higher than from heterogeneous one from the cycle #10.

# General conclusion and perspectives

In the present research work (in Joule!), infrared thermography and heat source reconstruction (HSR) were applied to polycrystalline NiTi wires tested in tension. The experimental method allowed us to better understand thermomechanical couplings involved in the stress-induced martensitic transformation of NiTi. The following key points have been developed.

The bibliographical chapter (Chapter 1) is a review of the literature on different points related to the topic of the present research work: fundamental points on NiTi SMAs, a state of the art on deformation calorimetry methods, mathematical framework of the thermomechanics of materials, and details about HSR techniques. Special attention was given to superelasticity, one of the well-known functional properties of SMAs. A review of the "deformation calorimetry" approaches was presented. It was shown that HSR is a relevant and appropriate method for characterizing the heterogeneous response of NiTi specimens. NiTi is mainly available and sold in the form of wires, as a result of the manufacturing process. The important remark in Chapter 1 is that, surprisingly, the one-dimensional (1D) HSR approach has never been used to investigate the response of NiTi wire.

Chapter 2 is dedicated to the quantification of the calorific signature of the forward and reverse phase transition, both in time and in space along a *trained* NiTi wire specimen (i.e. a mechanically stabilized specimen), proceeding at relatively high load rates during a force-controlled superelastic cycle. Preliminary, an HSR-based procedure was proposed to characterize the heat exchanges between the specimen and the ambient air. In practice, various intervals of temperature variation during a natural cooling were considered: it was shown that a "variable" characteristic time (i.e. depending on the temperature change with respect with the ambient air temperature) improves the HSR results. Preliminary also, HSR was applied to measure the thermal diffusivity of both the austenite and the *oriented* martensite. To my best knowledge, values for oriented martensite are not available in the literature. It was shown in the present research work that the thermal diffusivity of the oriented martensite was 1.3 times higher than that of austenite. Two important results of Chapter 2 are 1) a successful application of 1D HSR to the characterization of the thermal diffusivity of *oriented* martensite of a trained NiTi wire, 2) a successful application of 1D HSR to the characterization of the spatio-temporal kinetics of the phase transformation during a superelastic cycle. Concerning the second point, the following observations have been made:

- The latent heat generated/absorbed during the forward/reverse martensitic transformation leads to strong thermomechanical coupling that drives the formation of the spatio-temporal distribution of localized transformation patterns (in particular heat bursts) and affects the stress-strain response of the SMA wire.
- Sequentially appearing patterns of localized transformation events of four types were identified. Upon loading, the events were associated with the nucleation of martensite bands and their subsequent merging. Analogically, the events associated with the nucleation of austenite bands and their subsequent merging were identified upon unloading. Events of merging transformation zones were also identified.
- Non-localized heat sources (observed before and after the heat bursts) were associated with homogeneous martensitic transformation.
- The intrinsic dissipation heat associated with the nucleation and merging events (i.e. the heat produced to mechanical irreversibility associated with these events) is estimated to be ~25% of the released/absorbed latent heat.

Chapter 3 is dedicated to the quantification of the calorific signature by 1D HSR of the deformation processes occurring during the first 20 superelastic cycles starting from a *virgin* NiTi wire specimen using a high-speed force control. The stabilization process occurring during *functional* fatigue was thus captured from a calorific point of view. Heat sources (in $W.m^{-3}$) were used to estimate the specific heat (in $J.g^{-1}$) by time integration within each mechanical cycle. Comparison with mechanical work was also made. An important result of Chapter 3 is the evidence of the progressive "delocalization" of the phase transformation events within the specimen upon functional fatigue (i.e., the less and less localized character of the transformation along the first mechanical cycles). The test results can be summarized as follows:

- HSR has proved its efficiency as a fast calorimetric technique thanks to a nearly-adiabatic regime.
- Large temperature variations of about 42 K were observed in the first cycle. After 10 superelastic loadings the material mechanical response reached a stabilized stage with an average peak to peak temperature variation of about 30 K.
- Due to strong thermo-mechanical couplings involved in NiTi, the thermal stabilization was not reached even after 20 cycles applied in total.
- 1D spatio-temporal fields of temperature variations (in K) and of heat sources (in $W.m^{-3}$) showed the localized occurrence of martensitic transformation in the form of martensite band fronts, nucleation sites and merging sites, followed by a progressive "delocalization" of martensitic transformation.
- The magnitude of the specific heat (in $J.g^{-1}$) released during the forward martensitic transformation was greater than the one absorbed during the reverse martensitic transformation, this asymmetry is assumed to be attributed to the stored martensite and work dissipated in form of heat.
- The evaluation of the heat of the heterogeneous and homogeneous events evidenced that martensitic transformation tends to be delocalized after the mechanical stabilization. Indeed, we have shown that heat coming from homogeneous events tends to be higher than that of heterogeneous ones from the 10th cycle.

# Perspectives:

In the present research work, the robustness of HSR has been proven in two "high-speed" force-controlled superelastic cycles. Although the technique has been applied many times, technical problems have not been studied, such as:

- Convective heat exchanges are the result of mechanical-thermal-fluid interactions. The weight of these heat exchanges for "slow" tests can drastically influence the quality of the HSR results. Therefore, a specific study should be conducted based on the experimental and numerical results to possibly improve the mathematical expressions used in this work.
- Development of an appropriate user interface including filtering algorithms to facilitate the reconstruction of the derived operators could be performed. A thorough study using numerical simulations is required to develop an appropriate filtering strategy. Convergence of data smoothing must take into account the different resolutions, namely measurement resolution, spatial resolution, and temporal resolution (see Appendix A). In the current trend of data processing, a machine learning algorithm could be applied and initially be powered by numerical simulations.
- The proposed procedure for HSR-based thermal diffusivity assessment (presented in Section 2.4.2) could be extended to other materials and geometries and developed to determine heterogeneous thermal diffusivity fields. This procedure using a tensile rig offers an excellent alternative to commercial devices for combining mechanical loading with thermophysical property evaluation. In addition, it would be possible to characterize the effect of plasticity on thermophysical properties and improve the fidelity of the HSR and models.
- While in the seminal work of A. Chrysochoos [79] in 1983, HSR was implemented to discuss the validity of the phenomenological mechanical model of material response, only a few attempts have been reconsidered by applying this method. An effort should be made in this direction to improve thermomechanical models, and thus to allow scientists to better understand the response of materials.

# Appendix A: Proceeding SEM

## Chapter 7

## One-Dimensional Heat Source Reconstruction Applied to Phase Transforming Superelastic Ni-Ti Wire

**Antoine Jury, Xavier Balandraud, Luděk Heller, Eduardo Alarcon, and Miroslav Karlik**

**Abstract** The study deals with the reconstruction of heat sources originating from deformation processes in metals. A one-dimensional method to be applied on wires or bars is introduced and tested on superelastic NiTi wire subjected to force-controlled loading and unloading. Infrared thermography was used for this purpose. Thermal data were then processed by heat source reconstruction technique using a one-dimensional version of the heat diffusion equation. Attention was paid to the identification of the heat exchanges with the specimen's environment, in particular by convection to the air of ambient temperature. The sensitivity of the method to the degree of spatio-temporal filtering was also tested. Finally, the localization of martensitic transformation in superelastic NiTi was evaluated using the proposed method. It is shown that under force-control regime the phase transformation proceeds in two time-shifted bursts, where each of bursts consists in several displaced and nearly simultaneous transforming zones. This transformation sequence is rationalized by fast latent heat release from the transforming zone upon load control regime, which leads to overheating of surrounding zones thus temporarily suppressing their transformation.

**Keywords** Shape-memory alloy · NiTi · Infrared thermography · Superelasticity · Heat source reconstruction

### Introduction

Among the shape memory alloys (SMAs), near-equiatomic nickel-titanium (NiTi) alloys are the most frequently selected in engineering applications [1]. This is due to their attractive functional properties exhibited by these alloys, such as shape memory effects, superelasticity and high damping capacity. These macroscopic properties originate from a diffusionless

---

A. Jury (✉)
Nuclear Physics Institute of the CAS, Řež, Czech Republic

Institute of Physics of the CAS, Prague, Czech Republic

Czech Technical University in Prague, Faculty of Nuclear Sciences and Physical Engineering, Department of Materials,
Prague, Czech Republic

Université Clermont Auvergne, CNRS, SIGMA Clermont, Institut Pascal, Clermont-Ferrand, France
e-mail: jury@fzu.cz

X. Balandraud
Université Clermont Auvergne, CNRS, SIGMA Clermont, Institut Pascal, Clermont-Ferrand, France
e-mail: xavier.balandraud@sigma-clermont.fr

L. Heller · E. Alarcon
Nuclear Physics Institute of the CAS, Řež, Czech Republic

Institute of Physics of the CAS, Prague, Czech Republic
e-mail: heller@fzu.cz; alarcon@fzu.cz

M. Karlik
Czech Technical University in Prague, Faculty of Nuclear Sciences and Physical Engineering, Department of Materials, Prague, Czech
Republic

Charles University, Faculty of Mathematics and Physics, Department of Physics of Materials, Prague, Czech Republic
e-mail: miroslav.karlik@fjfi.cvut.cz

A. Baldi (ed.), *Residual Stress, Thermomechanics & Infrared Imaging and Inverse Problems, Volume 6*,
Conference Proceedings of the Society for Experimental Mechanics Series, https://doi.org/10.1007/978-3-030-30098-2_7

solid-solid phase transformation that can be thermally or mechanically induced. According to the thermomechanical heat treatment, environmental conditions (ambient temperature and heat exchange conditions) and mechanical loading (stress level and loading rate), the tensile response of polycrystalline NiTi-based SMAs may exhibit the propagation of phase transformation fronts [2]. The latter were extensively studied in the literature. They were described first in [3] and then investigated in many studies (see for instance [4–7]). The reader is also referred to [8] for details on the origin of these phase transformation fronts.

The stress-induced phase transformation in NiTi wires subjected to tension is usually tracked in-situ by measuring sudden changes of strain and strain rates, both evaluated either integrally using displacement of the testing machine's cross-head, more accurately using clip-on extensometer, or locally using digital image correlation. Thermal Field Measurements (TFM), based on the use of an infrared (IR) camera [4–6, 9–11] are an alternative way of tracking in-situ the phase transformation in NiTi. In general, TFM takes advantage of temperature changes that always accompany material stretching due to thermomechanical couplings and intrinsic dissipation: thermoelastic coupling, latent heat due to solid-solid phase change, self-heating due to plasticity, viscosity or fatigue damage. The reconstruction of heat sources from temperature changes is possible by using the heat diffusion equation, which in the case of wires can be reduced into 1-D considering axial symmetry and seeking for heat sources integrally over the entire wire cross-section. By *heat source*, we mean the heat power density produced or absorbed by the material itself (i.e. not due to conduction, convection and radiation). To the best knowledge of the authors, one dimensional heat source reconstruction has never been carried out on NiTi subjected to force controlled tensile loadings. In fact, the phase transformation in NiTi normally proceeds under a constant plateau-stress but it cannot under the force controlled loading regime as the latent heat of rapidly transformed zones increases the temperature of their surroundings where the phase transformation may be temporarily suppressed. It may lead to sudden bursts and arrests of the phase transformation along the wire axis appear in NiTi wire. Hence, superelastic NiTi subjected to the force controlled regime represents a perfect example case for present work aiming at the development and testing of a method for one-dimensional reconstruction of heat sources evolving dynamically in time and heterogeneously in space.

The paper is divided into three sections as follows. The first section provides the general background on 1D heat source reconstruction. The second section presents the NiTi material experimental set-up. Finally, results are given and discussed in the third section, with a focus on the spatio-temporal features of phase change fronts along the NiTi wire during a load-unload cycle.

## Methodology for Heat Source Reconstruction

Materials produce or absorb heat when subjected to mechanical loadings. As indicated in the introduction, heat sources are defined as the heat power densities (in W m$^{-3}$) resulting in a temperature changes. In metals, heat is produced or absorbed as a consequence of different deformation and chemical processes. For instance, the thermomechanical coupling upon elastic deformation in metals, called thermoelasticity, results in a heat production inversely proportional to the applied stress rate. On the other hand, phenomena related to energy dissipation such as plasticity, viscosity, fatigue damage always results in irreversible heat production. In NiTi, an additional thermomechanical coupling is involved: a production or absorption of latent heat associated with the austenite-to-martensite or martensite-to-austenite phase changes, respectively. Using the heat diffusion equation, heat sources can be reconstructed from the temperature fields captured by IR thermography at the specimen surface [10–17]. In the present study, we used the so-called 1D approach [10, 13, 14] for reconstructing the heat sources of NiTi wires subjected to force-controlled tensile loadings.

Let us consider a straight NiTi wire whose axial coordinate is denoted $z$. The simplified local form of the heat equation (7.1) provides the relationship between the temperature change $\Theta(z,t)$ and the heat source $s(z,t)$ (here expressed in °K s$^{-1}$ resulting from its reduction by the product of the density $\rho$ and the specific heat $C$). The latter quantity is defined with respect to a reference configuration, considered in practice as the unloaded state in thermal equilibrium. The parameter $D$ is the thermal diffusivity of the material (in m$^2$ s$^{-1}$) and $\tau$ is a characteristic time (in s) characterizing the heat exchanges between the wire lateral surface and its surroundings. The calculation of heat source from the right-hand side of Eq. (7.1) was implemented using derivative Gaussian filters, as detailed in [16].

$$s(z,t) = \frac{d\Theta(z,t)}{dt} + \frac{\Theta(z,t)}{\tau} - D\frac{d^2\Theta(z,t)}{dz^2} \tag{7.1}$$

The characteristic time $\tau$ was evaluated from a natural cooling of the sample to ambient temperature after its homogeneous heating without any contact with the jaws of the testing machine. In practice, the specimen was suspended in air with a piece of tape. Figure 7.1a shows the temperature change $\Theta(t)$ during a homogeneous natural return to ambient temperature after homogeneous heating using a hot air gun. In this way, we consider only the heat exchange of the lateral surface of the specimen with its surroundings. As the heat source is equal to zero (the specimen did not produce heat), Eq. (7.1) becomes:

$$0 = \frac{d\Theta}{dt} + \frac{\Theta}{\tau} \tag{7.2}$$

If $\tau$ is a constant, the solution of Eq. (7.2) is a decreasing exponential function of the cooling duration. Assuming that $\tau$ may potentially depend on the temperature change $\Theta$, it was proposed to identify the value of $\tau(\Theta)$ for different portions of the curve $\Theta(t)$ as illustrated in Fig. 7.1a. A minimization algorithm was employed with a correlation index equal to 0.995 as stopping criteria. Results are presented in Fig. 7.1b, each point corresponding to the value of $\tau$ for a given portion of the curve. A linear equation was identified for the function $\tau(\Theta)$. Figure 7.1c shows the residual heat sources obtained using experimental data. The latter corresponds to the right-hand side of Eq. (7.2) as calculated using the linear fit of $\tau(\Theta)$ (Fig. 7.1b). In fact, the residual heat source values should be equal to zero during this natural return to ambient temperature. The curve in Fig. 7.1c thus provides an estimation of the measurement resolution of the heat source in the case of homogeneous temperature fields: a few tenth of one K s$^{-1}$ at the maximum.

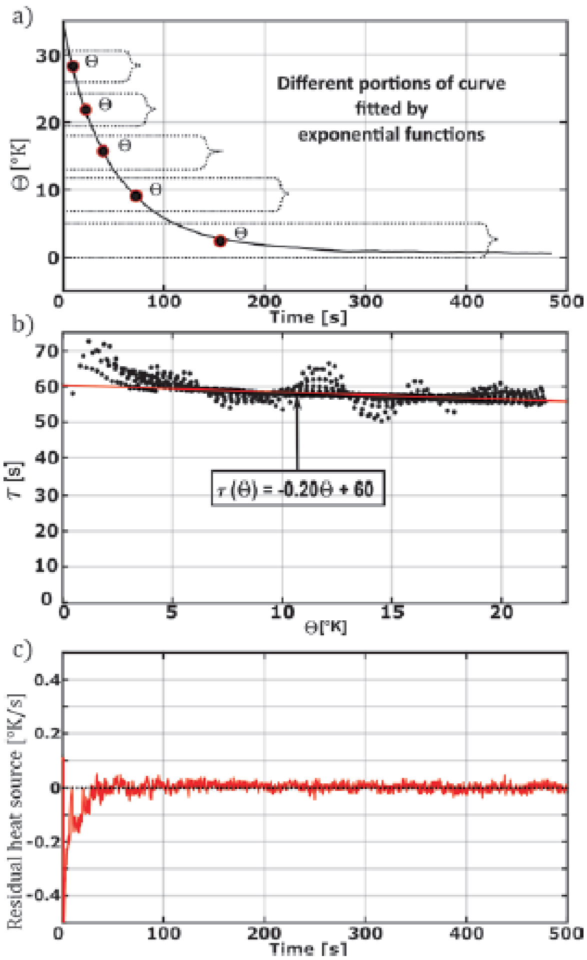

**Fig. 7.1** Identification of the characteristic time $\tau$: (**a**) temperature change $\Theta$ during a homogeneous natural return to ambient temperature, (**b**) values of $\tau$ as a function of $\Theta$, (**c**) residual heat sources obtained after heat source reconstruction

The thermal diffusivity $D$ was measured using a similar approach. We calculated Eq. (7.1) during the natural cooling after a local heating. This time, the specimen was clamped in the jaws of the machine, then heated locally by gently applying a pressure in the middle of the specimen with the fingers. A unique value of $D$ was identified at room temperature equal to $2.7 \times 10^{-6}$ m$^2$ s$^{-1}$, which is in agreement with [15].

## Experimental Set-Up

A Cedip Jade III-MWIR infrared camera was employed to capture the temperature fields after calibration in the range [268 K; 333 K]. The mechanical loading was applied with an MTS uniaxial machine equipped with a 15 kN load cell. Figure 7.2a presents a schematic view of the NiTi wire during heat treatment by Joule effect. Figure 7.2b, c show the wire placed in the mechanical test configuration. It can be noticed that two reference elements made of the same material were added on both sides of the mechanically tested specimen: each reference was clamped in a jaw of the testing machine. This experimental device was introduced in [11]. Effects of changes in the specimen's environment during a test can be tracked thanks to these reference elements: change in temperature of the jaws of the testing machine, in temperature and flow of the ambient air, and more generally any change of the testing room conditions (machines, persons, walls, etc.). The NiTi wire and its two reference elements were painted in black to maximize the thermal emissivity, as well as the close environment to limit parasitic reflections: see Fig. 7.2c.

The specimen was a Ni-Ti SMA wire of 1.78 mm of diameter, supplied by Fort Wayne Metals. It was preliminary heat treated by Joule effect using a 50 A current for a period of 3.5 s as presented in [18]. It was then subjected to mechanical training at ambient temperature (≈300 K) for 20 cycles at ±392 N s$^{-1}$ between 20 N and 1984 N. Lengths L1 and L2 in Fig. 7.1a were equal 40 mm and 80 mm, respectively. These lengths were used for both the annealing treatment and the mechanical loadings. The wire is fully austenitic at ambient temperature in the stress-free state.

A tensile test was carried out on the specimen in a force-controlled mode with a rate of ±20 N s$^{-1}$, and same minimum and maximum forces as for the preliminary mechanical training. The room temperature was 300 K. The spatial resolution of the full-field thermal measurement was equal to 148.5 µm (will be referred to as $dz$ in the following). Recording frequency was set to 162 Hz, leading to a temporal resolution of 6.17 ms (will be referred to as $dt$). As we are interested in localized phase transformation phenomena (both in time and in space), there is a compromise to be found between measurement resolution (improved by filtering) and spatial/temporal resolution (penalized by filtering and derivation) for the calculation of the heat sources from Eq. (7.1).

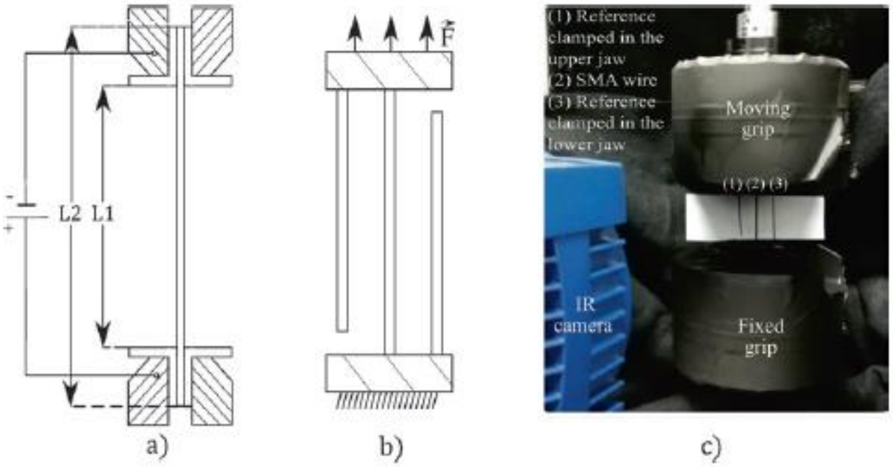

**Fig. 7.2** (**a**) Schematic view of the NiTi wire during heat treatment by Joule effect, (**b**) schematic view of the specimen with two reference elements for thermomechanical analysis, (**c**) photo of the specimen and reference elements placed in the jaws of the testing machine

## Analysis

Heat source reconstruction was implemented using first-derivative (in time) Gaussian filter in time for the term $d\Theta/dt$ and second-derivative (in space) Gaussian filter in space for the term $d^2\Theta/dz^2$. No filter was applied to the term $\Theta/\tau$. Figure 7.3 shows the influence of the standard deviations $\sigma_{space}$ (in mm) and $\sigma_{time}$ (in s) of the two Gaussian functions on the spatio-temporal heat source distribution around a short and localized event (see Fig. 7.4 for a global view along the whole duration of the test and the whole length of the wire). The kernel sizes of the convolution windows were set to $\pm 4.5\sigma_{space}$ in space and $\pm 3\sigma_{time}$ in time, i.e. 9 and 6 times the standard deviations respectively. In practice, $\sigma_{space}$ and $\sigma_{time}$ were expressed in terms of multiple of the spatial and temporal resolutions of the thermal fields:

$$\sigma_{space} = k_{space}dz \text{ and } \sigma_{time} = k_{time}dt \tag{7.3}$$

where $k_{space}$ and $k_{time}$ are integers.

Figure 7.3a presents the temperature change $\Theta(z, t)$ of a strong calorific event that we used to investigate appropriate filter parameters. Figure 7.3b shows the heat sources that were reconstructed using only a finite difference (FD) scheme

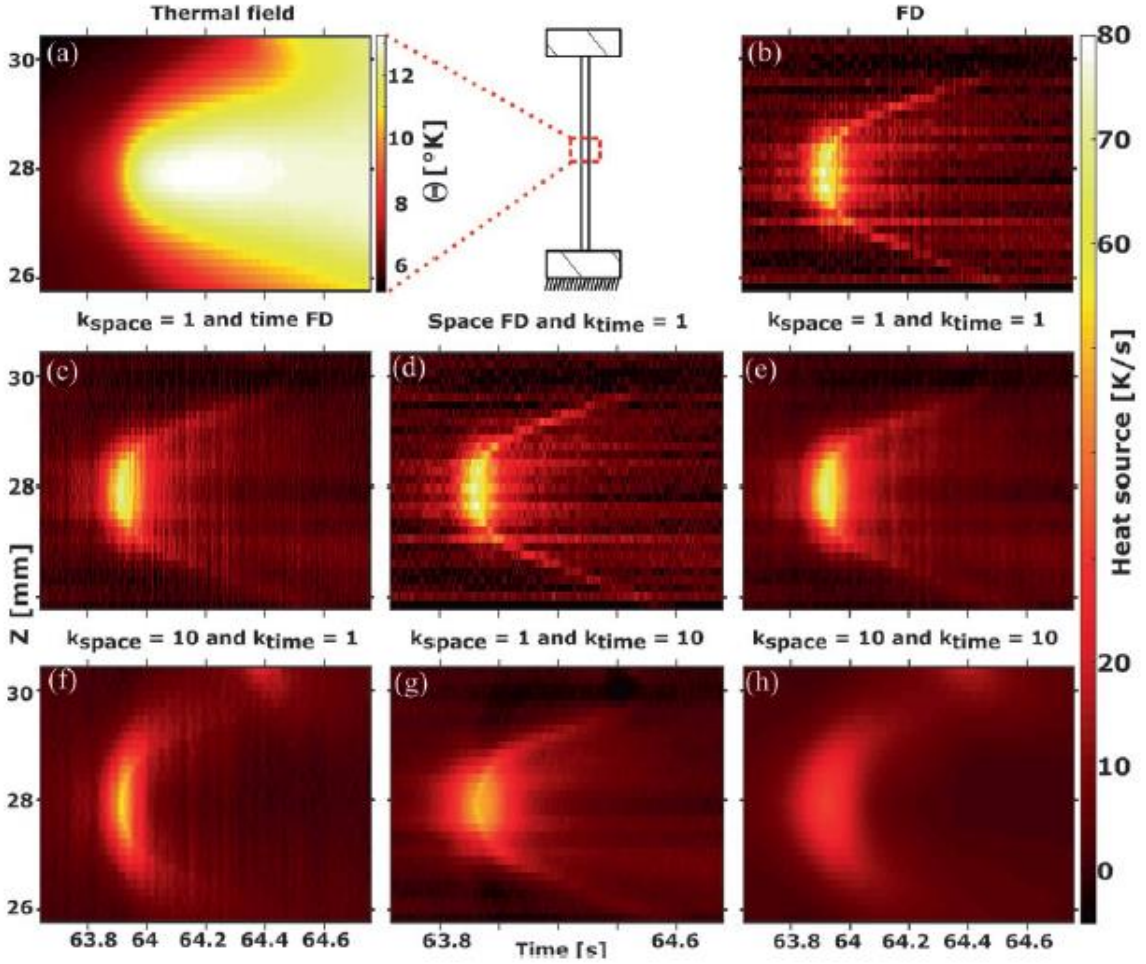

**Fig. 7.3** (**a**) Temperature change $\Theta$ around a short and localized calorific event, (**c**–**h**) influence of the standard deviations in terms of multiples of spatial ($k_{space}$) and temporel ($k_{time}$) resolutions $\sigma_{space}$ and $\sigma_{time}$ of the Gaussian derivative filters on the reconstructed heat sources as compared with the solution vie Finite differences (FD) method (**b**)

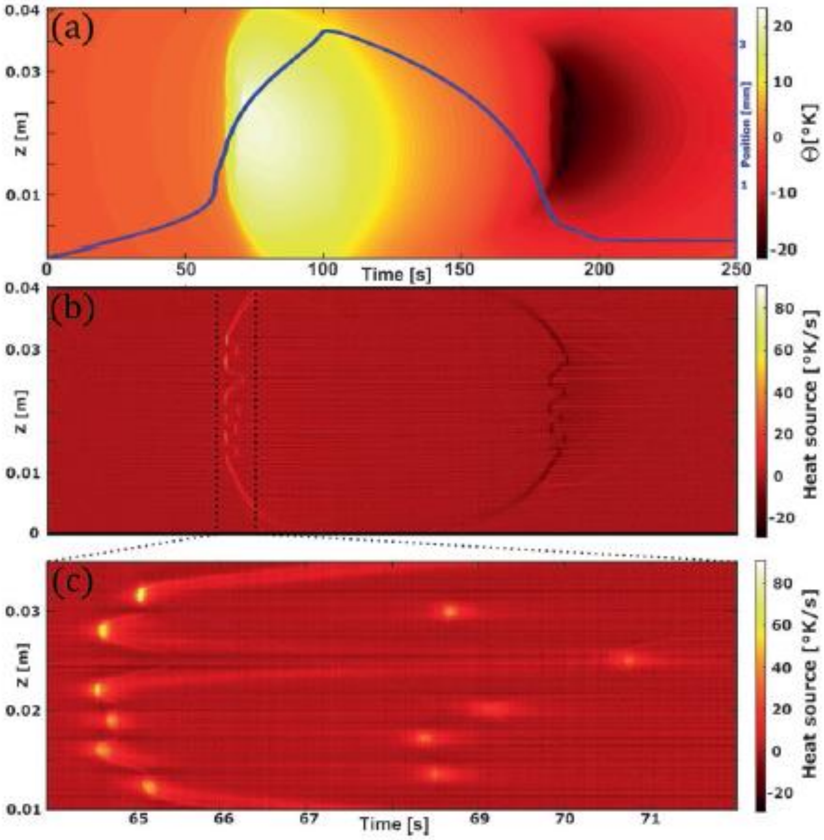

**Fig. 7.4** Load-unload cycle: (**a**) temperature change $\Theta$ as a function of time and space. The displacement of the actuator is also plotted as a function of time; (**b**) heat source reconstructed from the temperature changes, mapped over the whole duration of the test, (**c**) zoom on the heat source map over the short period revealing strong hear source activity

named forward time centered space of the right-hand side of Eq. (7.1), without filtering. Figure 7.3c–h show the heat sources reconstructed using Gaussian derivation filters for the two derivative terms. It is worth noting that, by construction, heat sources are much more localized in time and in space that the temperatures. Indeed, heat source reconstruction is a physics-based data processing that removes heat exchanges with the specimen surroundings and the heat conduction through the axis of the specimen. It can be also noted that filtering tends to smooth the calorific phenomena. The case for which $\sigma_{space} = dz$ and $\sigma_{time} = dt$ appears to be a good compromise: see Fig. 7.3e. In other words, the advantageous signal-to-noise ratio of the thermal data allows us to apply a "soft" filtering without strongly penalizing the spatial and temporal resolutions of the heat sources. The chosen spatial and temporal resolutions of the reconstructed heat sources are then equal to 1.04 mm and 43.4 ms respectively.

Figure 7.4a presents the temperature change $\Theta(z, t)$, as well as the position of the actuator, as a function of time during the load-unload cycle. Figure 7.4b shows the map of the reconstructed heat source, and Fig. 7.4c shows a zoom over the forward phase transformation (delimited between dotted lines in Fig. 7.4b). The following comments can be made with respect to these graphs.

- Up to approximatively 64 s, the actuator moved quasi-linearly, exhibiting an elastic response of the NiTi wire. Although unseen in Fig. 7.4, the temperature slightly decreased during the first seconds as expected due to thermoelastic coupling: decrease of about 0.02 K in 3.5 s. Then the temperature kept rising continuously and homogeneously up to reach a value of 2 K above the ambient temperature. This increase might be related to premartensitic R-phase transformation, although further investigations are needed to confirm it. It can be noted that the corresponding heat sources of these two phenomena are not detectable because of the chosen filtering parameters (broader filtering windows would enhance the information about this quasi-homogeneous phenomenon, similar to the so-called zero-dimensional approach [14]).

- From 64 s to 68 s approximatively, the actuator position rate rapidly increased due to the large transformation strain of the stress-induced martensitic transformation. It is accompanied by a strong temperature increase of the wire. This is attributed to the production of latent heat of the phase transformation. Six transformation zones separated by non-transforming zones appeared in less than one second (at around 65 s). Four of the non-transforming zones transformed almost 4 s later, and the last one did it 6 s later. The length of individual transformation zones is ~1.5 mm. Figure 7.3 reveals that the duration of individual transformation zones is shorter than 0.1 s. The burst of an individual transformation zone was followed by two transformation fronts propagating upwards and downwards indicated by inclined heat source traces (covering a total distance of less than 1.5 mm in less than 0.1 s).
- The intensity of the heat sources at the first six transformation zones is two higher than the intensity of the following five.
- It can be noted that continuous propagation of phase transformation fronts also occurred at the two ends of the wire, just after the appearance of the first six martensitic zones (see Fig. 7.4b).
- The reverse transformation, starting at ~150 s, is characterized by heat absorption. The intensity of the heat sources upon the reverse transformation is, however, three times lower than the one observed upon the forward transformation. The differences might be related to other material processed occurring simultaneously upon phase transformations such as plasticity.
- Unlike the forward phase transformation, the reverse transformation initiates inside the clamping jaws. There is not an evident correspondence between the order of activation of the transformation zones upon loading and unloading. The number of localized transformation zones upon the reverse transformation is even lower than upon the forward transformation.

## Conclusion

We apply the 1D heat source reconstruction to track the heterogeneous distribution of stress-induced phase transformation in superelastic NiTi upon a force controlled tensile loading-unloading test. Significant temperature changes were observed, as a result of the strong thermomechanical coupling associated supposedly with phase transformations (production and absorption of latent heat). Recorded temperature fields were successfully converted into spatio-temporal evolutions of heat sources associated with forward and reverse martensitic transformation. Attention was paid to the choice of processing parameters with respect to the spatial and temporal resolutions required for a suitable identification of the spatial and temporal kinetics of transformation: rapid nucleation of small martensitic zones and propagation of phase transformation fronts. The method allowed to identify sudden bursts and arrests of phase transformation due to heat effects. In fact, the force controlled loading regime leads to a burst of several phase transformation zones that are displaced due to increasing temperature of their surroundings where the phase transformation is suppressed. These zones can transform only after a sufficient stress increase and/or temperature decrease as a consequence of transformation stress-temperature coupling in NiTi. Consequently, the phase transformation proceeds in two bursts of several displaced transformation zones, where the second burst is shifted in time and related transformation zones fill the non-transformed volume left after the first one.

**Acknowledgements** This publication was supported by OP RDE, MEYS, under the project "European Spallation Source—participation of the Czech Republic—OP", "Reg. No. CZ.02.1.01/0.0/0.0/16_013/0001794". A.J. acknowledges the support received from the Agence Nationale de la Recherche of the French government through the program "Investissements d'Avenir" (16-IDEX-0001 CAP 20-25). M.K. would like to acknowledge financial support of the ERDF in the frame of the Project No. CZ.02.1.01/0.0/0.0/15_003/0000485.

## References

1. C. Otsuka, K. Wayman, *Shape Memory Materials* (Cambridge University Press, Cambridge, 1999)
2. H. Yin, Y. He, Q. Sun, Effect of deformation frequency on temperature and stress oscillations in cyclic phase transition of NiTi shape memory alloy. J. Mech. Phys. Solids **67**, 100–128 (2014)
3. S. Miyazaki, T. Imai, K. Otsuka, Y. Suzuki, Lüders-like deformation observed in the transformation pseudoelasticity of a Ti-Ni alloy. Scr. Metall. **15**, 853–856 (1981)
4. H. Louche, P. Schlosser, D. Favier, L. Orgéas, Heat source processing for localized deformation with non-constant thermal conductivity. Application to superelastic tensile tests of NiTi shape memory alloys. Exp. Mech. **52**(9), 1313–1328 (2012)
5. J.A. Shaw, S. Kyriakides, Thermomechanical aspects of NiTi. J. Mech. Phys. Solids **43**(8), 1243–1281 (1995)

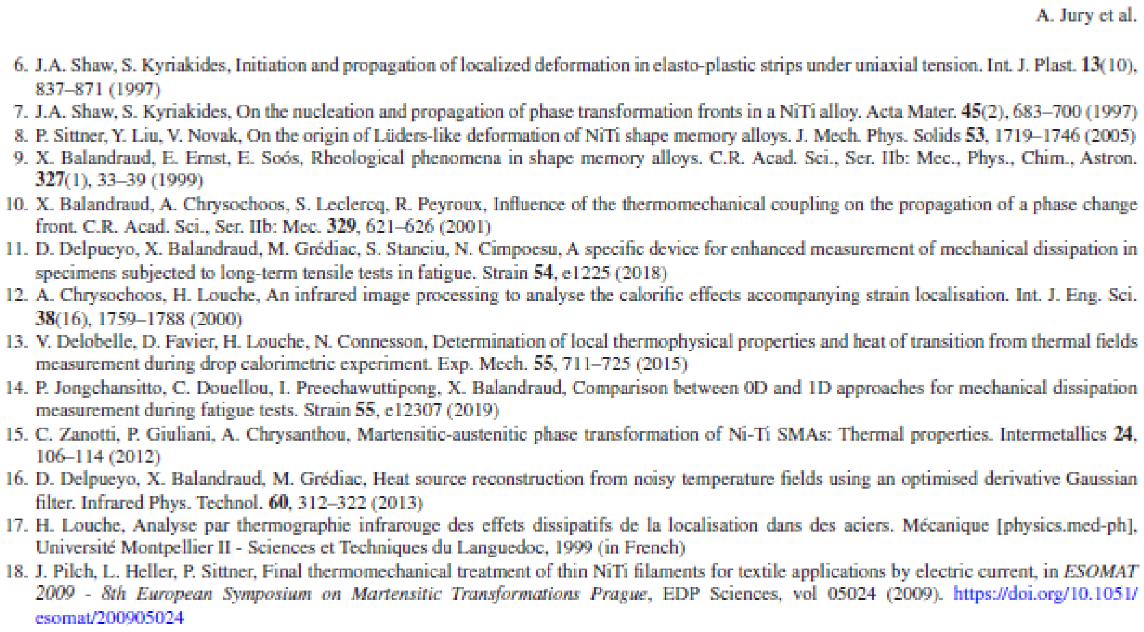

6. J.A. Shaw, S. Kyriakides, Initiation and propagation of localized deformation in elasto-plastic strips under uniaxial tension. Int. J. Plast. **13**(10), 837–871 (1997)
7. J.A. Shaw, S. Kyriakides, On the nucleation and propagation of phase transformation fronts in a NiTi alloy. Acta Mater. **45**(2), 683–700 (1997)
8. P. Sittner, Y. Liu, V. Novak, On the origin of Lüders-like deformation of NiTi shape memory alloys. J. Mech. Phys. Solids **53**, 1719–1746 (2005)
9. X. Balandraud, E. Ernst, E. Soós, Rheological phenomena in shape memory alloys. C.R. Acad. Sci., Ser. IIb: Mec., Phys., Chim., Astron. **327**(1), 33–39 (1999)
10. X. Balandraud, A. Chrysochoos, S. Leclercq, R. Peyroux, Influence of the thermomechanical coupling on the propagation of a phase change front. C.R. Acad. Sci., Ser. IIb: Mec. **329**, 621–626 (2001)
11. D. Delpueyo, X. Balandraud, M. Grédiac, S. Stanciu, N. Cimpoesu, A specific device for enhanced measurement of mechanical dissipation in specimens subjected to long-term tensile tests in fatigue. Strain **54**, e1225 (2018)
12. A. Chrysochoos, H. Louche, An infrared image processing to analyse the calorific effects accompanying strain localisation. Int. J. Eng. Sci. **38**(16), 1759–1788 (2000)
13. V. Delobelle, D. Favier, H. Louche, N. Connesson, Determination of local thermophysical properties and heat of transition from thermal fields measurement during drop calorimetric experiment. Exp. Mech. **55**, 711–725 (2015)
14. P. Jongchansitto, C. Douellou, I. Preechawuttipong, X. Balandraud, Comparison between 0D and 1D approaches for mechanical dissipation measurement during fatigue tests. Strain **55**, e12307 (2019)
15. C. Zanotti, P. Giuliani, A. Chrysanthou, Martensitic-austenitic phase transformation of Ni-Ti SMAs: Thermal properties. Intermetallics **24**, 106–114 (2012)
16. D. Delpueyo, X. Balandraud, M. Grédiac, Heat source reconstruction from noisy temperature fields using an optimised derivative Gaussian filter. Infrared Phys. Technol. **60**, 312–322 (2013)
17. H. Louche, Analyse par thermographie infrarouge des effets dissipatifs de la localisation dans des aciers. Mécanique [physics.med-ph], Université Montpellier II - Sciences et Techniques du Languedoc, 1999 (in French)
18. J. Pilch, L. Heller, P. Sittner, Final thermomechanical treatment of thin NiTi filaments for textile applications by electric current, in *ESOMAT 2009 - 8th European Symposium on Martensitic Transformations Prague*, EDP Sciences, vol 05024 (2009). https://doi.org/10.1051/esomat/200905024

# Appendix B: additional data for Chapter 3

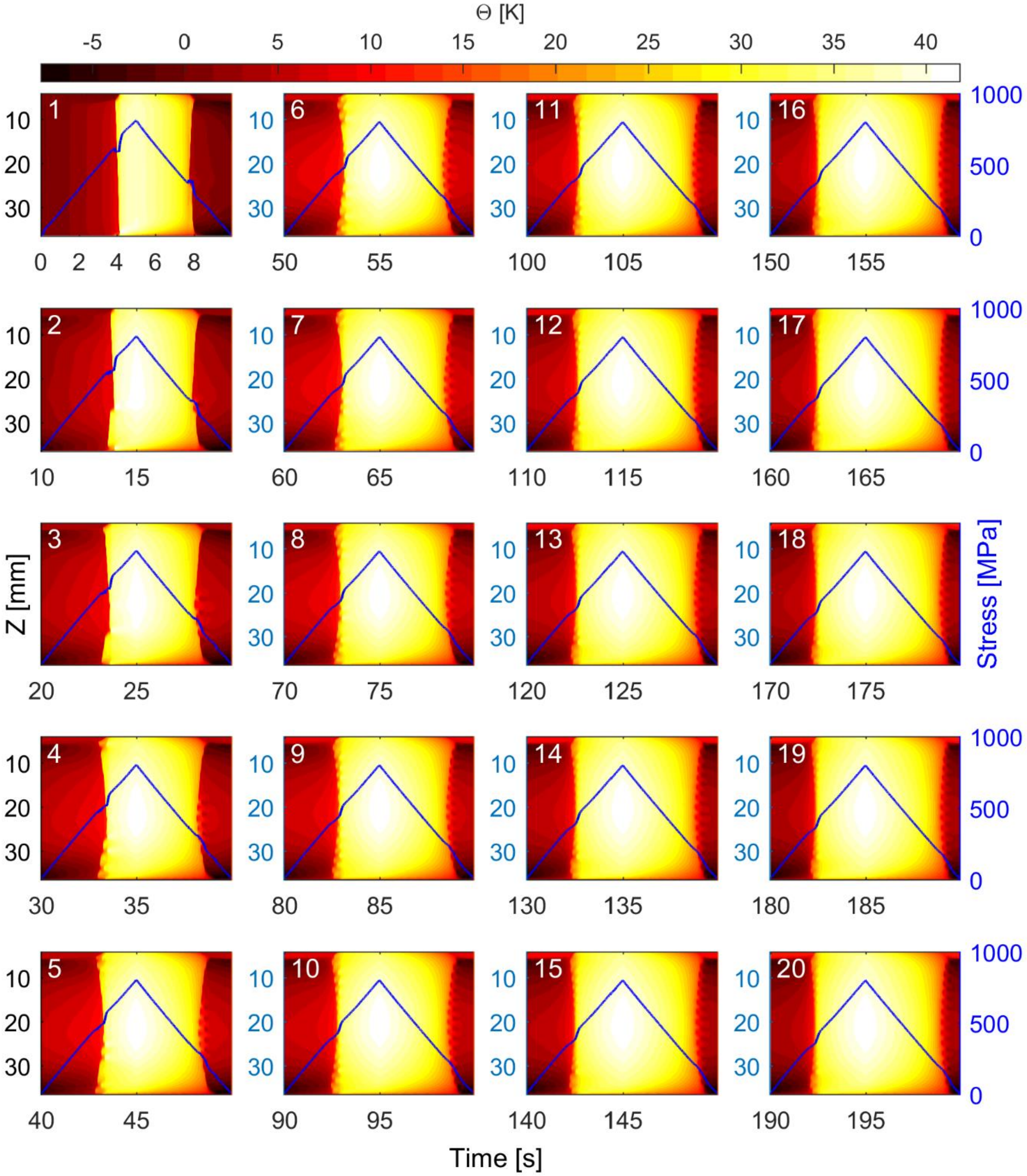

Spatio-temporal colormap of **temperature variation** and stress variation (blue curves) along the mechanical cycles.

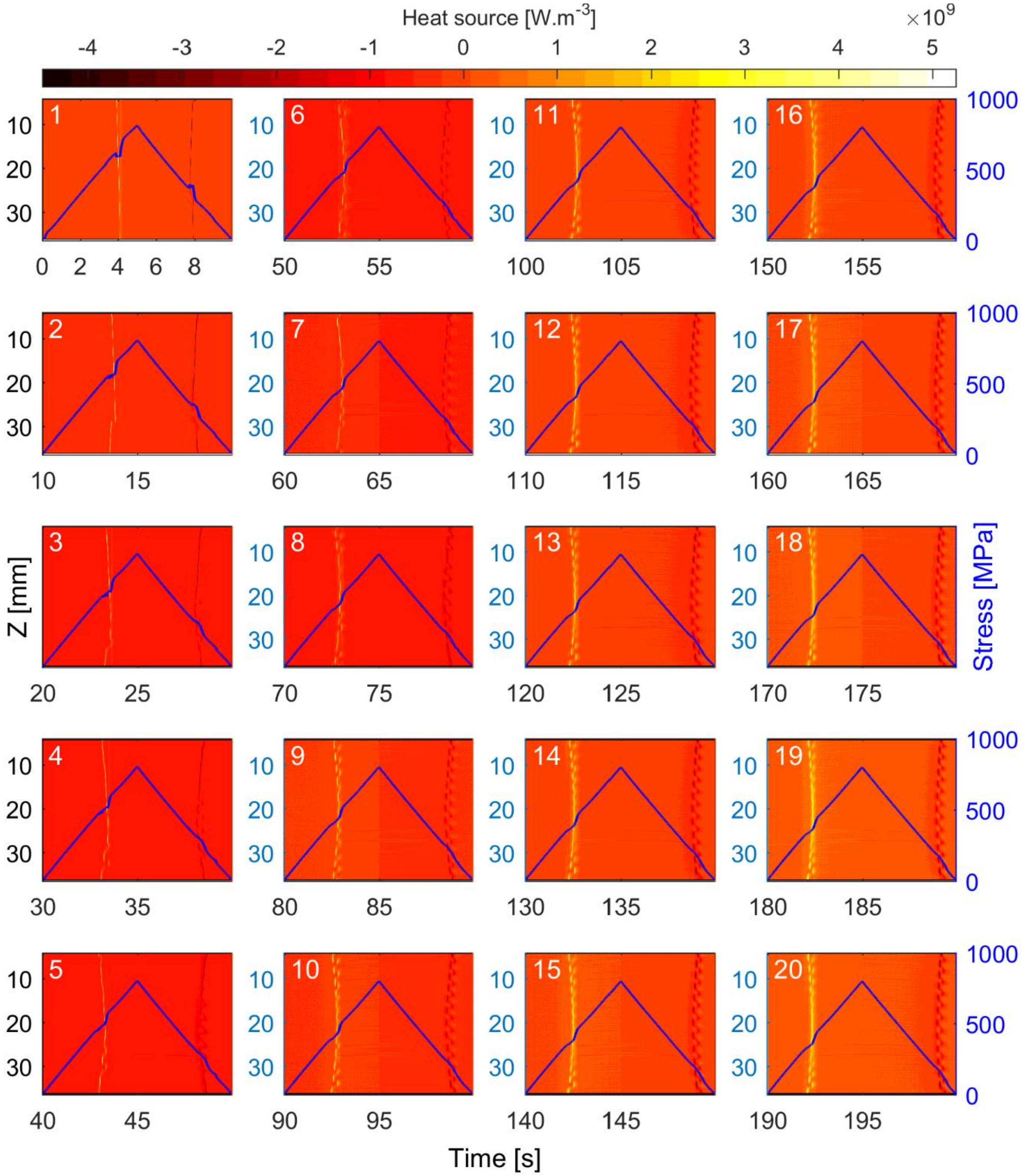

Spatio-temporal colormap of **heat source** and stress variation (blue curves) along the mechanical cycles.

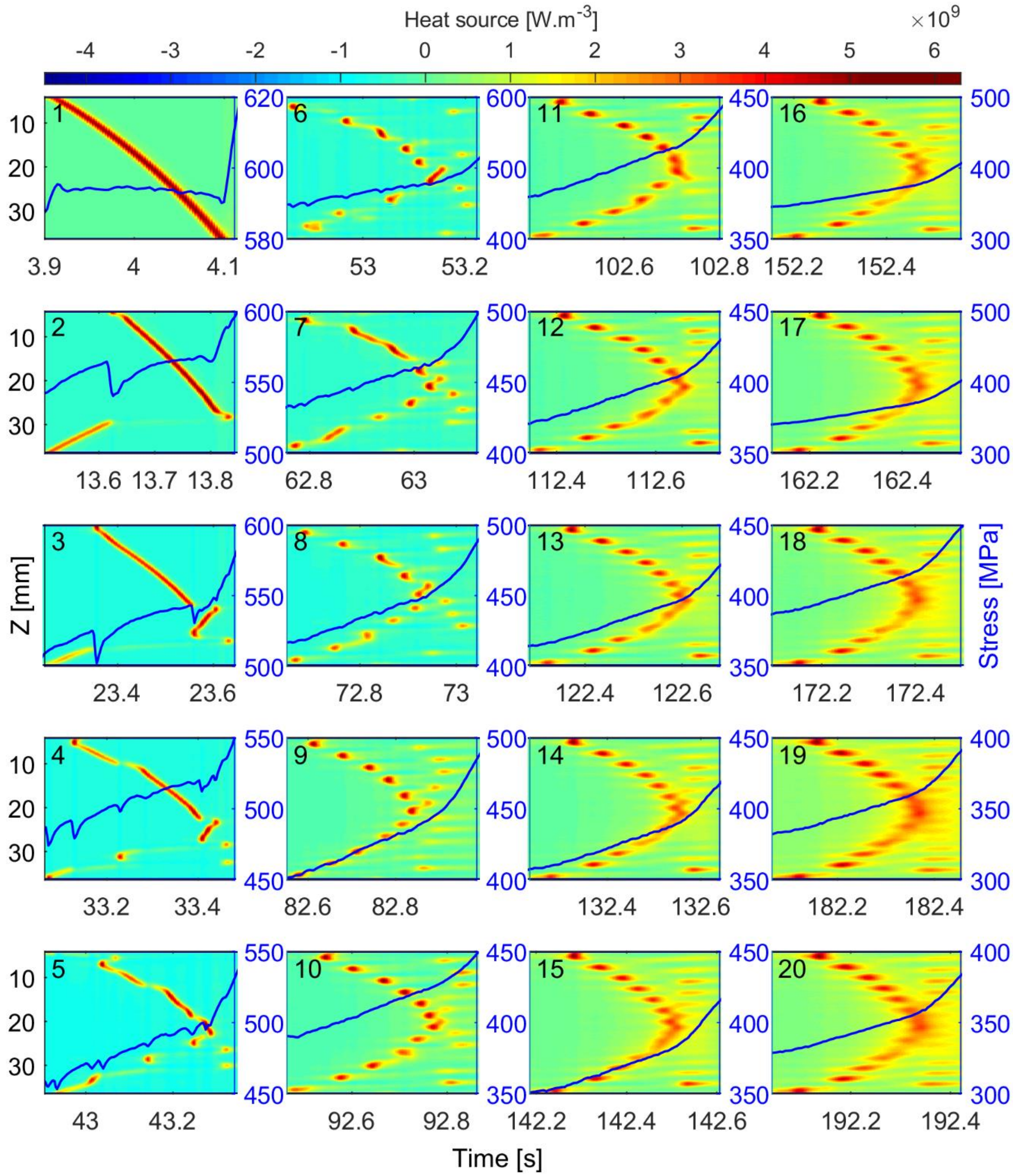

Spatio-temporal colormap of **heat source** on short durations during **forward martensitic transformation**, and stress variation (blue curves).

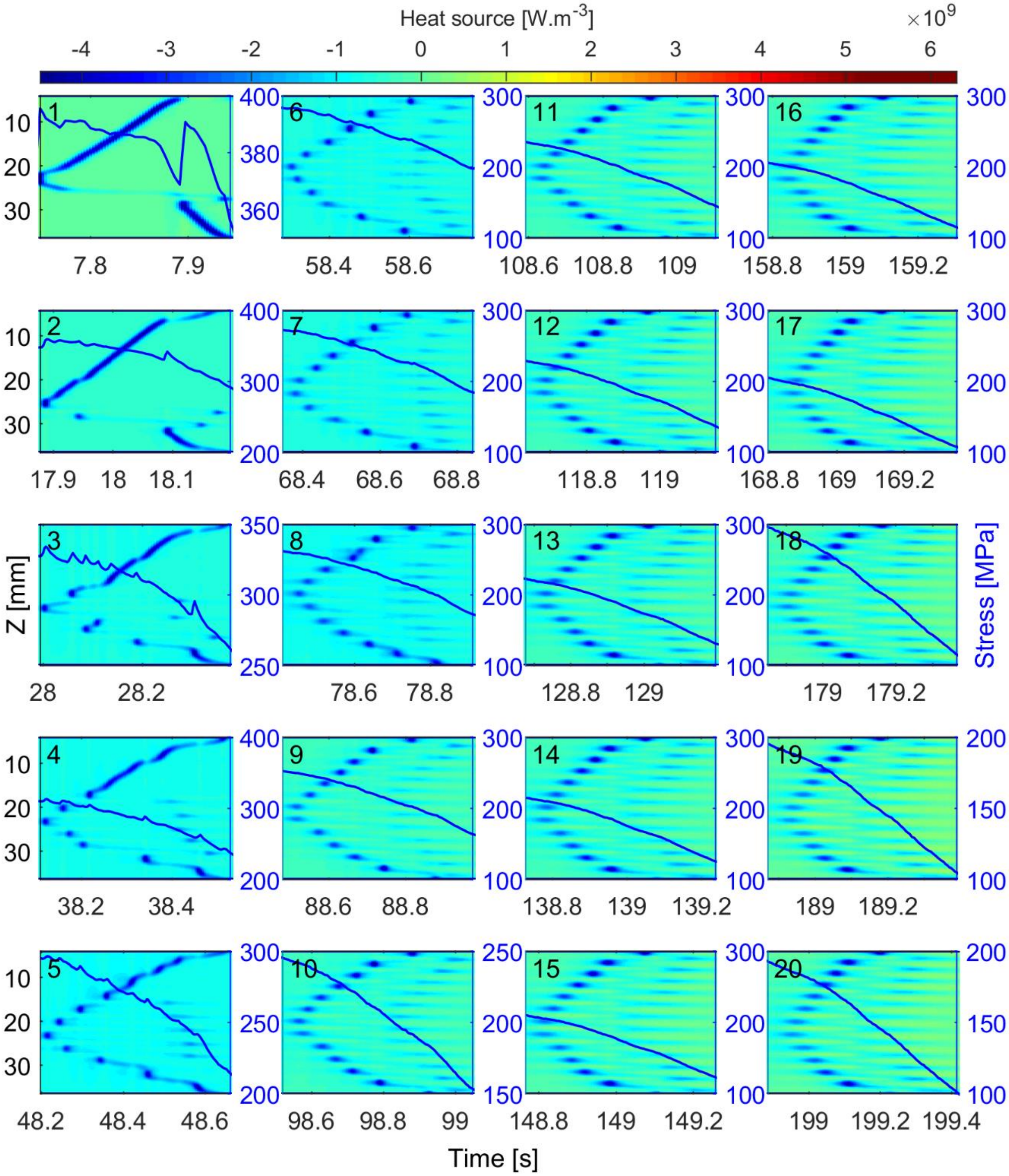

Spatio-temporal colormap of **heat source** on short durations during **reverse martensitic transformation**, and stress variation (blue curves).

# Appendix C: localized events energy extraction in Chapter 3

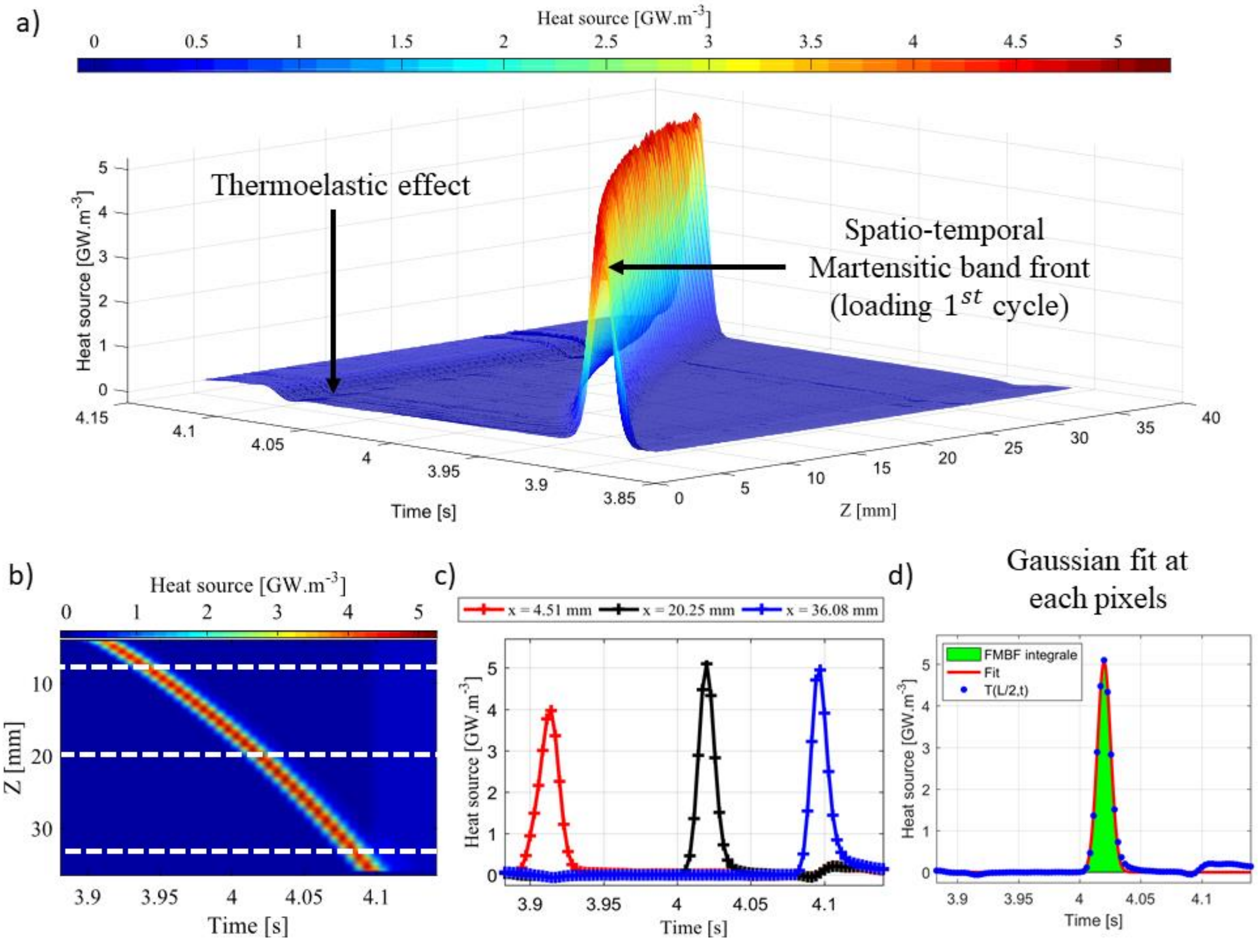

Example of procedure for extraction of martensitic band front energy, **a)** spatio-temporal **heat source** field presented in 3D, **b)** same in 2D, **c)** variation of the heat source at three different material points (x = [4.51, 20.25, 36.08] mm), **d)** example of Gaussian fitting at a given material point. Blue dots correspond to experimental data. Red curve is the fitting using Gaussian function. Green area represents integral of the fitted curve.

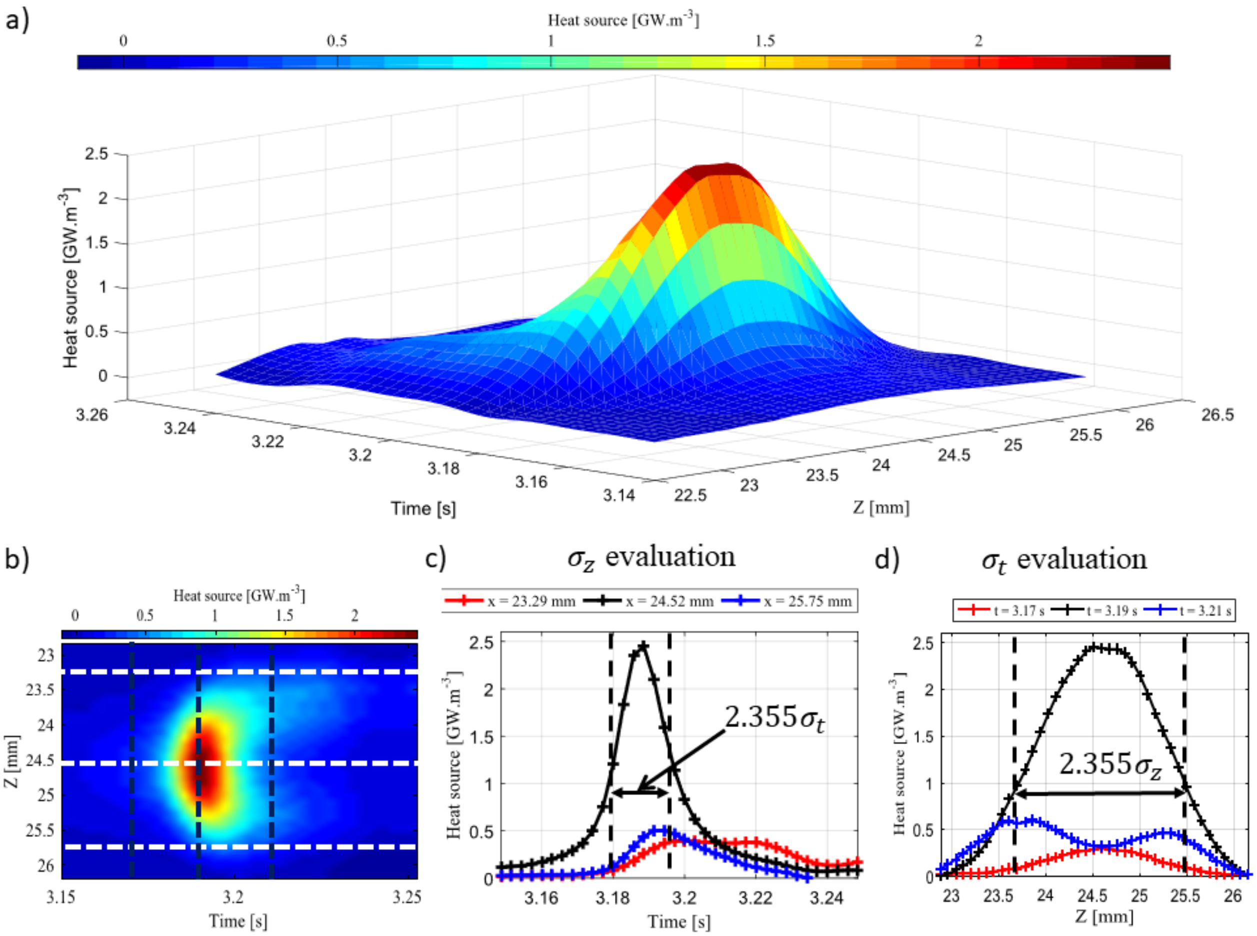

Example of procedure for extraction of nucleation site and merging site energies and estimation of the spatio-temporal standard deviations, **a)** spatio-temporal **heat source** field presented in 3D, **b)** same in 2D, **c)** variation of the heat source at three different material points (x = [23.29, 24.52, 25.75] mm), **d)** variation of the heat source at three different instants (t = [3.17, 3.19, 3.21] s). The spatio-temporal standard deviations are estimated using FWHM criterion.

# List of Publications

**Article:**

[1] **A. Jury**, X. Balandraud, L. Heller, P. Sittner, M. Karlik, “Reconstruction of heat sources induced in superelastically loaded Ni-Ti wire by localized deformation processes”, *Experimental Mechanics* 61, 349-366, 2021, https://doi.org/10.1007/s11340-020-00648-8

[2] M. Frost, A. Jury, L. Heller, P. Sedlak, “Experimentally validated constitutive model for NiTi-based shape memory alloys featuring intermediate R-phase transformation: A case study of Ni48Ti49Fe3”, *Materials & Design* 203, 109593, 2021 https://doi.org/10.1016/j.matdes.2021.109593

**Conference proceedings:**

[3] **A. Jury**, X. Balandraud, L. Heller, E. Alarcon, M. Karlik, “One-dimensional heat source reconstruction applied to phase transforming superelastic Ni-Ti wire”, in: A. Baldi (ed.) *Residual Stress, Thermomechanics & Infrared Imaging and Inverse Problems*, Volume 6, Chapter 7, Conference Proceedings of the Society for Experimental Mechanics Series, Reno, USA, 3-6 June 2019, Springer, Cham, 2020. https://doi.org/10.1007/978-3-030-30098-2_7

**Presentations in international conference:**

[4] **A. Jury**, L. Heller, E. Alarcon, P. Sittner, R. Stalmans, C.F. Promper, “Thermomechanical characterization of NiTiFe for pipe coupling application”, *ESOMAT (European Symposium on Martensitic Transformations)*, Metz, France, 27-31 August 2018.

[5] L. Heller, P. Sittner, L. Kaderavek, O. Tyc, E. Alarcon, **A. Jury**, X. Balandraud, “Transformation-plasticity coupling in superelastic NiTi characterized by in-situ DIC, resistometry, IR thermography and DMA”, *IUTAM’19 Phase Transformations in Shape Memory Materials: Modeling and Applications*, The University of Texas at Austin, USA, April 28 – May 2, 2019

[6] E. Alarcon, L. Heller, **A. Jury**, P. Sittner, X. Balandraud, “Heat dissipated at moving austenite-martensite interfaces in superelastic NiTi wires”, *IUTAM’19 Phase Transformations in Shape Memory Materials: Modeling and Applications*, The University of Texas at Austin, USA, April 28 – May 2, 2019

# References

[1] S. Miyazaki, M. Fremond, Shape Memory Alloys, CISM Inter, Springer-Verlag Wien, 1996. https://doi.org/10.1007/978-3-7091-4348-3.

[2] K. Otsuka, X. Ren, Physical metallurgy of Ti-Ni-based shape memory alloys, Prog. Mater. Sci. 50 (2005) 511–678. https://doi.org/10.1016/j.pmatsci.2004.10.001.

[3] D.C. Lagoudas, Modeling of SMAs, 2008. https://doi.org/10.1007/978-0-387-47685-8.

[4] S.M. Takayuki Yoneyama, Shape memory alloys for biomedical applications, 2009. https://doi.org/10.1002/9781118577776.

[5] C. Lexcellent, Shape-Memory Alloys Handbook, Wiley, 2013. http://eu.wiley.com/WileyCDA/WileyTitle/productCd-1848214340.html.

[6] K. Otsuka, C.M. Wayman, Shape Memory Materials, Cambridge University Press, Cambridge, UK, 1999.

[7] S. Miyazaki, Y. Ohmi, K. Otsuka, Y. Suzuki, CHARACTERISTICS OF DEFORMATION AND TRANSFORMATION PSEUDOELASTICITY IN Ti-Ni ALLOYS., in: J. Phys. (Paris), Colloq., 1982. https://doi.org/10.1051/jphyscol:1982434.

[8] P. A, D. J, M. S, Optimisation of processing and properties of medical grade Nitinol wire, Minimally Invasive Therapy & Allied Technologies, Proc. Int'l Conf. Shape Mem. Superelastic Technol. SMST-2000 107-118. (2000).

[9] S. Miyazaki, My Experience with Ti–Ni-Based and Ti-Based Shape Memory Alloys, Shape Mem. Superelasticity. 3 (2017) 279–314. https://doi.org/10.1007/s40830-017-0122-3.

[10] J. Perkins, SHAPE MEMORY EFFECTS IN ALLOYS, Plenum Press (Metall Soc of AIME Proc), 1975. https://doi.org/10.1007/978-1-4684-2211-5.

[11] P. Sittner, D. Vokoun, G.N. Dayananda, R. Stalmans, Recovery stress generation in shape memory Ti 50 Ni 45 Cu 5 thin wires, Mater. Sci. Eng. A. 286 (2000) 298–311.

[12] P.G. Mccormick, Y. Liu, Thermodynamic analysis of the martensite transformation in NiTi -II, Acta Metall. Mater. 42 (1994) 2407–2413.

[13] O. K, Related content Origin of Memory Effect in Cu-Al-Ni Alloy, Jpn. J. Appl. Phys. 10 (1971) 571–579. https://doi.org/10.1143/JJAP.10.571.

[14] S. Miyazaki, S. Kimura, K. Otsuka, Y. Suzuki, The habit plane and transformation strains associated with the martensitic transformation in Ti-Ni single crystals, Scr. Metall. 18 (1984) 883–888. https://doi.org/10.1016/0036-9748(84)90254-0.

[15] L.C. Brinson, I. Schmidt, R. Lammering, Stress-induced transformation behavior of a polycrystalline NiTi shape memory alloy: Micro and macromechanical investigations via in situ optical microscopy,

J. Mech. Phys. Solids. 52 (2004) 1549–1571. https://doi.org/10.1016/j.jmps.2004.01.001.

[16] Y. Chen, O. Tyc, L. Kadeřávek, O. Molnárová, L. Heller, P. Šittner, Temperature and microstructure dependence of localized tensile deformation of superelastic NiTi wires, Mater. Des. 174 (2019). https://doi.org/10.1016/j.matdes.2019.107797.

[17] Y. Chen, P. Sittner, Acta Materialia Recoverability of large strains and deformation twinning in martensite during tensile deformation of NiTi shape memory alloy polycrystals rov a, 180 (2019) 243–259. https://doi.org/10.1016/j.actamat.2019.09.012.

[18] L. Heller, H. Seiner, P. Šittner, P. Sedlák, O. Tyc, L. Kadeřávek, On the plastic deformation accompanying cyclic martensitic transformation in thermomechanically loaded NiTi, Int. J. Plast. 111 (2018) 53–71. https://doi.org/10.1016/j.ijplas.2018.07.007.

[19] Z. Moumni, W. Zaki, H. Maitournam, Cyclic behavior and energy approach to the fatigue of shape memory alloys, Mech. Mater. Struct. 4 (2009).

[20] R. DesRoches, J. McCormick, M. Delemont, Cyclic Properties of Superelastic Shape Memory Alloy Wires and Bars, J. Struct. Eng. 130 (2004) 38–46. https://doi.org/10.1061/(asce)0733-9445(2004)130:1(38).

[21] M.A. Iadicola, J.A. Shaw, The effect of uniaxial cyclic deformation on the evolution of phase transformation fronts in pseudoelastic NiTi wire, J. Intell. Mater. Syst. Struct. 13 (2002) 143–155. https://doi.org/10.1177/104538902761402549.

[22] B. Strnadel, S. Ohashi, H. Ohtsuka, T. Ishihara, S. Miyazaki, Cyclic stress-strain characteristics of TiNi and TiNiCu shape memory alloys, Mater. Sci. Eng. A. 202 (1995) 148–156. https://doi.org/10.1016/0921-5093(95)09801-1.

[23] P.G. McCormick, Y. Liu, S. Miyazaki, Intrinsic thermal-mechanical behaviour associated with the stress-induced martensitic transformation in NiTi, Mater. Sci. Eng. A. 167 (1993) 51–56. https://doi.org/10.1016/0921-5093(93)90336-D.

[24] J. Van HUMBEECK, CYCLING EFFECTS, FATIGUE AND DEGRADATION OF SHAPE MEMORY ALLOYS, Le J. Phys. IV. 01 (1991) C4-189-C4-197. https://doi.org/10.1051/jp4:1991429.

[25] S. Miyazaki, T. Imai, Y. Igo, K. Otsuka, EFFECT OF CYCLIC DEFORMATION ON THE PSEUDOELASTICITY CHARACTERISTICS OF Ti-Ni ALLOYS., Metall. Trans. A, Phys. Metall. Mater. Sci. 17 A (1986) 115–120. https://doi.org/10.1007/BF02644447.

[26] X. Gu, Y. Zhang, Y. You, X. Ju, J. Zhu, Z. Moumni, W. Zhang, Evolution of transformation characteristics of shape memory alloys during cyclic loading: Transformation temperature hysteresis and residual martensite, Smart Mater. Struct. 29 (2020). https://doi.org/10.1088/1361-665X/ab9f10.

[27] G. Eggeler, E. Hornbogen, A. Yawny, A. Heckmann, M. Wagner, Structural and functional fatigue of NiTi shape memory alloys, Mater. Sci. Eng. A. 378 (2004) 24–33. https://doi.org/10.1016/j.msea.2003.10.327.

[28] S. Miyazaki, T. Imai, K. Otsuka, Y. Suzuki, Luders-like Deformation Observed in the Transformation Pseudoelasticity of a Ti-Ni Alloy, Scr. Metall. 15 (1981) 853–856. https://doi.org/10.1016/0036-9748(81)90265-9.

[29] P. Sedmák, J. Pilch, L. Heller, J. Kopeček, J. Wright, P. Sedlák, M. Frost, P. Šittner, Grain-resolved analysis of localized deformation in nickel-titanium wire under tensile load, Science (80-. ). 353 (2016) 559–562. https://doi.org/10.1126/science.aad6700.

[30] J.A. Shaw, S. Kyriakides, Thermomechanical aspects of NiTi, J. Mech. Phys. Solids. 43 (1995) 1243–1281. https://doi.org/10.1016/0022-5096(95)00024-D.

[31] M.A. Iadicola, J.A. Shaw, Rate and thermal sensitivities of unstable transformation behavior in a shape memory alloy, Int. J. Plast. 20 (2004) 577–605. https://doi.org/10.1016/S0749-6419(03)00040-8.

[32] S. Daly, G. Ravichandran, K. Bhattacharya, Stress-induced martensitic phase transformation in thin sheets of Nitinol, Acta Mater. 55 (2007) 3593–3600. https://doi.org/10.1016/j.actamat.2007.02.011.

[33] Z.Q. Li, Q.P. Sun, Superelastic NiTi memory alloy micro-tube under tension - Nucleation and propagation of martensite band, Key Eng. Mater. 177-180 II (2000) 461–466. https://doi.org/10.4028/www.scientific.net/kem.177-180.461.

[34] J.A. Shaw, S. Kyriakides, Initiation and propagation of localized deformation in elasto-plastic strips under uniaxial tension, Int. J. Plast. 13 (1997) 837–871. https://doi.org/10.1016/S0749-6419(97)00062-4.

[35] E.A. Pieczyska, S.P. Gadaj, W.K. Nowacki, H. Tobushi, Phase-Transformation Fronts Evolution for Stress- and Strain-Controlled Tension Tests in TiNi Shape Memory Alloy, Exp. Mech. 46 (2006) 531–542. https://doi.org/10.1007/s11340-006-8351-y.

[36] C.M. Jackson, H.. Wagner, R.J. Wasilewski, 55-NITINOL-THE ALLOY WITH A MEMORY: ITS PHYSICAL METALLURGY, PROPERTIES, AND APPLICATIONS, 1972.

[37] M. Follador, M. Cianchetti, A. Arienti, C. Laschi, A general method for the design and fabrication of shape memory alloy active spring actuators, Smart Mater. Struct. 21 (2012). https://doi.org/10.1088/0964-1726/21/11/115029.

[38] C.B. Churchill, Experimental techniques for characterizing the thermo-electro-mechanical shakedown response of SMA wires and tubes, ProQuest Diss. Theses. (2010) 305. http://search.proquest.com/docview/288250390?accountid=14511%5Cnhttp://sfx.ucl.ac.uk/sfx_local?url_ver=Z39.88-2004&rft_val_fmt=info:ofi/fmt:kev:mtx:dissertation&genre=dissertations+&+theses&sid=ProQ:ProQuest+Dissertations+&+Theses+Global&atitle=&title=Exp.

[39] J. Perkins, R.O. Sponholz, STRESS-INDUCED MARTENSITIC TRANSFORMATION CYCLING AND TWO-WAY SHAPE MEMORY TRAINING IN Cu-Zn-Al ALLOYS., Metall. Trans. A, Phys. Metall. Mater. Sci. 15 A (1984) 313–321. https://doi.org/10.1007/BF02645117.

[40] G. Lebon, D. Jou, J.C. Vazquez, Understand non-equilibrium thermodynamics, Springer, Berlin

Hedelberg, 2008.

[41] A. Nespoli, F. Passaretti, F. Stortiero, E. Villa, Temperature-modulated differential scanning calorimetry for the study of reversing and nonreversing heat flow of shape memory alloys, in: J. Therm. Anal. Calorim., Kluwer Academic Publishers, 2014: pp. 771–777. https://doi.org/10.1007/s10973-013-3600-7.

[42] D. Favier, Y. Liu, Restoration by rapid overheating of thermally stabilized martensite of NiTi shape memory alloys, J. Alloys Compd. 297 (2000) 114–121. https://doi.org/10.1016/S0925-8388(99)00576-9.

[43] D. Favier, H. Louche, P. Schlosser, L. Orgéas, P. Vacher, L. Debove, Homogeneous and heterogeneous deformation mechanisms in an austenitic polycrystalline Ti-50.8 at.% Ni thin tube under tension. Investigation via temperature and strain fields measurements, Acta Mater. 55 (2007) 5310–5322. https://doi.org/10.1016/j.actamat.2007.05.027.

[44] H.M.R. de Oliveira, H. Louche, E.N.D. Grassi, D. Favier, Specific forward/reverse latent heat and martensite fraction measurement during superelastic deformation of nanostructured NiTi wires, Mater. Sci. Eng. A. 774 (2020). https://doi.org/10.1016/j.msea.2020.138928.

[45] Y. He, H. Yin, R. Zhou, Q. Sun, Ambient effect on damping peak of NiTi shape memory alloy, Mater. Lett. 64 (2010) 1483–1486. https://doi.org/10.1016/j.matlet.2010.03.068.

[46] Y.J. He, Q.P. Sun, On non-monotonic rate dependence of stress hysteresis of superelastic shape memory alloy bars, Int. J. Solids Struct. 48 (2011) 1688–1695. https://doi.org/10.1016/j.ijsolstr.2011.02.017.

[47] H. Yin, Y. He, Q. Sun, Effect of deformation frequency on temperature and stress oscillations in cyclic phase transition of NiTi shape memory alloy, J. Mech. Phys. Solids. 67 (2014) 100–128. https://doi.org/10.1016/j.jmps.2014.01.013.

[48] M.A. Iadicola, J.A. Shaw, An Experimental Setup for Measuring Unstable Thermo-mechanical Behavior of Shape Memory Alloy Wire, J. Intell. Mater. Syst. Struct. (2002) 1–10. https://doi.org/10.1106/104538902025935.

[49] Y.J. He, Q.P. Sun, International Journal of Solids and Structures Rate-dependent domain spacing in a stretched NiTi strip, 47 (2010) 2775–2783. https://doi.org/10.1016/j.ijsolstr.2010.06.006.

[50] L. Heller, P. Šittner, J. Pilch, M. Landa, Factors controlling superelastic damping capacity of SMAs, J. Mater. Eng. Perform. 18 (2009) 603–611. https://doi.org/10.1007/s11665-009-9358-1.

[51] E. Pieczyska, S. Gadaj, W. Nowacki, H. Tobushi, A. Chrysochoos, G. Martin, Investigation of nucleation and propagation of phase transitions in TiNi SMA, QIRT. 1 (2004) 117–128. https://doi.org/10.3166/qirt.1.117-128.

[52] Y. Xiao, P. Zeng, L. Lei, Experimental observations on mechanical response of three-phase NiTi shape memory alloy under uniaxial tension, Mater. Res. Express. 3 (2016). https://doi.org/10.1088/2053-1591/3/10/105701.

[53] M. Tazarv, D. Ph, A.M. Asce, M.S. Saiidi, D. Ph, F. Asce, Low-Damage Precast Columns for Accelerated Bridge Construction in High Seismic Zones, (2015) 1–13. https://doi.org/10.1061/(ASCE)BE.1943-5592.0000806.Author.

[54] J. Tušek, K. Engelbrecht, D. Eriksen, S. Dall'Olio, J. Tušek, N. Pryds, A regenerative elastocaloric heat pump, Nat. Energy. 1 (2016). https://doi.org/10.1038/nenergy.2016.134.

[55] M. Zhou, Y.S. Li, C. Zhang, L.F. Li, Elastocaloric effect and mechanical behavior for NiTi shape memory alloys, Chinese Phys. B. 27 (2018). https://doi.org/10.1088/1674-1056/27/10/106501.

[56] I. Takeuchi, K. Sandeman, Solid-state cooling with caloric materials, Phys. Today. 68 (2015) 48–54. https://doi.org/10.1063/PT.3.3022.

[57] L. Zhang, J.X. Zhao, L.F. Yue, H.X. Zhou, C.L. Ren, Cycle performance evaluation of various R134a/hydrocarbon blend refrigerants applied in vapor-compression heat pumps, Adv. Mech. Eng. 11 (2019) 1–14. https://doi.org/10.1177/1687814018819561.

[58] J. Pilch, L. Heller, P. Sittner, Final thermomechanical treatment of thin NiTi filaments for textile applications by electric current, ESOMAT 2009 - 8th Eur. Symp. Martensitic Transform. 05024 (2009). https://doi.org/10.1051/esomat/200905024.

[59] R. Delville, B. Malard, J. Pilch, P. Sittner, D. Schryvers, Transmission electron microscopy investigation of dislocation slip during superelastic cycling of Ni-Ti wires, Int. J. Plast. 27 (2011) 282–297. https://doi.org/10.1016/j.ijplas.2010.05.005.

[60] R. Delville, B. Malard, J. Pilch, P. Sittner, D. Schryvers, Microstructure changes during non-conventional heat treatment of thin Ni-Ti wires by pulsed electric current studied by transmission electron microscopy, Acta Mater. 58 (2010) 4503–4515. https://doi.org/10.1016/j.actamat.2010.04.046.

[61] S. R., E., B. R., J., Modern Physical Metallurgy & Materials Engineering, Sixth, Elsevier Science, 1999.

[62] E. Pieczyska, H. Tobushi, TiNi shape memory alloy tension at various temperatures - infrared imaging of shape memory effect and pseudoelasticity, Mech. Control. 30 (2011) 20–26.

[63] A. Maynadier, M. Poncelet, K. Lavernhe-Taillard, S. Roux, One-shot Measurement of Thermal and Kinematic Fields: InfraRed Image Correlation (IRIC), Exp. Mech. 52 (2012) 241–255. https://doi.org/10.1007/s11340-011-9483-2.

[64] Lord Kelvin, On the thermoelastic and thermo-magnetic properties of matter, Trans. Roy. Soc. Edimb. 20 (1853) 57–77.

[65] M.A. Biot, Thermoelasticity and Irreversible Thermodynamics, 240 (1962). https://doi.org/10.1063/1.1722351.

[66] W. Thomson, On a Universal Tendency in Nature to the Dissipation of Mechanical Energy., Proc. R. Soc. Edinburgh. 3 (1857) 139–142. https://doi.org/10.1017/s0370164600027541.

[67] S. C., L. D., L. L., DIFFERENTIAL SCANNING CALORIMETRY AND DIFFERENTIAL THERMAL ANALYSIS, in: Charact. Od Mater., N., Kauffm, John Wiley & Sons, 2012: pp. 483–493.

[68] V. Delobelle, D. Favier, H. Louche, N. Connesson, Determination of Local Thermophysical Properties and Heat of Transition from Thermal Fields Measurement During Drop Calorimetric Experiment, Exp. Mech. 55 (2015) 711–723. https://doi.org/10.1007/s11340-014-9877-z.

[69] A. Chrysochoos, Dissipation et blocage d'énergie lors d'un écrouissage en traction simple, Université des Sciences et Techniques du Languedoc, 1987.

[70] D. Ronnpagel, A new method of deformation calorimetry, J. Phys. E Sci. Instrum. 12 (1979).

[71] M. Vollmer, K.-P. Mollmann, Infrared Thermal Imaging, Fundamentals, Research and Applications, 2nd ed., Weiheim, 2018.

[72] J.E. Bailey, P.B. Hirsch, The dislocation distribution, flow stress, and stored energy in cold-worked polycrystalline silver, Philos. Mag. 5 (1960) 485–497. https://doi.org/10.1080/14786436008238300.

[73] W.S.. Farren, G.I. Taylor, The heat developed during plastic extension of metals, Proc. R. Soc. London. Ser. A, Contain. Pap. a Math. Phys. Character. 107 (1925) 422–451. https://doi.org/10.1098/rspa.1925.0034.

[74] W.N. Sharpe, Springer handook of experimental solid mechanics, 2008.

[75] M. B. BEVER, the Stored Energy of Cold Work, 1973.

[76] G.I. Taylor, H.. Quinney, The Latent Energy Remaining in a Metal after Cold Working, Proc. R. Soc. London. Ser. A, Contain. Pap. a Math. Phys. Character. 143 (1934) 307–326. http://rspa.royalsocietypublishing.org/.

[77] R.O. Williams, The increase in internal energy of copper crystals during deforming at 25°C, Acta Metall. 12 (1964) 745–747. https://doi.org/10.1016/0001-6160(64)90225-1.

[78] N. Gao, Applications of differential scanning calorimetry on materials subjected by severe plastic deformation, in: Mater. Sci. Forum, Trans Tech Publications Ltd, 2008: pp. 255–260. https://doi.org/10.4028/www.scientific.net/msf.584-586.255.

[79] A. Chrysochoos, CONTRIBUTION A L'ETUDE DE LA DISSIPATION INTTRINSEQUE POUR DES MATERIAUX ELASTIPLASTIQUES EN GRANDES DEFORMATIONS, 1983.

[80] A.S. Machin, J.G. Sparrow, M.G. Stimson, S. Division, Mean stress dependence of the thermoelastic constant, (1987) 6–9.

[81] A. Chrysochoos, J. Dulieu-Barton, Infra-red techniques for thermomechanical characterisation of materials and structures, Exp. Mech. 55 (2015) 651–652. https://doi.org/10.1007/s11340-015-0002-8.

[82] C. Saix, P. Jouanna, Dissipation plastique et thermographie de surface. Premiers résultats

expérimentaux, Matériaux Constr. 12 (1979) 457–466. https://doi.org/10.1007/BF02476290.

[83] W. Oliferuk, S. P. Gadaj, M.W. Grabski, Energy storage during the tensile deformation of Armco iron and austenitic steel, Mater. Sci. Eng. 70 (1985) 131–141. https://doi.org/10.1016/0025-5416(85)90274-5.

[84] J. Ye, Utilisation de mesures de champs thermique et cinématique pour la reconstruction de sources de chaleur thermomécaniques par inversion de l'equation d'advection-diffusion 1D, Université de Lorraine, 2015.

[85] C. Doudard, S. Calloch, F. Hild, S. Roux, C. Doudard, S. Calloch, F. Hild, S. Roux, Identification of heat source fields from infra-red thermography : Determination of ' self-heating ' in a dual-phase steel by using a dog bone sample To cite this version : HAL Id : hal-00430489 Identification of heat source fields from infra-red thermogr, (2010).

[86] N. Renault, S. André, D. Maillet, C. Cunat, A spectral method for the estimation of a thermomechanical heat source from infrared temperature measurements, Int. J. Therm. Sci. 49 (2010) 1394–1406. https://doi.org/10.1016/j.ijthermalsci.2010.03.001.

[87] A. Chrysochoos, J.-C. Chezeaux, H. Caumon, Analyse thermomécanique des lois de comportement par thermographie infrarouge, Rev. Phys. Appliquée. 24 (1989) 215–225. https://doi.org/10.1051/rphysap:01989002402021500.

[88] A. Chrysochoos, O. Maisonneuve, G. Martin, H. Caumon, J.C. Chezeaux, Plastic and dissipated work and stored energy, Nucl. Eng. Des. 114 (1989) 323–333. https://doi.org/10.1016/0029-s5493(89)90110-6.

[89] Q.S. Nguyen, Sur les Matériaux Standard Généralisés Sur les matériaux standards généralisés, (2014).

[90] H. Louche, Analyse par thermographie infrarouge des effets dissipatifs de la localisation dans des aciers, 1999.

[91] A. Chrysochoos, H. Louche, An infrared image processing to analyse the calorific effects accompanying strain localisation, Int. J. Eng. Sci. 38 (2000) 1759–1788. https://doi.org/https://10.1016/S0020-7225(00)00002-1.

[92] a Chrysochoos, R. Peyroux, Experimental analysis and numerical simulation of thermomechanical couplings in solid materials., Rev. Gen. Therm. 37 (1998) 582–606. https://doi.org/10.1016/S0035-3159(98)80036-6.

[93] M. Vollmer, K.P. Mollmann, Infrared Thermal Imaging, Second, Wiley-VCH Verlag GmbH & Co. KGaA, 2018.

[94] A. Chrysochoos, G. Martin, Tensile test microcalorimetry for thermomechanical behaviour law analysis, Mater. Sci. Eng. A. 108 (1989) 25–32. https://doi.org/10.1016/0921-5093(89)90402-4.

[95] K. Mukherjee, S. Sircar, N.B. Dahotre, Thermal effects associated with stress-induced martensitic transformation, Mater. Sci. Eng. 74 (1985) 75–84.

[96] J. Van Humbeeck, L. Delaey, J. Van Humbeeck, L.D. The, I. Of, THE INFLUENCE OF STRAIN-RATE , AMPLITUDE AND TEMPERATURE ON THE HYSTERESIS OF A PSEUDOELASTIC Cu-Zn-Al SINGLE CRYSTAL To cite this version : HAL Id : jpa-00221028, (1981).

[97] P.H. Leo, T.W. Shield, O.P. Bruno, Transient heat transfer effects on the pseudoelastic behavior of shape-memory wires, Acta Metall. Mater. 41 (1993) 2477–2485. https://doi.org/10.1016/0956-7151(93)90328-P.

[98] Q. Kan, C. Yu, G. Kang, J. Li, W. Yan, Experimental observations on rate-dependent cyclic deformation of super-elastic NiTi shape memory alloy, Mech. Mater. 97 (2016) 48–58. https://doi.org/10.1016/j.mechmat.2016.02.011.

[99] A. Chrysochoos, Y. Surrel, Basics of Metrology and Introduction to Techniques, Full-f. Meas. Identif. Solid Mech. (2012) 1–30. https://doi.org/10.1002/9781118578469.ch1.

[100] P. Schlosser, H. Louche, D. Favier, L. Orgéas, Image processing to estimate the heat sources related to phase transformations during tensile tests of NiTi tubes, in: Strain, 2007: pp. 260–271. https://doi.org/10.1111/j.1475-1305.2007.00350.x.

[101] G. Tessier, M. Bardoux, C. Boú, C. Filloy, D. Fournier, Back side thermal imaging of integrated circuits at high spatial resolution, Appl. Phys. Lett. 90 (2007). https://doi.org/10.1063/1.2732179.

[102] A. Chrysochoos, H. Pham, O. Maisonneuve, Energy balance of thermoelastic martensite transformation under stress, Nucl. Eng. Des. 162 (1996) 1–12. https://doi.org/10.1016/0029-5493(95)01140-4.

[103] O.P. Bruno, N. Carolina, Ical review, 74 (1995) 746–749.

[104] A. Ahadi, Q. Sun, Effects of grain size on the rate-dependent thermomechanical responses of nanostructured superelastic NiTi, Acta Mater. 76 (2014) 186–197. https://doi.org/10.1016/j.actamat.2014.05.007.

[105] A. Chrysochoos, O.M. A. Chrysochoos, M. Lobel, Couplages thermomécaniques du comportement pseudoélastique d’alliages Cu-Zn-Al et Ni-Ti, C. R. Acad. Sci. IIb. 320 (1995) 217–223.

[106] H. Louche, P. Schlosser, D. Favier, L. Orgéas, Heat Source Processing for Localized Deformation with Non-Constant Thermal Conductivity. Application to Superelastic Tensile Tests of NiTi Shape Memory Alloys, Exp. Mech. 52 (2012) 1313–1328. https://doi.org/10.1007/s11340-012-9607-3.

[107] P. Schlosser, Influence of thermal and mechanical aspects on deformation behaviour of NiTi alloys, 2009.

[108] Y. Xiao, P. Zeng, L. Lei, Y. Zhang, In situ observation on temperature dependence of martensitic transformation and plastic deformation in superelastic NiTi shape memory alloy, Mater. Des. 134 (2017) 111–120. https://doi.org/10.1016/j.matdes.2017.08.037.

[109] V. Delobelle, D. Favier, H. Louche, Heat Estimation from Infrared Measurement Compared to DSC for Austenite to R Phase Transformation in a NiTi Alloy, J. Microbiol. Methods. 22 (2013) 1688–1693. https://doi.org/https://10.1007/s11665-012-0466-y.

[110] V. Delobelle, Contributions à l'étude thermomécanique des alliages à mémoire de forme NiTi et à la réalisation par soudage de matériaux architecturés NiTi, 2012. https://tel.archives-ouvertes.fr/tel-00982218.

[111] H. Louche, A. Chrysochoos, Thermal and dissipative effects of accompanying Lüders band propagation, Mater. Sci. Eng. A. 307 (2001) 15–22. https://doi.org/https://10.1016/S0921-5093(00)01975-4.

[112] A. Chrysochoos, H. Louche, Infrared image processing to analyze the calorific effects accompanying strain localization, Int. J. Eng. Sci. 38 (2000) 1759–1788. https://doi.org/10.1016/S0020-7225(00)00002-1.

[113] A. Chrysochoos, R. Peyroux, Experimental analysis and numerical simulation of thermomechanical couplings in solid materials, Rev. Gen. Therm. 37 (1998) 582–606. https://doi.org/10.1016/s0035-3159(98)80036-6.

[114] P. Schlosser, Influence of thermal and mechanical aspects on deformation behaviour of NiTi alloys, Université Joseph-Fourier, 2008. https://tel.archives-ouvertes.fr/tel-00384405v2.

[115] A. Chrysochoos, V. Huon, F. Jourdan, J.-M.M. Muracciole, R. Peyroux, B. Wattrisse, Use of Full-Field DIC & IRT Measurements for the Thermomechanical Analysis of Material Behavior, Strain. 46 (2010) 117–130.

[116] A. CHRYSOCHOOS, F. BELMAHJOUB, Thermographic analysis of thermomechanical couplings, Arch. Mech. 44 (1992) 55–68.

[117] X. Balandraud, A. Chrysochoos, S. Leclercq, R. Peyroux, Effet du couplage thermomécanique sur la propagation d'un front de changement de phase, Comptes Rendus l'Academie Sci. - Ser. IIb Mec. 329 (2001) 621–626. https://doi.org/10.1016/S1620-7742(01)01376-9.

[118] L. Ianniciello, M. Romanini, L. Mañosa, A. Planes, K. Engelbrecht, E. Vives, Tracking the dynamics of power sources and sinks during the martensitic transformation of a Cu-Al-Ni single crystal, Appl. Phys. Lett. 116 (2020). https://doi.org/10.1063/5.0006859.

[119] E. Alarcon, L. Heller, Deformation infrared calorimetry for materials characterization applied to study cyclic superelasticity in NiTi wires, Mater. Des. 199 (2021) 1–23. https://doi.org/10.1016/j.matdes.2020.109406.

[120] H. Louche, Analyse par thermographie infrarouge des effets dissipatifs de la localisation dans des aciers, Université Montpellier II, 1999. https://tel.archives-ouvertes.fr/tel-00259398.

[121] H. Louche, A. Chrysochoos, Thermal and dissipative effects of accompanying Lüders band propagation, Mater. Sci. Eng. A. 307 (2001) 15–22. https://doi.org/10.1016/S0921-5093(00)01975-4.

[122] S. Dumoulin, H. Louche, O.S. Hopperstad, T. Børvik, Heat sources, energy storage and dissipation in high-strength steels: Experiments and modelling, Eur. J. Mech. A / Solids. 29 (2010) 461–474. https://doi.org/10.1016/j.euromechsol.2009.11.005.

[123] A. Chrysochoos, V. Huon, F. Jourdan, J.M. Muracciole, R. Peyroux, B. Wattrisse, Use of full-field digital image correlation and infrared thermography measurements for the thermomechanical analysis of material behaviour, Strain. 46 (2010) 117–130. https://doi.org/10.1111/j.1475-1305.2009.00635.x.

[124] X.G. Wang, L. Wang, M.X. Huang, Kinematic and thermal characteristics of Lüders and Portevin-Le Châtelier bands in a medium Mn transformation-induced plasticity steel, Acta Mater. 124 (2017) 17–29. https://doi.org/10.1016/j.actamat.2016.10.069.

[125] D. Pajani, Thermographie - Principes et mesure, Tech. l'ingénieur. 33 (2013) 1–21.

[126] P. Jongchansitto, C. Douellou, I. Preechawuttipong, X. Balandraud, Comparison between 0D and 1D approaches for mechanical dissipation measurement during fatigue tests, Strain. 55 (2019) 1–16. https://doi.org/10.1111/str.12307.

[127] D. Delpueyo, X. Balandraud, M. Grédiac, S. Stanciu, N. Cimpoesu, A specific device for enhanced measurement of mechanical dissipation in specimens subjected to long-term tensile tests in fatigue, Strain. 54 (2018) 1–14. https://doi.org/10.1111/str.12252.

[128] M.L. Pastor, X. Balandraud, M. Grédiac, J.L. Robert, Applying infrared thermography to study the heating of 2024-T3 aluminium specimens under fatigue loading, Infrared Phys. Technol. 51 (2008) 505–515. https://doi.org/10.1016/j.infrared.2008.01.001.

[129] N. Ranc, A. Blanche, D. Ryckelynck, A. Chrysochoos, POD Preprocessing of IR Thermal Data to Assess Heat Source Distributions, Exp. Mech. 55 (2015) 725–739. https://doi.org/10.1007/s11340-014-9858-2.

[130] T. Pottier, H. Louche, S. Samper, H. Favrelière, F. Toussaint, P. Vacher, Proposition of a modal filtering method to enhance heat source computation within heterogeneous thermomechanical problems, Int. J. Eng. Sci. 81 (2014) 163–176. https://doi.org/10.1016/j.ijengsci.2014.04.010.

[131] D. Delpueyo, X. Balandraud, M. Grédiac, Heat source reconstruction from noisy temperature fields using an optimised derivative Gaussian filter, Infrared Phys. Technol. 60 (2013) 312–322. https://doi.org/10.1016/j.infrared.2013.06.004.

[132] G. Corvec, E. Robin, J.-B. Le Cam, J.-C. Sangleboeuf, P. Lucas, Improving spatio-temporal resolution of infrared images to detect thermal activity of defect at the surface of inorganic glass, Infrared Phys. Technol. 77 (2016) 193–202. https://doi.org/10.1016/J.INFRARED.2016.05.026.

[133] C. Beitone, X. Balandraud, D. Delpueyo, M. Grédiac, Heat source reconstruction from noisy temperature fields using a gradient anisotropic diffusion filter, Infrared Phys. Technol. 80 (2017) 27–37. https://doi.org/10.1016/j.infrared.2016.11.003.

[134] E.A. Pieczyska, S.P. Gadaj, W.K. Nowacki, H. Tobushi, Thermomechanical investigations of martensitic and reverse transformations in TiNi shape memory alloy, Bull. Polish Acad. Sci. Tech. Sci. 52 (2004) 165–171.

[135] E. Pieczyska, Activity of stress-induced martensite transformation in TiNi shape memory alloy studied by infrared technique, J. Mod. Opt. 57 (2010) 1700–1707.

https://doi.org/10.1080/09500341003725748.

[136] E.A. Pieczyska, H. Tobushi, K. Kulasinski, Development of transformation bands in TiNi SMA for various stress and strain rates studied by a fast and sensitive infrared camera, Smart Mater. Struct. 22 (2013). https://doi.org/10.1088/0964-1726/22/3/035007.

[137] V. Dunić, E.A. Pieczyska, H. Tobushi, M. Staszczak, R. Slavković, Experimental and numerical thermo-mechanical analysis of shape memory alloy subjected to tension with various stress and strain rates, Smart Mater. Struct. 23 (2014). https://doi.org/10.1088/0964-1726/23/5/055026.

[138] E. Alarcon, L. Heller, S.A. Chirani, P. Sittner, L. Saint-Sulpice, S. Calloch, Phase transformations and fatigue of NiTi, MATEC Web Conf. 33 (2015) 1–6. https://doi.org/10.1051/matecconf/20153303011.

[139] V. Dunić, E.A. Pieczyska, Z.L. Kowalewski, R. Matsui, R. Slavković, Experimental and numerical investigation of mechanical and thermal effects in TiNi SMA during transformation-induced creep phenomena, Materials (Basel). 16 (2019). https://doi.org/10.3390/ma12060883.

[140] A. Chrysochoos, M. Lôbel, O. Maisonneuve, Couplages thermomécaniques du comportement pseudoélastique d’alliages Cu-Zn-Al et Ni-Ti, C. R. Acad. Sci. Patis. 320 (1995) 217–223.

[141] J.A. Shaw, S. Kyriakides, On the nucleation and propagation of phase transformation fronts in a NiTi alloy, Acta Mater. 45 (1997) 683–700. https://doi.org/10.1016/S1359-6454(96)00189-9.

[142] Y.J. He, Q.P. Sun, Rate-dependent domain spacing in a stretched NiTi strip, Int. J. Solids Struct. 47 (2010) 2775–2783. https://doi.org/10.1016/j.ijsolstr.2010.06.006.

[143] L. Zheng, Y. He, Z. Moumni, Effects of Lüders-like bands on NiTi fatigue behaviors, Int. J. Solids Struct. 83 (2016) 28–44. https://doi.org/10.1016/j.ijsolstr.2015.12.021.

[144] L. Heller, P. Šittner, P. Sedlák, H. Seiner, O. Tyc, L. Kadeřávek, P. Sedmák, M. Vronka, Beyond the strain recoverability of martensitic transformation in NiTi, Int. J. Plast. 116 (2019) 232–264. https://doi.org/10.1016/j.ijplas.2019.01.007.

[145] S.C. Dutta, R. Majumder, Shape memory alloy (SMA) as a potential damper in structural vibration control, Springer International Publishing, 2019. https://doi.org/10.1007/978-3-319-99353-9_51.

[146] X. Balandraud, A. Chrysochoos, S. Leclercq, R. Peyroux, Effet du couplage thermomécanique sur la propagation d’un front de changement de phase, C. R. Acad. Sci. IIb. 38 (2001) 621–626. https://doi.org/10.1016/S0020-7225(00)00002-1.

[147] B. Wattrisse, J.M. Muracciole, A. Chrysochoos, Thermomechanical effects of accompanying the localized necking of semi-crystalline polymers, Int. J. Therm. Sci. 41 (2002) 422–427. https://doi.org/10.1016/S1290-0729(02)01334-0.

[148] N. Connesson, F. Maquin, F. Pierron, Experimental Energy Balance During the First Cycles of Cyclically Loaded Specimens Under the Conventional Yield Stress, Exp. Mech. 51 (2011) 23–44. https://doi.org/10.1007/s11340-010-9336-4.

[149] A. Blanche, A. Chrysochoos, N. Ranc, V. Favier, Dissipation Assessments During Dynamic Very High Cycle Fatigue Tests, Exp. Mech. 55 (2015) 699–709. https://doi.org/10.1007/s11340-014-9857-3.

[150] A.P. Witkin, Scale-Space Filtering, Morgan Kaufmann Publishers, Inc., 1983. https://doi.org/10.1016/b978-0-08-051581-6.50036-2.

[151] D. Delpueyo, X. Balandraud, M. Grédiac, Heat source reconstruction from noisy temperature fields using an optimised derivative Gaussian filter, Infrared Phys. Technol. 60 (2013) 312–322. https://doi.org/10.1016/j.infrared.2013.06.004.

[152] A. Chrysochoos, Y. Surrel, Basics of Metrology and Introduction to Techniques, in: M. Grédiac, F. Hild (Eds.), Full-f. Meas. Identif. Solid Mech., Wiley-ISTE, 2012: pp. 1–30. https://doi.org/10.1002/9781118578469.ch1.

[153] I. Philippi, J.C. Batsale, D. Maillet, A. Degiovanni, Measurement of thermal diffusivities through processing of infrared images, Rev. Sci. Instrum. 66 (1995) 182–192. https://doi.org/10.1063/1.1146432.

[154] M. Rohde, A. Schüssler, On the response-time behaviour of laser micromachined NiTi shape memory actuators, Sensors Actuators, A Phys. 61 (1997) 463–468. https://doi.org/10.1016/S0924-4247(97)80306-8.

[155] M.G. Faulkner, J.J. Amalraj, A. Bhattacharyya, Experimental determination of thermal and electrical properties of Ni-Ti shape memory wires, Smart Mater. Struct. 9 (2000) 632–639. https://doi.org/10.1088/0964-1726/9/5/307.

[156] C. Zanotti, P. Giuliani, G. Riva, A. Tuissi, A. Chrysanthou, Thermal diffusivity of Ni-Ti SMAs, J. Alloys Compd. 473 (2009) 231–237. https://doi.org/10.1016/j.jallcom.2008.05.040.

[157] C. Zanotti, P. Giuliani, A. Chrysanthou, Martensitic-Austenitic phase transformation of Ni-Ti SMAs: Thermal properties, Intermetallics. 24 (2012) 106–114. https://doi.org/10.1016/j.intermet.2012.01.026.

[158] G.H. Meyer, The Method od Lines (MOL) for the Diffusion Equation, in: Time-Discrete Method Lines Options Bond. (A PDE Approach), 2015: pp. 57–74. https://doi.org/10.1142/9789814619684_0002.

[159] P. Šittner, M. Landa, P. Lukáš, V. Novák, R-phase transformation phenomena in thermomechanically loaded NiTi polycrystals, Mech. Mater. 38 (2006) 475–492. https://doi.org/10.1016/j.mechmat.2005.05.025.

[160] A. Jury, X. Balandraud, L. Heller, E. Alarcon, M. Karlik, One-Dimensional Heat Source Reconstruction Applied to Phase Transforming Superelastic Ni-Ti Wire, Conf. Proc. Soc. Exp. Mech. Ser. 6 (2020) 33–40. https://doi.org/10.1007/978-3-030-30098-2_6.

[161] K. Takeda, H. Tobushi, E.A. Pieczyska, Transformation-Induced Creep and Creep Recovery of Shape Memory Alloy, Materials (Basel). 5 (2012) 909–921. https://doi.org/10.3390/ma5050909.

[162] J.A. Shaw, C.B. Churchill, M.A. Iadicola, Tips and tricks for characterizing shape memory alloy wire: Part 1-differential scanning calorimetry and basic phenomena, Exp. Tech. 32 (2008) 55–62. https://doi.org/10.1111/j.1747-1567.2008.00410.x.

[163] D.A. Hebda, S.R. White, Effect of training conditions and extended thermal cycling on nitinol two-way shape memory behavior, Smart Mater. Struct. 4 (1995) 298–304. https://doi.org/10.1088/0964-1726/4/4/010.

[164] G. Kang, Q. Kan, C. Yu, D. Song, Y. Liu, Whole-life transformation ratchetting and fatigue of super-elastic NiTi Alloy under uniaxial stress-controlled cyclic loading, Mater. Sci. Eng. A. 535 (2012) 228–234. https://doi.org/10.1016/j.msea.2011.12.071.

[165] Y. Chen, O. Tyc, O. Molnárová, L. Heller, P. Sittner, Tensile Deformation of Superelastic NiTi Wires in Wide Temperature and Microstructure Ranges, Shape Mem. Superelasticity. 5 (2019) 42–62. https://doi.org/10.1007/s40830-018-00205-2.

[166] P.G. McCormick, Y. Liu, S. Miyazaki, Intrinsic thermal-mechanical behaviour associated with the stress-induced martensitic transformation in NiTi, Mater. Sci. Eng. A. 167 (1993) 51–56. https://doi.org/10.1016/0921-5093(93)90336-D.

[167] E. Pieczyska, S. Gadaj, W.K. Nowacki, K. Hoshio, Y. Makino, H. Tobushi, Characteristics of energy storage and dissipation in TiNi shape memory alloy, Sci. Technol. Adv. Mater. 6 (2005) 889–894. https://doi.org/10.1016/j.stam.2005.07.008.

[168] Y. Xiao, P. Zeng, L. Lei, Grain size effect on mechanical performance of nanostructured superelastic NiTi alloy, Mater. Res. Express. 4 (2017). https://doi.org/10.1088/2053-1591/aa6074.

[169] P. Sedmák, P. Šittner, J. Pilch, C. Curfs, Instability of cyclic superelastic deformation of NiTi investigated by synchrotron X-ray diffraction, Acta Mater. 94 (2015) 257–270. https://doi.org/10.1016/j.actamat.2015.04.039.

[170] A. Jury, X. Balandraud, L. Heller, P. Šittner, M. Karlik, Reconstruction of Heat Sources Induced in Superelastically Loaded Ni-Ti Wire By Localized Deformation Processes, Exp. Mech. (2020). https://doi.org/10.1007/s11340-020-00648-8.

[171] D.J. Sharar, B.F. Donovan, R.J. Warzoha, A.A. Wilson, A.C. Leff, B.M. Hanrahan, Solid-state thermal energy storage using reversible martensitic transformations, Appl. Phys. Lett. 114 (2019). https://doi.org/10.1063/1.5087135.

[172] M. Li, M. Chen, Q. Sun, Nonlocal modeling and analysis of spatiotemporal patterns in non-isothermal phase transformation of NiTi strips, Int. J. Solids Struct. (2020). https://doi.org/10.1016/j.ijsolstr.2020.05.013.